MODELING THE DISTRIBUTION OF DARK MATTER AND ITS CONNECTION TO GALAXIES

A DISSERTATION
SUBMITTED TO THE DEPARTMENT OF PHYSICS
AND THE COMMITTEE ON GRADUATE STUDIES
OF STANFORD UNIVERSITY
IN PARTIAL FULFILLMENT OF THE REQUIREMENTS
FOR THE DEGREE OF
DOCTOR OF PHILOSOPHY

Yao-Yuan Mao
May 2016

I certify that I have read this dissertation and that, in my opinion, it is fully adequate in scope and quality as a dissertation for the degree of Doctor of Philosophy.

Risa Wechsler, Primary Adviser

I certify that I have read this dissertation and that, in my opinion, it is fully adequate in scope and quality as a dissertation for the degree of Doctor of Philosophy.

Tom Abel

I certify that I have read this dissertation and that, in my opinion, it is fully adequate in scope and quality as a dissertation for the degree of Doctor of Philosophy.

Steven Allen

Approved for the Stanford University Committee on Graduate Studies.

Patricia J. Gumport, Vice Provost for Graduate Education

Abstract

Despite the mysterious nature of dark matter and dark energy, the Lambda–Cold Dark Matter (ΛCDM) model provides a reasonably accurate description of the evolution of the cosmos and the distribution of galaxies. Today, we are set to tackle more specific and quantitative questions about the galaxy formation physics, the nature of dark matter, and the connection between the dark and the visible components. The answers to these questions are however elusive, because dark matter is not directly observable, and various unknowns lie between what we can observe and what we can calculate. Hence, mathematical models that bridge the observable and the calculable are essential for the study of modern cosmology.

The aim of my thesis work is to improve existing models and also to construct new models for various aspects of the dark matter distribution, as dark matter structures the cosmic web and forms the nests of visible galaxies. Utilizing a series of cosmological dark matter simulations which span a wide dynamical range and a statistical sample of zoom-in simulations which focus on individual dark matter halos, we develop models for the spatial and velocity distribution of dark matter particles, the abundance of dark substructures, and the empirical connection between dark matter and galaxies.

As more precise observational results become available, more accurate models are then required to test the consistency between these results and the ΛCDM predictions. For all the models we investigate, we find that the formation history of dark matter halos always plays a crucial role. Neglecting the halo formation history would result in systematic biases when we interpret various observational results, including dark matter direct detection experiments, the detection of dark substructures with strong-lensed systems, the large-scale spatial clustering of galaxies, and the abundance of dwarf galaxies. Rectifying this, our work will enable us to fully utilize the complementary power of diverse observational datasets to test the ΛCDM model and to seek new physics.

Acknowledgements

First and foremost, I would like to thank my advisor, Risa Wechsler. Risa has been an amazing mentor, and really a role model for me. I have learned enormously from her, not only about astrophysics and cosmology, but also about being an independent researcher. I joined Stanford with very little background in cosmology, but Risa has made sure that I kept my steps steady. She is always friendly and approachable, and her knowledge and passion are always inspiring. I enjoyed almost every discussion with her (and for the very few ones I didn't enjoy, I am certain that the topic was to blame). Besides being my advisor, Risa is also a very good friend. She has given me strength when I needed it, and shown me how to concurrently do good science and be human. Thank you, Risa; I am fortunate to have you as my advisor.

Risa also leads a wonderful research group. This group is energetic and full of interesting ideas. I am really grateful to every member in Risa's group, former and current alike. When I first joined Risa's group, Peter Behroozi, Louis Strigari, and Hao-Yi Wu have patiently coached me, providing me the fundamentals I needed in my very first projects. They have also been very helpful along my PhD journey. My collaborations with Matthew Becker, Alis Deason, Oliver Hahn, Yashar Hezaveh, Yu Lu, Phil Marshall, and Sam Skillman have all been fun and fruitful, and I have been hugely benefited from the enlightening discussions with them. It has been my pleasure to work with Benjamin Lehmann and Marc Williamson, who both have contributed to the work presented here. I thank Tony Li for being my office buddy and for sharing all those "wait-tomorrrow-is-Friday-already?" moments with me. I am also thankful to Michael Busha, Joe DeRose, Harry Desmond, Simon Foreman, Elisabeth Krause, Warren Morningstar, Rachel Reddick, Eduardo Rozo, Eli Rykoff, Vincent Su, and Hung-I Yang for all the productive exchanges we had.

Working at the Kavli Institute for Particle Astrophysics and Cosmology (KIPAC) has certainly made my PhD life more vibrant, and people at KIPAC are like family. I thank Tom Abel and Roger Blandford for their leadership of KIPAC, which has made KIPAC a lively place. I thank Ralf Kaehler, who has helped me many times when it comes to visualizing simulations, and thank Stuart Marshall, who has always been helpful and tolerant when we messed something up in the computing systems. I also thank Steven Allen, Keith Bechtol, Patricia Burchat, Blas Cabrera, Chihway Chang, Helen Craig, Alex Drlica-Wagner, Jimmy Grayson, Chao-Lin Kuo, Devon Powell, Kristi Schneck, Leonardo Senatore, Paul Simeon, and Anja von der Linden for all the scientific discussions we had (and for the non-scientific ones too). I deeply thank Christine Aguilar, Ziba Mahdavi, Martha Siegel, David Stricker, and also the SLAC computational team for their consistent administrative support.

During my PhD study, many people have given me constructive comments, suggestions, and even guidance. In particular, I want to thank Michael Boylan-Kolchin, James Bullock, Neal Dadal, Benedikt Diemer, Marla Geha, Andrew Hearin, Anatoly Klypin, Alexander Knebe, Rafael Lang, Joel Primack, Peter Sorensen, Jeremy Tinker, Erik Tollerud, Matt Turk, Frank van den Bosch, Mike Warren, and Andrew Zentner. They all have been very helpful and generous when I seek for their input.

I thank Ric Weiland and Mike Schaefer for their generosity, as my PhD study was partly supported by the Weiland Family Stanford Graduate Fellowship. I thank Maria Frank for her administrative support along my PhD journey, literally from admission to graduation. I thank Tom Abel, Steven Allen, and Patricia Burchat for being on my dissertation defense committee, and thank Bradley Efron for chairing this committee.

I am very thankful to my family, especially my parents, for allowing me to leave Taiwan and pursue this career path. I am also grateful to my supportive connections, both local and remote ones. I apologize for not listing all the names of these connections; the list is rather long. I thank my friends in the Bay Area who have extended their hospitality to me, friends at Stanford who make sure that I am not alone, friends in other institutes who know exactly what a PhD life is like, and friends around the world who care for me regardless which time zones they are in.

Last but not least, I am truly fortunate to have the company of Li-Cheng Tsai during my time at Stanford. Not only does he give me the emotional support that I need, but he also teaches me probability theory (which turns out to be crucially useful). And being close to a mathematician certainly makes me more rigorous when it comes to math. Li-Cheng has undoubtedly made my PhD journey more enjoyable and colorful. I cherish his company.

Contents

List of Tables

List of Figures

Chapter 1

Introduction

1.1 Lambda–Cold Dark Matter Cosmology

It was only a hundred years ago when we realized the universe is much larger than the Milky Way, our home galaxy. Yet over the last few decades, rapid progress in both astronomical observations and theoretical development has established a general picture of how the cosmos form and evolve. This general picture, also known as the "standard model of cosmology", is the Lambda–Cold Dark Matter (ΛCDM) model. The ΛCDM model specifies that the universe consists of three components: (1) the ordinary matter (or "baryons" as how cosmologists call it[1]), which is everything in the standard model of *particle physics*, (2) dark matter, which has mass but very little interaction (other than gravity), if any, with ordinary matter, and (3) dark energy, which accelerates the expansion of the universe.

The ΛCDM model is still only a *model* because we do not have direct evidence of its validity, nor do we understand the fundamental nature of dark matter and dark energy for now. Nevertheless, with this model, we can successful explain the evolution of the universe, the seen Large-Scale Structures (LSS) of galaxies, and also the measured Cosmological

---

[1] More precisely, neutrinos are not considered as "baryons" in cosmologists' language.

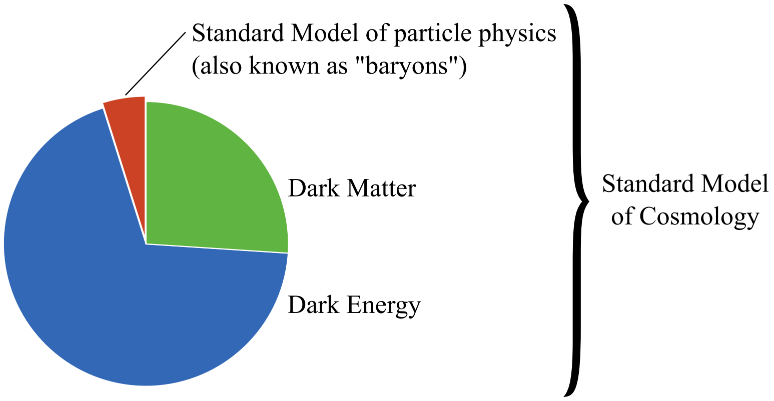

Figure 1.1: Three main components in the total mass-energy budget of the universe: ordinary matter ("baryons[1]"), dark matter, and dark energy.

Microwave Background (CMB). If we assume the ΛCDM model is correct, these observations in return constrain how much each component constitute of the total mass-energy budget of the universe. From the latest results of a series observations, including the Planck CMB observations, we can derive that there are $\sim$ 69.1% of dark energy, $\sim$ 26.0% of dark energy, and only $\sim$ 4.9% of ordinary matter (Planck Collaboration et al., 2015). Figure 1.1 illustrates this distribution.

The aforementioned indirect evidences have made the ΛCDM model widely accepted, and advanced the field of cosmology into the era of *precision cosmology*. Today, plenty of challenges still lie in modern cosmology, including: to find direct evidence of dark matter and dark energy, to understand the nature of dark matter and dark energy, to probe discrepancies between observation and ΛCDM prediction that may indicate new physics, and to learn the complex physical processes involved in galaxy formation. To tackle these challenges, not only do we need further astronomical observations, but also require new advances in the department of theories and simulations.

1.2 Modeling Dark Matter

This dissertation, as its title suggests, focuses on the study of dark matter. Dark matter was proposed in 1930s to explain the mismatch between the estimated total mass and the light of galaxy clusters. Modern observations suggest that dark matter constitutes $\sim 84\%$ of the total mass (i.e., not including dark energy) in the universe, dominating the distribution of matter. However, dark matter does not interact with ordinary matter (or only extremely weekly) in anyway way other than its gravitational influence. Dark matter leaves gravitational footprints on the ordinary matter, such as galaxy rotation curves, the gravitational lensing effect, and the spatial distribution of galaxies.

We now know that dark matter is the building block of the universe. Dark matter forms the cosmic web, and all visible galaxies are formed within the deep gravitational potential of clumps of dark matter, also known as dark matter *halos*. For a typical galaxy such as the Milky Way galaxy, the halo it resides in is about ten times more massive in mass, with the galaxy sitting at the very center of the halo.

Hence, the distribution of dark matter and the evolution of dark matter halos are both crucial components in our understanding of the nature of dark matter and the physics of galaxy formation. However, due to the obscure nature of dark matter, the distribution of dark matter is not directly observable. As a result, studies of dark matter usually rely heavily on numerical simulations, in which we can create a *model* universe and observe how dark matter distributes itself within this model universe.

The machinery of our universe has an incredibly large dynamical range, down to sub-atomic scales and up to super-galactic scales. It is, evidently, impossible to simulate a fake universe with all these scales properly implemented. A common practice is to conduct the so-called “dark matter-only” simulations. It should be clarified that, although this kind of simulation is named “dark matter-only”, they do include both dark energy (so that the universe expands acceleratingly) *and* ordinary matter, but assume that the ordinary matter behaves like dark matter does gravitationally. Since dark matter does not interact with ordinary matter nor itself except via gravity, this kind of simulation is more computationally affordable. Also, because dark matter dominates the mass of the universe, the matter distribution in dark matter-only simulations still resembles the real matter distribution very closely, at least on super-galactic scales.

Despite the predictive power of these numerical simulations, in practice, simulations alone are far from enough for the study of dark matter. For reasons I will elaborate below, mathematical models that *empirically describe* the distribution or the behavior of dark matter are also essential ingredients. In this dissertation, I construct several empirical models that describe various aspects of the dark matter distribution and of the connection between dark matter and visible galaxies. These models are based on numerical simulations, and have wide-ranging applications, as I will demonstrate in each chapter of this dissertation.

1.3 Why do we need empirical models?

For now, I shall first explain why empirical models are necessary despite the fact that we can already access a good number of dark matter simulations. The reasons can be summarized as follows:

1. *Facilitating applications.* Dark matter simulations provide "mock" universes where we can directly sample the phase-space distribution of dark matter and dark matter halos. However, for most applications, it is more convenient, usually for implementational purposes, to work with a functional form of the desired distribution. The functional form should capture the essential features of the distribution, and in most cases, also smooth out the noise.

   For example, experiments that search for the rare event of collisions between dark matter particles and nuclei require the knowledge of the local velocity distribution of dark matter. Since this velocity distribution is not directly observable in the real universe, one has to assume a specific distribution for these experiments, and preferably a parametrized functional form as this distribution would enter the post-analysis, and it would be easier to work with a parametrized function.

2. *Exploring universality and physical origins.* In dark matter simulations, we have observed various universalities and self-similarities — the spatial distribution of dark matter, the velocity distribution of dark matter, and the subhalo abundance function, to name a few. These universalities are often manifested in the mathematical models, and they also provide new insight for the physical origin of the distribution in consideration.

   Furthermore, the parameters of an empirical model can hint at what the controlling physical quantities are, and facilitate the construction of a first-principle model or the identification of the dominant physical processes. Parametrized models help us understand the physics that hides in the plain simulations.

3. *Extrapolating beyond the capacity of simulations.* Even for the state-of-the-art cosmological dark matter-only simulations, the tracer particles that discretize the density fields of dark matter have a mass of the order of $10^7\ M_\odot$, which is at least 10^{60} times more massive than a typical hypothetical dark matter particle (lighter then 1 TeV/c^2). Hence, these simulations are far from resolving all the small-scale structures.

   For the purpose of studying the large-scale structures, the resolution of these simulations are often sufficient. Yet from time to time we need to utilize the current simulations in a regime that is not fully resolved due to computational limitation. In this case, it is more reliable and robust to extrapolate the distribution based on a physically motivated model, rather than to use the distribution measured directly from simulations, because the latter, by definition, suffers from the resolution limitation. In this way, empirical models help extending the capacity of existing simulations.

4. *Estimating systematic uncertainties.* Many sources contribute to the systematic uncertainties when we use simulated universes to approximate the real universe. For example, the cosmology used in the simulation can differ from the actual cosmology.

For a fixed cosmology, a single simulation is only *one* realization of a universe, and hence what we measure in any simulation would resemble the real universe only in a *statistical* sense even if the cosmology is exactly correct. Also, because dark matter halos are not direct observable, in the real universe we can only infer the halo properties from other observables, and hence it is also important to understand the possible systematic errors in the inference.

Parametrized empirical models help estimating these systematics uncertainties. By evaluating the parameters, we can calculate the scatter due to random realization and also examine if there is any factor which correlates with the scatter and may result in a bias. In other words, the models help constructing the statistical priors according to the ΛCDM description.

5. *Connecting direct observables and the mock universes.* Despite the success of the ΛCDM model, a dark matter-only simulation still does not fully represent the universe we *observe*. Since the ordinary matter in a dark matter-only simulation is assumed to have only gravitational interaction, the ordinary matter does not form stars nor galaxies. In order to map these observables to the predictions from dark matter-only simulations, we need a prescription of how the observables, such as galaxies, trace the dark matter distribution.

   One way to obtain this prescription is to conduct hydrodynamical simulations. Hydrodynamical simulations include baryonic physics to a certain extend, so they require much higher resolution and are more computational expensive than their dark matter-only counterpart. With the limited computation resources, hydrodynamical simulations usually fall short of the simulated volume, which is critical for understand the sample variance. Also, hydrodynamical simulations do not have infinite resolution, even state-of-the-art hydrodynamical simulations still cannot resolve individual stars. As a result, subgrid physical models are still needed in hydrodynamical simulations to prescribe the unresolved processes.

   A very different approach to bridge the observables and the predictions from dark matter-only simulations is to directly model the galaxy–halo connection. This approach links the observed galaxy distribution and the simulated distribution of dark matter halos on a statistical basis. This kind of empirical models is particular useful to constrain the statistical relationship between galaxies and dark matter halos. By revealing the relationship, we can learn about the galaxy formation physics.

The above reasons should have made a strong case for why empirical models are necessary for the study of dark matter, galaxy formation, and cosmology. We should, however, carefully distinguish between a empirical model, a physical law, and a fitting function, despite their blurred boundaries. Empirical models can by no means replace a detailed, first-principle physical model, nor to be taken as the underlying physical laws or principles. A physical law usually represents some fundamental understandings of a *collection* of physical problems, while an empirical model provides strategies to tackle *specific* problems. From a different aspect, empirical models can also be seen as the macroscopic effective theory for the problems at hand. Furthermore, an empirical model is *more* than a fitting function because empirical models need to capture the essential trends and correlations so that they provide insight into the physical problems in consideration. For example, a spline fit is apparently a fitting function, but an empirical model should have the correct asymptotic behaviors as we would expected from the physics.

1.4 The cases

In this dissertation, I will discuss three particular aspects of dark matter distribution and its connection to galaxies: (1) the local velocity distribution, (2) the abundance of dark substructures, and (3) the flexibility in the galaxy–halo connection. Here I briefly explain our motivations, goals, and main findings of these studies.

1. *Local velocity distribution.* Direct detection experiments search for signals of the weak interaction between dark matter particles and nuclei, and the event rate of this rare collision depends on the local velocity distribution of dark matter. Since there

is no independent observation which can reveal the velocity distribution, it becomes one of the assumptions when we interpret the results. Conventionally, it is assumed to follow the Maxwell–Boltzmann distribution, although numerical simulations suggest otherwise. To understand how much the assumed velocity distribution impacts the interpretation, I developed an empirical model for the velocity distribution which encompasses the predictions from N-body and hydrodynamical simulations. With this model and the simulations, I further constructed priors on the model parameters, and then quantified the systematic uncertainties in direct detection experiments due to the lack of knowledge about the distribution.

2. *Dark substructures.* One of the unique predictions of ΛCDM is the existence of abundant dark matter subhalos. While subhalos are not directly observable, they can produce detectable perturbations in radio or optical strong-lensed systems, and some of the dark subhalos could host ultra-faint dwarf galaxies. These observables can constrain the properties of the halo in consideration, and even test the validity of ΛCDM model, when the subhalo abundance is properly modeled. Traditionally the abundance of subhalos is modeled to be a Poisson random variable which depends on only the host halo mass. However, studies have shown that halo formation time would impact subhalo abundance. In light of this, I developed a model which predicts the subhalo abundance based on the mass and concentration of the host halo, and demonstrated that the Poisson scatter results from small-scale perturbation when the large-scale properties, particularly halo mass and concentration, are fixed. This model not only extend the utility of current simulations beyond their resolution limits, but also provides a more accurate description of subhalo abundance.

3. *Galaxy–Halo Connection.* The "abundance matching" technique connects dark matter halos with galaxies on the assumption that the luminosity of galaxy varies with a halo property, such as mass, approximately monotonically. With this simple assumption, we can populate galaxies on a large dark matter-only simulations to generate a comparable volume of mock observation with limited computational resource, which

is critical for utilizing the data from large-area surveys such as the Sloan Digital Sky Survey. I am conducting a series of studies on the flexibility of abundance matching, investigating how the choice of the halo property used in abundance matching affects the galaxy clustering and other observables. For example, we found that the concentration dependence in abundance matching can be parameterized and constrained by the two-point correlation functions of luminosity-selected samples. This result can further be used to constrain the physics in semi-analytical models and hydrodynamical simulations.

The dissertation is arranged as follows: In Chapter 2 I describe the simulations used in this dissertation. In Chapter 3 I review the notion of dark matter halos and the universal density profile of halos and its connection to halo formation histories, as this topic is essential ingredient in the following chapters. In Chapters 4, 5, and 6, I present the main results of, respectively, the local velocity distribution, the abundance of dark substructures, and the flexibility in the galaxy–halo connection, as described above. A brief summary and future outlook are presented in Chapter 7.

Chapter 2

Dark Matter Simulations

This chapter describes the simulations used in this dissertation. Many of these simulations are carried out by my collaborators and colleagues, including Matthew Becker (for the "Chinchilla" Simulations), Anatoly Klypin and the MultiDark/Bolshoi Project[1] (for the "MultiDark/Bolshoi" Simulations), Hao-Yi Wu and Oliver Hahn (for the "Rhapsody" Simulation), and Samuel Skillman, Mike Warren, and Matt Turk (for the "Dark Sky" Simulations). I also thank Peter Behroozi for providing the halo catalogs and merger trees for the "MultiDark/Bolshoi" Simulations, and thank Marc Williamson for helping conducting the new series of zoom-in simulations of Milky Way-mass halo. Relevant references will be given in the main text.

Abstract Dark matter simulations provide robust and scalable predictions of the matter distribution under the ΛCDM paradigm, upon which modern galaxy formation theory is built. In order to span a wide dynamical range and to collect a statistical sample of dark matter halos of different characteristics, we use several series of cosmological and zoom-in simulations, for the development of analytical models that describe the features of these simulations. In addition, we study the resolution requirements for modeling the two-point correlation functions, which is essential for extracting information about dark matter and

---

[1] https://www.cosmosim.org/cms/simulations/multidark-project/

Series/box name	h	Ω_M	n_s	σ_8	Code
Chinchilla	0.7	0.286	0.96	0.82	L-Gadget2
`Bolshoi`	0.7	0.27	0.95	0.82	Art
`BolshoiP`	0.678	0.295	0.968	0.823	Art
`MDPL2`	0.678	0.307	0.96	0.823	L-Gadget2
Dark Sky	0.688	0.295	0.968	0.834	2Hot

Table 2.1: List of the cosmologies and codes of cosmological simulations

dark energy from large-scale surveys.

2.1 Cosmological Simulations

Dark matter-only simulations discretize the underlying dark matter density field with tracer particles, and use a gravity solver to solve the motions of these tracer particles. The initial condition of these tracer particles are given by the linear perturbation theory, with a specific cosmology. A cosmological dark matter-only simulations commonly has a cubical volume with a periodic boundary condition (and hence commonly referred to a *box*). The mass resolution of a cosmological simulation is defined as the mass of each tracer particle, which is given by $\rho_M L^3/N$, where ρ_M is the total matter density of the Universe, L is the side length of the cubical volume, and N is the total number of particles.

With modern implementations of the gravity solver, the computational cost of a dark matter-only simulation is approximately proportional to $N \log N$. Hence, given limited computational resources, it is always a trade-off between a higher mass resolution and a larger volume. The higher the resolution, the more details about individual dark matter halos one could learn. The larger the volume, the more precise statistics of dark matter halos one could derive. In practice, one usually need to utilize several cosmological boxes to span a wide dynamical range. In my dissertation I used three different series of cosmological simulations. They have different cosmology parameters and also use different N-body solvers, as listed in Table 2.1.

All the simulations in the “Chinchilla” series (M. R. Becker, in preparation), as listed

Box name	Side length [Mpc h^{-1}]	Particle number	Particle mass [$M_\odot h^{-1}$]
`c125-2048`	125	2048^3	1.80×10^7
`c125-1024`	125	1024^3	1.44×10^8
`c250-2048`	250	2048^3	1.44×10^8
`c250-1024`	250	1024^3	1.15×10^9
`c250-768`	250	768^3	2.74×10^9
`c250-512`	250	512^3	9.24×10^9
`c400-2048`	400	2048^3	5.91×10^8
`c400-1024`	400	1024^3	4.73×10^9
`c400-768`	400	768^3	1.12×10^{10}

Table 2.2: List of the “Chinchilla” boxes

Box name	Side length [Mpc h^{-1}]	Particle number	Particle mass [$M_\odot h^{-1}$]
`Bolshoi`	250	2048^3	1.35×10^8
`BolshoiP`	250	2048^3	1.49×10^8
`MDPL2`	1000	3840^3	1.51×10^9

Table 2.3: List of the “MultiDark/Bolshoi” simulations

in Table 2.2 all have the same cosmology but different resolutions and box sizes. They are also all run with the L-Gadget2 code, a variant of Gadget2 (Springel, 2005). The multiple resolutions and box sizes enable a study of resolution requirement.

The “MultiDark/Bolshoi” series has several boxes with different cosmology parameters, resolutions, box sizes, and codes (Klypin et al., 2011, 2014). In this dissertation, we use three boxes from this series: `Bolshoi`, `BolshoiP`, and `MDPL2`, as listed in Table 2.1 and Table 2.3. `Bolshoi` and `BolshoiP` were run with the ART N-body code (Klypin et al., 2011), and `MDPL2` was run with L-Gadget2.

The “Dark Sky” Simulations were introduced in Skillman et al. (2014). This suite is run with the 2HOT code (Warren, 2013). The simulations used in this work, `DarkSky-250`, `DarkSky-400`, and `DarkSky-Gpc`, are companion simulations of the original 8 Gpc h^{-1} box. They all have the same cosmology, but different sizes and particle masses, as listed in Table 2.4. In order to build the merger trees for the `DarkSky-Gpc` box, we down-sampled

Box name	Side length [Mpc h^{-1}]	Particle number	Particle mass [$M_\odot h^{-1}$]
`DarkSky-250`	250	2560^3	7.63×10^7
`DarkSky-400`	400	4096^3	7.63×10^7
`DarkSky-Gpc`	1000	$3225^{3\,\dagger}$	1.53×10^8

Table 2.4: List of the "Dark Sky" Simulations. (†The original `DarkSky-Gpc` box has 10204^3 particles.)

the box by 1/32. The original `DarkSky-Gpc` box has 10204^3 particles.

Figure 2.1 shows the mass resolutions and volumes of the aforementioned simulations and also other start-of-the-art large-scale simulations. From the figure, we can see clearly that the simulations lie on a diagonal band, which represents the trade-off between high resolution (toward upper left) and larger volumes (toward lower right). The black diagonal line represents simulations that have a trillion particles, which is approximately the current limit for a single cosmological box due to limited computing power.

2.2 Zoom-in Simulations

The finite computation resource limits the resolution or the volume of a cosmological simulation, as we discussed above. However, both high resolution and a large volume are desired features. The higher the resolution, the more details about individual halos one could learn. The larger the volume, the more statistics of halos one could have. Many studies do require both high resolution and large statistics, so that one can not only the see detailed distribution of dark matter but also estimate the halo-to-halo scatter or the sample variance. For these studies, the zoomed-in simulations are especially useful.

A zoom-in simulation focuses the computational power on a small region of a full cosmological box, by using tracer particles of different masses. To achieve this, we first run a low-resolution cosmological simulation, and identify the regions of interest, commonly the regions occupied by specific dark matter halos. We then find the Lagrangian volume in the initial condition which corresponds to the region we want to zoom in on. Then we

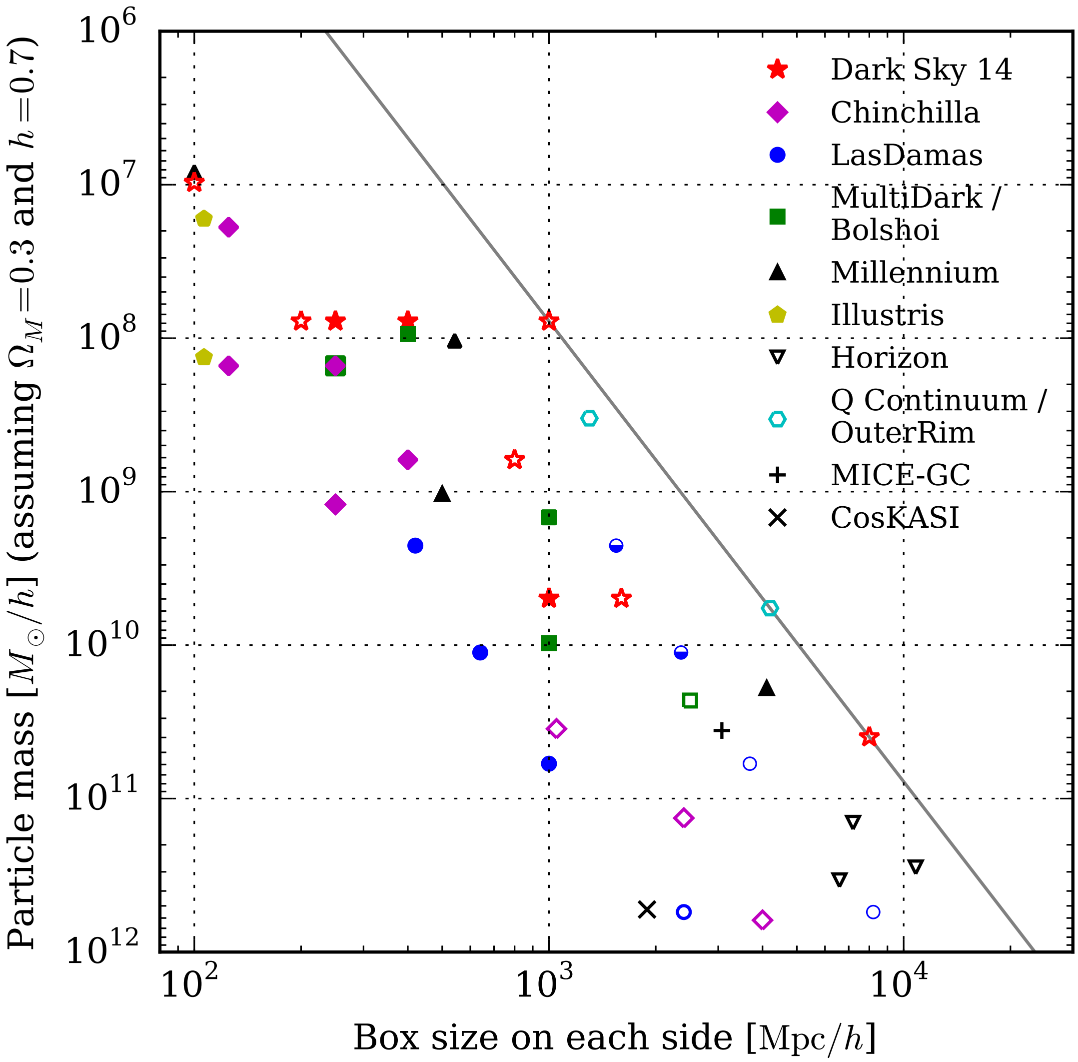

Figure 2.1: The mass resolutions and box sizes of various simulations. The black diagonal line represents simulations that have a trillion particles.

Simulation	h	Ω_M	n_s	σ_8	L [Mpc/h]	$N_{\rm part}^{\rm base}$	$N_{\rm part}^{\rm eff}$	$N_{\rm halos}$
`Rhapsody`	0.7	0.25	1.0	0.8	1000	1120^3	8192^3	96
MW Zoom-in	0.7	0.286	0.96	0.82	125	1024^3	8192^3	46

Table 2.5: List of the cosmology parameters, box sizes, and resolutions for the zoom-in simulations.

regenerate the initial condition with the publicly available Music code[2]. Music would preserve the large-scale fluctuation in the original cosmological simulation (commonly refereed to as "parent box" or "base box"), and put down the initial condition as layers of different resolutions, with the highest in the Lagrangian volume we identified, and gradually decreasing outwards (Hahn & Abel, 2011). Once the initial condition is correctly generated, we can use the conventional gravity solvers to conduct the simulations.

In this dissertation I use two suites of zoom-in simulations, as listed in Table 2.5. The `Rhapsody` suite consists of 96 zoom-in simulations on cluster-size halos of a mass $\sim 10^{14.8}\, M_\odot h^{-1}$, with the mass of the highest-resolution particles being $1.3 \times 10^8\, M_\odot h^{-1}$ (for more details, see Wu et al., 2013b,a). The halos in the `Rhapsody` suite are selected from the base box, `Carmen` simulation, from the `LasDamas` suite[3].

We also conducted a new suite of zoom-in simulations that consists of 46 Milky Way-size halos of a mass $\sim 10^{11.9}\, M_\odot h^{-1}$ (Mao et al., 2015). The mass of the highest-resolution particles in the zoom-in simulations is $3.0 \times 10^5 M_\odot h^{-1}$. The base box for this new suite is `c125-1024`. See Section 5.2 for more details. Figure 2.2 shows a visualization of one of the halos in this new suite, with the tetrahedral tessellation method (Kaehler et al., 2012). The full volume spanned by the high-resolution particles are shown in the picture, with the main Milky Way-size halo sitting at the center (the rounded structure with the bright color).

---

[2] `https://bitbucket.org/ohahn/music`

[3] `http://lss.phy.vanderbilt.edu/lasdamas/`

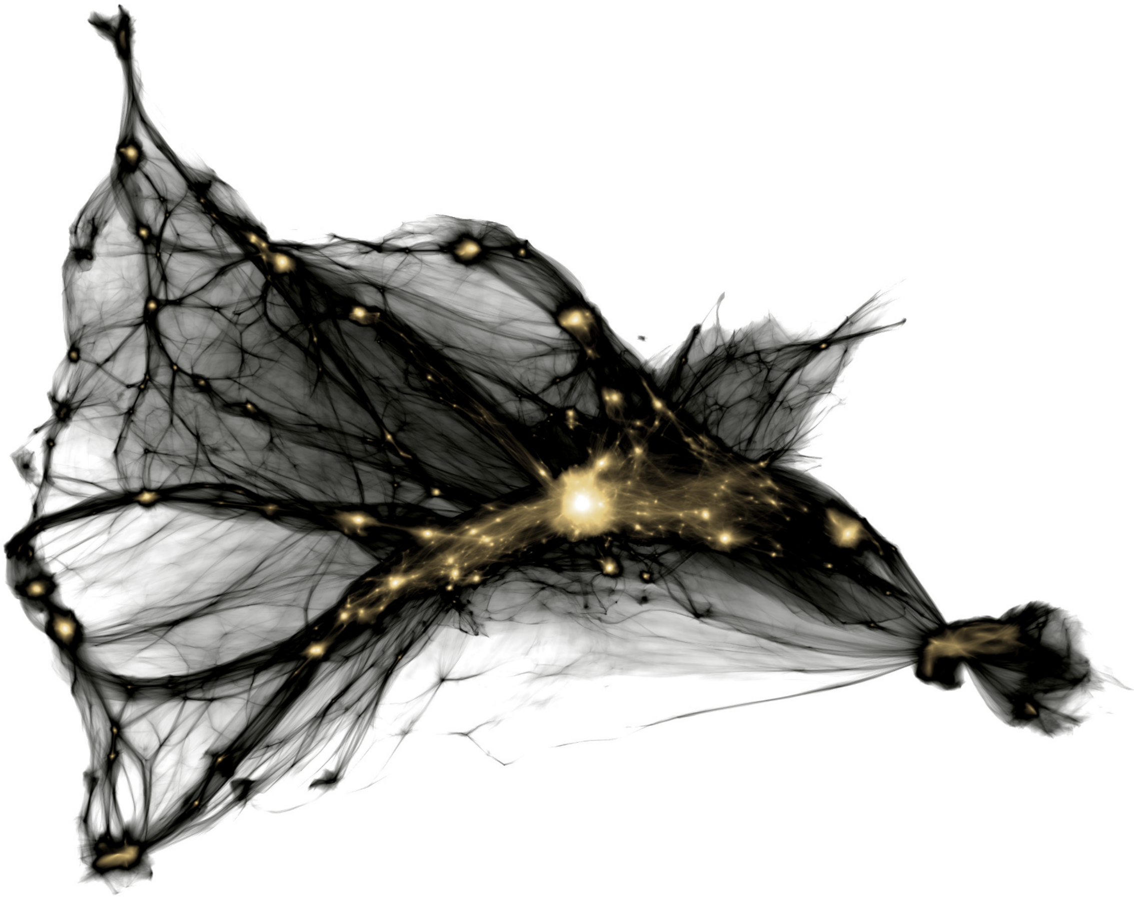

Figure 2.2: A visualization of one zoom-in simulation of a Milky Way-size halo. The visualization is done by Ralf Kaehler, with the tetrahedral tessellation method (Kaehler et al., 2012). The figure shows the full volume spanned by the high-resolution particles, which is much larger than the halo of interest. The halo appears in this rendering as a rounded object at the very center of the volume (the bright color).

2.3 Simulation Post-processing

While the N-body simulations provide the distribution of dark matter and its evolution, further processes are needed to identify dark matter halos. Dark matter halos are overdensities of dark matter. They are identified by finding density peaks in the distribution of dark matter. The halo finding process is a critical step in the simulation post-processing, because halos are considered the basic unit in almost all modern research on dark matter, including this dissertation.

To ensure consistency, in this dissertation, we use Rockstar[4] all halo finding procedures. Rockstar is a phase-space halo finder, which better distinguishes halos that are overlapping in space (Behroozi et al., 2013a). We also always use spherical overdensity to define the boundary of a dark matter halo. And we use $\Delta_{\rm vir}$ as the halo boundary definition (see Section 3.1 for more details about halo boundary definition). At $z = 0$, for the cosmology we considered in Table 2.1, $\Delta_{\rm vir} \approx 100$; that is, the averaged density of a halo is 100 times the critical density.

In order to understand how halos evolve with time, we also need to build halo merger trees. In this dissertation, we use Consistent Trees[5] for tree building. For each halo present at $z = 0$, Consistent Trees first creates a preliminary merger tree by link halos at different epochs with the particle information, and then gravitationally evolves the halos to remove spurious links in the trees (Behroozi et al., 2013b).

Also, I developed a Python module “SimulationAnalysis[6]” to facilitate the access to the final products (halo catalogs and merger trees) of Rockstar and Consistent Trees.

The choice of halo finder and tree builder affects all analyses that base on dark matter halos. Ideally, different halo finders and tree builders should produce consistent results when they analyze the same set of simulations. Efforts have been made to compare different halo finders and tree builders (see e.g., Onions et al., 2012; Srisawat et al., 2013; Avila et al., 2014). While difference still exists between different halo finders and tree builders,

---

[4] `https://bitbucket.org/gfcstanford/rockstar`

[5] `https://bitbucket.org/pbehroozi/consistent-trees`

[6] `https://bitbucket.org/yymao/helpers`

the combined use of Rockstar and Consistent Trees in general produces reliable halo catalogs and merger trees, and the resulting statistical properties of dark matter halos are usually consistent with other modern phase-space halo finders.

Chapter 3

The Density Profile of Dark Matter Halos

Abstract Dark matter halos are overdensities in the distribution of dark matter. They are the building blocks of the cosmic webs and the nests of galaxies. Dark matter halos are commonly characterized by their density profiles. In ΛCDM simulations, it has been found that the density profiles of halos can be described by a universal functional form, the Navarro–Frenk–White profile, in which case one can use only two parameters, mass and concentration, to describe a halo. In ΛCDM simulations, it is also known that the mass and the concentration of halos are correlated, and they are also correlated with halo formation history. In this chapter, we briefly review this universality of the halo density profile and models that explain the mass–concentration relation. We then propose a toy model to show how the mass–concentration relation can emerge from simple assumptions of a relation between the density profile and halo mass function.

3.1 Introduction: A Universal Density Profile

Dark matter halos are the spherical overdensities in the distribution of dark matter. Halos are characterized by the density peak (center), and mass (boundary), and the density profile, which is the density as a function of radius with respect to the halo center. The density profile of dark matter halos has been studied extensively, and it has been proposed and shown in simulations that the density profiles of halos are in a universal two-parameter family, the Navarro–Frenk–White (NFW) profile (Navarro et al., 1996, 1997).

The NFW density profile has been adopted widely to describe the dark matter halos in both simulations and observations. The NFW profile is characterized by two parameters, the the scale radius r_s and the scale density ρ_s, in this functional form:

$$\rho(r) = \frac{\rho_s}{(r/r_s)(1+r/r_s)^2}. \tag{3.1}$$

The scale density is by definition the density at the scale radius $\rho(r_s) = \rho_s$. The logarithmic slope of density for the NFW profile is

$$\frac{d\ln\rho}{d\ln r} = -\frac{1+3r/r_s}{1+r/r_s}. \tag{3.2}$$

This logarithmic slope goes asymptotically to -3 as $r \to \infty$ and to -1 as $r \to 0$, and it equals -2 when $r = r_s$.

Other functional forms were also proposed to describe the density profile of dark matter halos, and they can be categorized into two families: the generalized NFW model (generic double power law) and the generalized Einasto profile (An & Zhao, 2013).

Note that when comparing the scale radii in different models of the density profile, one should compare the radii which all correspond to a given logarithmic slope but not the scale radii in their nature parameterization forms because the latter can be arbitrarily defined. Hereafter the term "scale radius" and the symbol r_s will always refer to the radius where logarithmic slope equals -2, despite of the specific model of the density profile assumed.

It is physically motivated to choosing the radius where logarithmic slope equals -2 as the scale radius. N-body simulations generally have shown two phases of the growth of a halo. The first phase is the gravitational collapse or fast-accretion phase. In this phase the logarithmic slope is shallower than -2 and the scale radius increases as the halo grows. The second phase is slow-accretion phase, in which the scale radius stays at a constant physical value, and the virial radius increases as the halo grows, building up a steeper logarithmic slope on the outskirts (Lu et al., 2006).

The concentration parameter c is defined as the ratio of the virial radius to the scale radius. Because different mass definitions result in different virial radii, a good definition of concentration parameter should specify the mass definition as well. Given the scale radius and the virial mass M_Δ, the relation between the concentration parameter and the mass definition is independent of the density profile.

$$c = \frac{R_\Delta}{r_s} = \frac{1}{r_s}\left[\frac{M_\Delta}{(4\pi/3)\Delta\rho_{\rm cirt}}\right]^{1/3}, \tag{3.3}$$

where Δ is the overdensity of a halo with respect to the critical density for a certain mass definition (e.g., $200c$, $500c$, virial).

Since the NFW density profile is a two-parameter model, one can fully determine the parameters (r_s, ρ_s) by specifying the concentration and mass given one mass definition. r_s can be calculate from (c, M) with Equation 3.3, which is independent of the density profile. ρ_s can be calculated from solely c, and for the NFW profile their relation is

$$\left(\frac{\rho_s}{\rho_{\rm cirt}}\right)\left[\frac{\ln(1+c)}{c^3} - \frac{1}{c^2(1+c)}\right] = \frac{\Delta}{3}. \tag{3.4}$$

From Equations 3.3 and 3.4, we can also write down the relation between the virial mass M_Δ and the "scale mass", which is defined as

$$M_s \equiv \frac{4\pi}{3}\rho_s r_s^3, \tag{3.5}$$

$$M_\Delta = 3M_s\left[\ln(1+c) - \frac{c}{(1+c)}\right]. \tag{3.6}$$

Given a specific density profile $\rho(r)$, we can also fully determine the circular velocity as a function of radius $v_{\rm circ}(r) = \sqrt{GM(<r)/r}$. We define $v_{\rm vir}$ to be the circular velocity at

virial radius. For the NFW profile, we have

$$v_{\rm vir} \equiv v_{\rm circ}(r_{\rm vir}) = \left[\frac{3GM_s}{r_s}\left(\frac{\ln(1+c)}{c} - \frac{1}{1+c}\right)\right]^{1/2}. \tag{3.7}$$

We also define $r_{\rm max}$ to be the radius at which $v_{\rm circ}$ has a maximum, and then we have

$$\left.\frac{dv_{\rm circ}(r)}{dr}\right|_{r=r_{\rm max}} = 0 \Rightarrow r_{\rm max} \simeq 2.16258\, r_s, \tag{3.8}$$

and

$$v_{\rm max} \equiv v_{\rm circ}(r_{\rm max}) \simeq \sqrt{0.2162166\,\frac{3GM_s}{r_s}}, \tag{3.9}$$

Hence, we have found another set of parameters $(v_{\rm max}, v_{\rm vir})$ that can fully determine the density profile (see also Klypin et al., 1999a). In particular, from $v_{\rm vir}$ one can infer $M_{\rm vir}$, and from the ratio of $v_{\rm max}$ and $v_{\rm vir}$ one can infer the concentration parameter:

$$\frac{v_{\rm max}}{v_{\rm vir}} = \left[0.2162166\left(\frac{\ln(1+c)}{c} - \frac{1}{1+c}\right)^{-1}\right]^{1/2}. \tag{3.10}$$

In Chapter 5 and Chapter 6 we will use this set of parametrization $(v_{\rm max}, v_{\rm vir})$ extensively.

3.2 The Concentration–Mass Relation and Halo Formation History

As we already discussed, the NFW profile can be characterized by halo concentration and mass (c, M). If we now look at the correlation between these two parameters for all the halos that we identified in a dark matter simulation, we find that halo concentration and mass are highly correlated: high-mass halos have lower concentrations (Navarro et al., 1997). This correlation is known as the halo concentration–mass relation.

Furthermore, at a given halo mass, halo concentration also correlates with halo formation history (e.g., Wechsler et al., 2002). This correlation suggests some connections between the seen concentration–mass relation and halo formation histories. Many efforts have been made in finding toy models that relate halo formation histories and the concentration–mass relation. In particular we review the toy models proposed by Navarro et al. (1997, hereafter NFW97), Bullock et al. (2001, hereafter Bullock01), Wechsler et al. (2002, hereafter Wechsler02), and Macciò et al. (2008, hereafter Maccio08). The basic underlying ideas of these models are all the same, which is to define a "collapse epoch", denoted by a_c hereafter, for each individual halo or for halos of a certain mass. Once the collapse epoch is defined, the toy models then relate the concentration parameter to the collapse epoch.

These models define the collapse time differently. For a halo with mass M at the observing time a_0, NFW97 assign the collapse time to be the epoch at which half the mass of the halo was first contained in progenitors more massive than a fixed fraction F_1 of the mass of the halo at the observing epoch a_0.

$$\operatorname{erfc}\left(\frac{\delta_{\rm cirt}/\left[D(a_c)-D(a_0)\right]}{\sqrt{2\left[\sigma^2(F_1 M)-\sigma^2(M)\right]}}\right)=\frac{1}{2}, \tag{3.11}$$

where $\delta_{\rm cirt} \simeq 1.686$ is the critical overdensity, $D(a)$ is the linear growth rate, and $\sigma(M)$ is the squared root of the mass variance (at $a = 1$) with a top-hat filter of mass M. Note that Equation 3.11 specifies the same a_c for all halos with the same M at epoch a.

Bullock01 revised the NFW97 model by simply assigning the collapse epoch a_c to the the epoch when the typical collapsing mass equals to a fixed fraction F_2 of the mass M at the observing epoch a_0, that is,

$$\sigma(F_2 M)D(a_c) = \delta_{\rm cirt}. \tag{3.12}$$

In this model, halos with the same mass are also assigned the same a_c like in the NFW97 model. However, the observing epoch a_0 enters this relation only implicitly through the halo mass M, resulting in different behaviors between the Bullock01 model and the NFW97 model. Maccio08 used the same method as Bullock01.

Wechsler02 assigned the collapse epoch directly from the accretion history of each halo.

The accretion history is constructed from the Extended Press-Schechter (EPS) formalism, and then fitted by this function

$$M(a) = M_0 \exp\left[-2a_c\left(\frac{a_0}{a} - 1\right)\right], \tag{3.13}$$

to obtain a_c. This method could assign different a_c to halos have the same mass at the observing epoch.

There are also different methods to relate the concentration parameter to the defined collapse epoch. NFW simply related the scale density to the matter density of the universe at the collapse epoch

$$\frac{\rho_s}{\rho_{\text{cirt}}} = \frac{K_1 \Omega_{M,0}}{a_c^3}, \tag{3.14}$$

where K_1 is a fixed constant, and for the NFW profile the relation between the concentration parameter and the scale density is given by Equation 3.4.

On the other hand, Bullock01 and Wechsler02 directly related the concentration parameter to the collapse epoch

$$c = K_2 \frac{a_0}{a_c}, \tag{3.15}$$

where K_2 is a fixed constant, to relate the concentration parameter to the collapse epoch. Maccio08 slightly modified this relation by taking into account the mass definition

$$c = K_3 \left[\frac{\Delta(a_c)\rho_{\text{cirt}}(a_c)}{\Delta(a_0)\rho_{\text{cirt}}(a_0)}\right]^{1/3}, \tag{3.16}$$

where K_3 is a fixed constant too.

3.3 Our Toy Model

In the previous section we review four different models that explain the concentration–mass relation by defining a collapse epoch for each halo. Effectively, those models translate the correlation between halo formation time and mass into the correlation between halo concentration and mass, but still leave the correlation between halo formation time and mass unexplained.

On the other hand, efforts have been made to describe the halo mass function and its evolution with time. In particular, the framework of the Press–Schechter model and its variants (e.g., Press & Schechter, 1974; Sheth & Tormen, 1999) provide explicit functional forms to describe the halo mass function at any given redshift, and the framework naturally results in a correlation between halo formation time and mass.

Hence, we propose a toy model that uses the halo mass function to predict the correlation between halo formation time and mass, and hence predict the concentration–mass relation. We will explicitly show how we transform the halo mass function into the joint probability distribution function (PDF) of concentration and mass at different observing epochs, $P(c, M; a_0)$. In general, these steps can be applied to any halo mass function, either derived theoretically or calibrated with simulations. For simplicity, we will only use the Sheth–Tormen halo mass function (Sheth & Tormen, 1999; Sheth et al., 2001) as a working example.

Our model follows the spirit of the models aforementioned, but has a few distinct features. First of all, since we need the distribution of concentration parameter for a given halo mass, we cannot assign a single value of a_c for all halos of the same mass. Instead, we need a method to find the distribution of a_c for halos of the same mass. Wechsler02 achieved this by using the EPS formalism to generate merger trees and then fitted the mass accretion history. In contrast, we simply use the information originally embedded in the halo mass function without assuming a functional form of the mass accretion history.

The second major difference between our model and previous models is that instead of relating the accretion epoch with the halo mass, we relate it directly with the halo *scale radius*. In other words, we equals the scale radius to the characteristic collapsed radius, or the filter radius.

We start with the Sheth–Tormen halo mass function

$$n(M, a)\, d\ln M = \frac{\rho_m}{M} f_{\mathrm{ST}}(\nu(M, a)) \left| \frac{d\ln\sigma(M)}{d\ln M} \right| d\ln M, \tag{3.17}$$

where ρ_m is the matter density,

$$f_{\rm ST}(\nu) = \frac{A}{\sqrt{2\pi}}\left(1 + \frac{1}{\nu^{2q}}\right)\nu e^{-\nu^2/2}, \tag{3.18}$$

$$\nu(M, a) = b\delta_c/[\sigma(M)D(a)], \tag{3.19}$$

and A, q, and b are parameters of the Sheth–Tormen halo mass function. Note that to avoid confusion with the scale factor, we named the last parameter b instead of $\sqrt{a}$ as in the original paper. The functional form also include the Press–Schechter mass function, which can be obtained by setting $(A, q, b) = (0.5, 0, 1)$.

As we mentioned, we need a description of the distribution of the collapse epoch for a given halo radius. We obtain this description by calculating the time derivative of the halo radius function. One can consider this time derivative as the effective halo forming rate, which is the rate halos with a certain characteristic radius appear. Note that this rate can be negative, in which case it means the halos with the particular characteristic radius are merged faster then forming.

By "time derivative" we actually mean the derivative with respect to $\ln a$. The halo forming/merging rate in a given log-radius bin and a given log-scale-factor bin is then

$$\begin{aligned}\mathcal{U}(M, a)\, d\ln a\, d\ln M \equiv \frac{dn(M, a)}{d\ln a}\, d\ln a\, d\ln M = \\ \frac{\rho_m}{M} f'_{\rm ST}(\nu(M, a))\left(\frac{d\ln D}{d\ln a}\right)\left|\frac{d\ln\sigma}{d\ln M}\right| d\ln a\, d\ln M,\end{aligned} \tag{3.20}$$

where

$$f'_{\rm ST}(\nu) = -\frac{d\, f_{\rm ST}(\nu)}{d\ln\nu} = \left(\frac{2q}{1+\nu^{2q}} + \nu^2 - 1\right) f_{\rm ST}(\nu). \tag{3.21}$$

Once we have the effective halo forming rate, $\mathcal{U}(M, a)$, we then make the following assumptions to convent this rate into the joint PDF of the scale mass and scale density, $P(M_s, \rho_s)$. First, both the physical scale radius and the physical scale density of a halo were determined at the time when the halo collapsed a_c, and then have both remained constant since then. Second, the scale mass M_s was set as a constant multiple F of the filter mass

R. Third, the scale density ρ_s was set as a constant multiple K of the matter density at the time when the halo collapsed, as proposed in NFW97. Fourth, halos with the same scale radius all have the same probability to be destroyed (merged into another halo).

The second and the third assumptions give the relations between (M_s, ρ_s) and (M, a_c):

$$M_s = FM \tag{3.22}$$

$$\rho_s = K\rho_{m,0}a_c^{-3}. \tag{3.23}$$

So we can map $\mathcal{U}(M, a)$ to $P(M_s, \rho_s)$,

$$P(M_s, \rho_s; a_0) = \frac{1}{3}\mathcal{N}(M = M_s/F, a_0)\,\widetilde{\mathcal{U}}(M = M_s/F, a_c = (K\rho_{m,0}/\rho_s)^{1/3}). \tag{3.24}$$

Note that in this case the Jacobian is $\frac{1}{3}$. Here $\widetilde{\mathcal{U}} \equiv \max(\mathcal{U}, 0)$. This modification is needed because $\mathcal{U}$ can be negative but the probability cannot, and according to the fourth assumption mentioned above we simply suppress the negative values of $\widetilde{\mathcal{U}}$. As a result, we need to add a prefactor $\mathcal{N}$ to match the original halo radius function, and $\mathcal{N}$ is defined as

$$\mathcal{N}(M, a_0) = \frac{\int_{a=0}^{a_0}\mathcal{U}(M, a)\, d\ln a}{\int_{a=0}^{a_0}\widetilde{\mathcal{U}}(M, a)\, d\ln a}, \tag{3.25}$$

and for the Sheth–Tormen mass function, it is simply

$$\mathcal{N}(M, a_0) = \begin{cases} n(M, a_0)/n(M, a_*), & a_0 > a_* \\ 1, & a_0 \le a_* \end{cases}, \tag{3.26}$$

where a_* is defined by satisfying $f'_{\mathrm{ST}}(\nu(M, a_*)) = 0$, and $f'_{\mathrm{ST}}(\nu)$ is defined in Equation 3.21. Note that in the expressions above, $M = M_s/F$. See Figure 3.1 for an illustration.

To convert $P(M_s, \rho_s; a_0)$ into $P(M_\Delta, c; a_0)$, one need to calculate the Jacobian

$$J = \begin{vmatrix} \partial\ln M_s/\partial\ln M_\Delta & \partial\ln M_s/\partial\ln c \\ \partial\ln \rho_s/\partial\ln M_\Delta & \partial\ln \rho_s/\partial\ln c \end{vmatrix}, \tag{3.27}$$

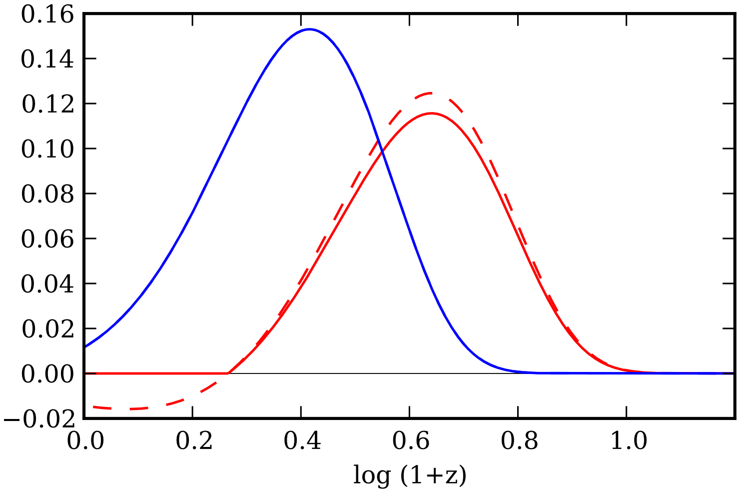

Figure 3.1: Comparison of $R^3\mathcal{U}(R, a)$ (dashed lines) and $R^3\widetilde{\mathcal{U}}(R, a)$ (solid lines) for $R =$ 0.5 (red) and 2 (blue) Mpc. For $R = 2$, the dashed line and solid line are the same.

and one would have

$$P(M_\Delta, c; a_0) = J(M_\Delta, c)\, P(M_s(M_\Delta, c), \rho_s(c); a_0) \tag{3.28}$$

To calculate the Jacobian, a specific density profile need to be assumed. For the NFW density profile, the relations between (M_Δ, c) and (M_s, ρ_s) are given by Equations 3.3 and 3.4. With these relations one can calculate the Jacobian for the NFW profile

$$J_{\mathrm{NFW}} = \frac{\partial \ln \rho_s}{\partial \ln c} = 3 - \frac{c^2}{(1+c)^2\,[\ln(1+c) - c/(1+c)]}. \tag{3.29}$$

With Equations 3.20, 3.21, 3.24, 3.28, and 3.29, we have fully specify our model, which translates the halo mass function into a PDF of halo concentration and mass at any given epoch. Figure 3.2 and Figure 3.3 show the prediction of our toy model: the PDFs of halo concentration conditioned on halo mass at $z = 0$ and the median concentration–mass relation at different redshifts, respectively.

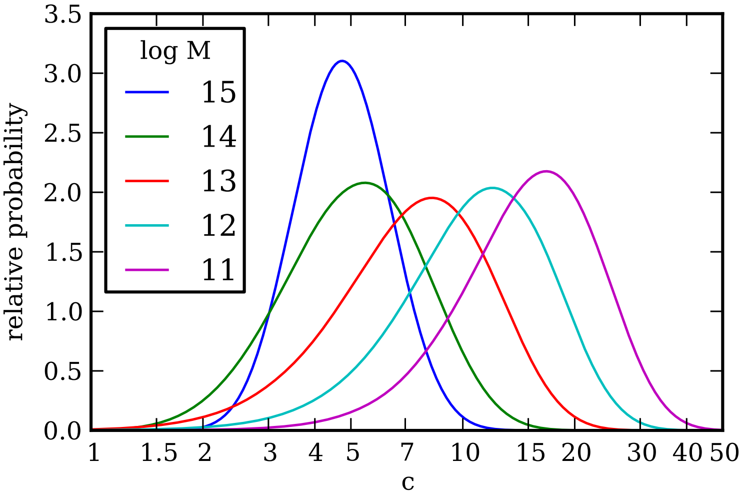

Figure 3.2: The PDFs of halo concentration conditioned on halo mass at $z = 0$, predicted by our model. The five lines of different colors are for $\log_{10}(M_{\rm vir}/\ M_\odot h^{-1}) = 11, 12, 13, 14$, and 15.

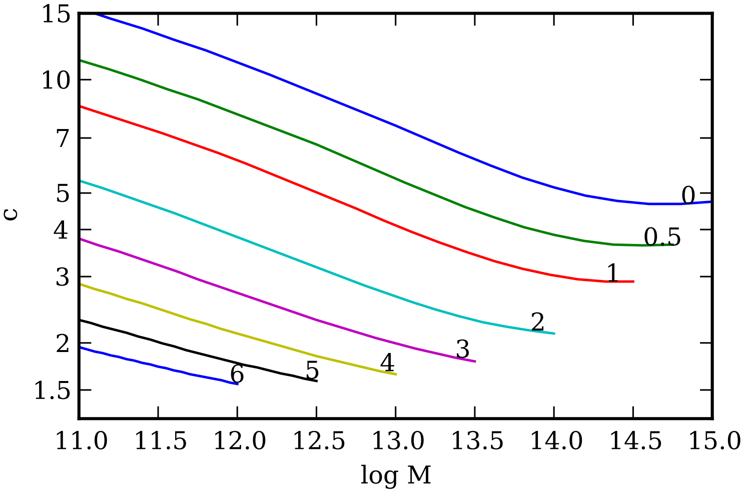

Figure 3.3: The median concentration–mass relation at different redshifts, predicted by our model. The x-axis represents $\log_{10}(M_{\rm vir}/\ M_\odot h^{-1})$.

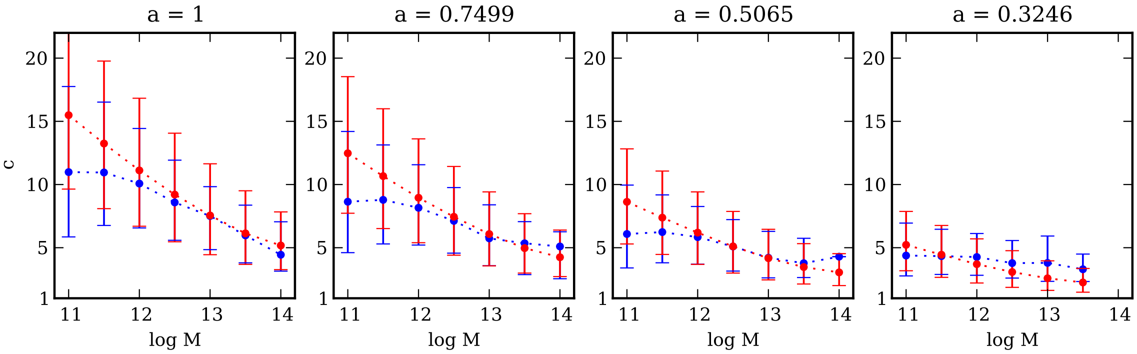

Figure 3.4: Red lines are the concentration–mass relations predicted by our model. Blue lines are obtained from the `Consuelo` simulation from the `LasDamas` suite[3]. Dots denotes the median concentration, and the errorbars denote the concentration values at 16% and 84% for each mass bin. The x-axis represents $\log_{10}(M_{\text{vir}}/\,M_{\odot}h^{-1})$. The four panels show the concentration–mass relation at different redshifts (z = 0, 0.33, 1, and 2, from left to right).

3.4 Comparison with Simulations

A great number of fitting functions and empirical models that describe the concentration–mass relation in simulations already exist (e.g., Macciò et al., 2008; Prada et al., 2012; Dutton & Macciò, 2014; Ludlow et al., 2014; Diemer & Kravtsov, 2015). As I mentioned at the beginning of this chapter, the main purpose of this new toy model is to demonstrate the connection between halo formation histories and halo density profiles, rather than provide a new fit to the concentration–mass relation. Nevertheless, it is still interesting to see how well we can recover the concentration–mass relation in simulations with this model.

Figure 3.4 shows the comparison between the concentration–mass relations in a dark matter simulation and that of our model prediction. We see that this simple toy model provides reasonably good description to both the median and the distribution of concentration as a function of halo mass and redshifts. Given that there are only two free parameters (F and K) in this model (five if including the parameters in the Sheth–Tormen mass function), this result certainly demonstrates the potential of this toy model.

However, we still see discrepancies at low mass, where the model over predicts the concentration. The main reason of this discrepancy is that, the time derivative of the halo mass function does not distinguish the formation and destruction of halos of the same mass. In other words, if at a certain epoch, there are the same number of halos of the same mass form and destroy, the time derivative of the halo mass function at that mass would be zero. However, this cancellation between the formation and destruction of halos does *not* preserve the concentration distribution, as older halos that destroyed would have higher concentration and the newly formed halos would have lower concentration. Hence this cancellation effect results in over predicting the concentration, especially for low-mass halos at low redshifts.

3.5 Summary

We review the universal NFW density profile, and explore different ways to parameterize the this profile (always with two parameters). We review a few models which explains the concentration–mass relation by linking halo concentration with halo formation history. We then propose a new toy model, which assumes that the scale radius and scale density of the density profile of a halo are set at the time when the halo collapse, and that the distribution of the halo collapse time can be derived from the time derivative of the halo mass function. With this two simple assumptions, the toy model can provide a reasonable description of the observed concentration–mass relation.

Chapter 4

The Local Velocity Distribution of Dark Matter

This chapter is originally published as

- Y.-Y. Mao, L. E. Strigari, R. H. Wechsler, H.-Y. Wu, O. Hahn, "Halo-to-Halo Similarity and Scatter in the Velocity Distribution of Dark Matter", *Astrophysical Journal*, 764, 35 (2013). © The American Astronomical Society ("AAS")
- Y.-Y. Mao, L. E. Strigari, R. H. Wechsler, "Connecting Direct Dark Matter Detection Experiments to Cosmologically Motivated Halo Models," *Physical Review D*, 89, 063513 (2014). © American Physical Society

Minor modifications have been made to the text. Permission for including this article in this dissertation is granted per the copyright agreements.

Abstract We examine the Velocity Distribution Function (VDF) in dark matter halos from Milky Way to cluster mass scales. We identify an empirical model for the VDF with a wider peak and a steeper tail than a Maxwell–Boltzmann distribution, and discuss physical explanations. We quantify sources of scatter in the VDF of cosmological halos and their implication for direct detection of dark matter. Given modern simulations and observations,

we find that the most significant uncertainty in the VDF of the Milky Way arises from the unknown radial position of the solar system relative to the dark matter halo scale radius. We establish a VDF parameter space from DM-only cosmological simulations and illustrate that seemingly contradictory experimental results can be made consistent within this parameter space. Future experimental limits should be reported after they are marginalized over a range of VDF parameters.

4.1 Introduction

Dark matter is the dominant component of matter in the Universe, and the key to the formation of large-scale and galactic structures. Modern cosmological observations suggest that dark matter is composed of a yet-unidentified elementary particle (e.g., Feng, 2010). However, direct evidence for dark matter particles has proved elusive. Experiments that search for Weakly Interacting Massive Particles (WIMPs), one of the most plausible particle dark matter candidates, seek to identify the scattering of a WIMP with a nucleus in an underground detector (Bernabei et al., 2008; CDMS II Collaboration et al., 2010; Aalseth et al., 2011; Angloher et al., 2012; Aprile et al., 2011). Constraining, and eventually measuring, the WIMP mass and cross section requires a precise understanding of the dark matter spatial and velocity distribution at the Earth's location in the Milky Way (Strigari & Trotta, 2009; McCabe, 2010; Reed et al., 2011; Green, 2012).

Dark matter is distributed in halos extending beyond the visible components of galaxies; many statistical properties including the formation and structure of these halos have been well characterized by simulations. Despite the diversity in the merger and accretion histories of dark matter halos of different masses, cosmological simulations have long suggested near universality in the density profiles of halos (Navarro et al., 1996, 1997). There have been several attempts to connect this universality in the density profile to the dark matter Velocity Distribution Function (VDF) (Hansen et al., 2006; Kuhlen et al., 2010; Navarro et al., 2010). However, there is no well-established model or description for the VDF that has been rigorously tested with cosmological simulations.

Both the implications for direct detection and the quest for a theoretical understanding of the phase-space distribution in dark matter halos motivate a study of the VDF. Under specific, and perhaps too stringent, assumptions, including isolation, equilibrium, spherical symmetry, and isotropy, the VDF may be determined uniquely from the density profile. For example, with all assumptions named above and a known density profile, the ergodic distribution function can be calculated using Eddington's formula (Eddington, 1916). Although useful as an analytic framework, these assumptions are unlikely to strictly hold for halos formed via hierarchical merging.

In absence of an understanding from first principles, a practical approach to study the VDF involves appealing directly to dark matter halos with a wide range of physical properties in cosmological simulations. Quantifying the VDF directly from cosmological simulations would provide a better empirically-motivated framework to predict signals in direct detection experiments. Furthermore, with a parametrized VDF, it becomes more tractable to study the relations between the VDF and other physical quantities of the halos, such as mass, density profile, shape, and formation history.

In this study, we use a suite of dark matter halos from cosmological simulations to study the VDFs at different radii of these halos. We identify a similarity in VDFs among a wide range of halos with different masses, concentrations, and other physical quantities, that depends primarily on r/r_s, the radius at which it is measured divided by the scale radius of the density profile. We further notice that neither standard Maxwell–Boltzmann models (Lewin & Smith, 1996) nor models that have been previously proposed to describe collisionless structures (Hansen et al., 2006; Kuhlen et al., 2010; Navarro et al., 2010) are able to provide an adequate description of cosmological VDFs. Instead, we describe the distribution of the norm of velocity (in the Galactic rest frame) more accurately with an empirical model:

$$f(|\mathbf{v}|) = \begin{cases} A\exp(-|\mathbf{v}|/v_0)\left(v_{\mathrm{esc}}^2 - |\mathbf{v}|^2\right)^p, & 0 \le |\mathbf{v}| \le v_{\mathrm{esc}} \\ 0, & \text{otherwise,} \end{cases} \tag{4.1}$$

where the normalization constant A is chosen such that the integral $4\pi \int_0^{v_{\rm esc}} v^2 f(v) dv$ equals the number of particles in the region of interest. Note that in this parameterization the VDF approaches an exponential distribution instead of a Gaussian distribution at the low-velocity end. With this model, we quantify the scatter in the VDF from a variety of sources, including halo-to-halo scatter, scatter from finite particle sampling, and scatter from the uncertain position of the Earth within a given halo. We further identify the largest uncertainties that currently exist in our understanding of the VDF at the location of the Earth in our Galaxy, and quantify their relevance for inferences from direct detection experiments.

4.2 Universal Velocity Distribution in Simulations

To identify the relevant physical quantities which affect the VDF and to quantify scatter in the distributions among different halos in cosmological simulations, we must examine a large number of halos across a wide range of mass. We also need high resolution to reduce sampling error and distinguish differences in VDFs for different parameters.

In this study, we use halos from the Rhapsody and Bolshoi simulations; state-of-the-art dark-matter-only simulations with high mass resolution. Rhapsody consists of re-simulations of 96 massive cluster-size halos with $M_{\rm vir} = 10^{14.8\pm0.05} M_\odot h^{-1}$. The particle mass is $1.3 \times 10^8 M_\odot h^{-1}$, resulting in $\sim 5 \times 10^6$ particles in each halo. This simulation set currently comprises the largest number of halos simulated with this many particles in a narrow mass bin (Wu et al., 2013b, Figure 1). Bolshoi is a full cosmological simulation, with similar mass resolution, $1.3 \times 10^8 M_\odot h^{-1}$. For detailed descriptions of the Rhapsody and Bolshoi simulations, refer to Wu et al. (2013b) and Klypin et al. (2011) respectively.

We use the phase-space halo finder Rockstar (Behroozi et al., 2013a) to identify host halos at $z = 0$. The masses and radii of the halos are defined by the spherical overdensity of virialization, $M(< r_{\rm vir}) = \frac{4\pi}{3} r_{\rm vir}^3 \Delta_{\rm vir} \rho_c$, where $\Delta_{\rm vir} = 94$ and ρ_c is the critical density. We examine the VDFs at a range of radii. A VDF at radius r uses all particles within a spherical shell centered at the halo center with the inner and outer radii of $10^{\pm0.05} r$, so that the ratio of the shell width to the radius is fixed. In each shell, we assign the escape velocity

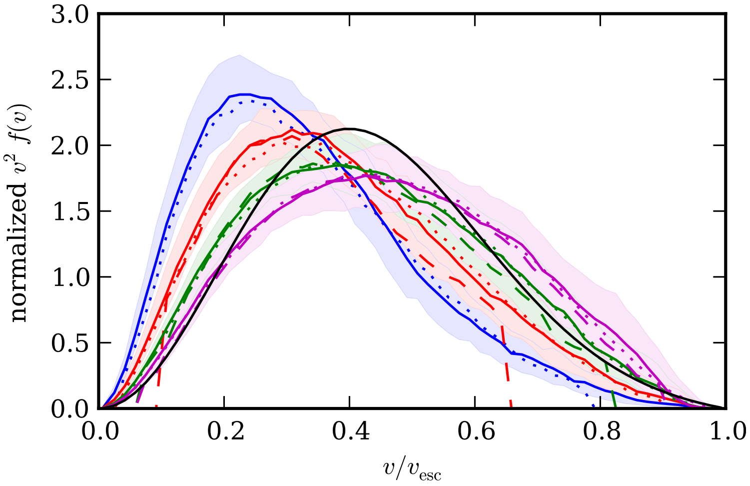

Figure 4.1: Solid colored lines show the stacked velocity distribution for 96 halos in Rhapsody, at different values of r/r_s: (from left to right) 0.15 (blue), 0.3 (red), 0.6 (green), 1.2 (magenta). Bands show the 68% halo-to-halo scatter in those VDFs. Dashed and dotted colored lines indicate the same values of r/r_s in Bolshoi with halos of $M_{\rm vir} \sim 10^{12}$ and $10^{13} M_\odot h^{-1}$ respectively. The VDFs of low-mass halos are cut at the head and tail due to limited particle number, and their scatter is not shown. The SHM ($v_0 = 220$ km/s and $v_{\rm esc} = 544$ km/s) is shown for comparison (black).

($v_{\rm esc}$) as the spherically-averaged $v_{\rm esc}$ of all particles in the shell. We have verified that $v_{\rm esc}$ determined from this method is consistent with the same quantity deduced from the best-fitting spherically-averaged smooth density profile.

We fit each halo with an NFW density profile,

$$\rho(r) = \frac{\rho_s}{(r/r_s)(1+r/r_s)^2}, \tag{4.2}$$

where r_s is the scale radius at which the log–log slope is -2. The fit uses maximum-likelihood estimation based on particles within $r_{\rm vir}$. The halo concentration is defined as $c = r_{\rm vir}/r_s$.

Figure 4.1 shows the VDF at different values of r/r_s. The value of r/r_s affects the shape of VDF dramatically. The peak of the distribution is a strong function of r/r_s. If instead the velocity is normalized by the circular velocity at each radius rather than the escape velocity, this trend will be slightly weakened but still significant. This trend in r/r_s is not surprising because the VDF heavily depends on the gravitational potential. If the density profiles of simulated halos can be described by the NFW profile, which is a function of r/r_s only (up to a normalization constant), the VDF should mostly depend on r/r_s until the isolated NFW potential breaks down at large radius.

The above trend is robust for halo masses down to $\sim 10^{12}$ $\mathrm{M}_{\odot}$, as shown by the Bolshoi simulation in Figure 4.1. The scatter of the VDFs in the low-mass halos considered is somewhat larger due to resolution. However, when the high-mass halos are downsampled to have the same particle number, the spreads in the stacked VDF are comparable to the low-mass halos. We further investigated the impact of a variety of parameters characterizing the halo on the shape of the VDF, and found that for a fixed value of r/r_s, the halo-to-halo scatter in the VDFs is not significantly reduced when binning on concentration, shape, or formation history. A detailed discussion on this halo-to-halo scatter is in Section 4.4.

4.3 Models of the Velocity Distribution Function

The dark matter velocity distribution in halos is set by a sequence of mergers and accretion. The process of violent relaxation (Lynden-Bell, 1967) may be responsible for the resulting near-equilibrium distributions observed in dark matter halos and in galaxies. These near-equilibrium distributions explain why existing VDF models (see e.g., Frandsen et al., 2012), including the Standard Halo Model (SHM), King model, the double power-law model, and the Tsallis model, are all variants of the Maxwell–Boltzmann distribution. Recent studies have shown that the widely-used SHM, which is a Maxwell–Boltzmann distribution with a cut-off put in by hand, is inconsistent with the VDF found in a handful of individual simulations (Stiff & Widrow, 2003; Vogelsberger et al., 2009; Kuhlen et al., 2010; Purcell et al., 2012) and in the study of rotation curve data (Bhattacharjee et al., 2013). The double power-law model was proposed to suppress the tail of the distribution, by raising the SHM to the power of a parameter k (Lisanti et al., 2011). The Tsallis model replaces the Gaussian in Maxwell–Boltzmann distribution with a q-Gaussian, which approaches to a Gaussian as

$q \to 1$ (Vergados et al., 2008). It was argued that the Tsallis model provides better fit to simulations with baryons (Ling et al., 2010), although this conclusion may be affected by the relatively low resolution of the simulations.

In contrast, our empirical model, Equation 4.1, is not based on a Gaussian distribution but rather on an exponential distribution. It also has a power-law cut-off in (binding) energy. Figure 4.2 shows the VDF in a simulated halo, along with the best fit from Equation 4.1 and the best fits from other conventional models. All the best-fit parameters are obtained from the maximum-likelihood estimation in the range of $(0, v_{\rm esc})$. The fits using Equation 4.1 are statistically better than other models or the analytic VDFs, especially around the peak and the tail. We performed the likelihood-ratio test and found that our model fits significantly better for *all* Rhapsody halos than the SHM or the double power-law model at all four radii shown in Figure 4.1.

In Figure 4.2 we also compare three analytic VDFs. For the isotropic model shown, the analytic VDF is given by Eddington's formula, which gives a one-to-one correspondence between the density profile and the VDF. For anisotropic systems, one must also model the anisotropy parameter, defined as $\beta = 1-(\sigma_\theta^2+\sigma_\phi^2)/(2\sigma_r^2)$, where σ^2 is the variance in each velocity component. There is currently no analytic VDF whose anisotropy profile matches that measured in simulations, so we choose three simple and representative anisotropic models: constant anisotropy (with $\beta = 0$ and $1/2$) and the Osipkov–Merritt model (Osipkov, 1979; Merritt, 1985). The phase-space distributions of these models can be determined numerically (Binney & Tremaine, 2008). For all three cases, we adopt the NFW profile as in Equation 4.2, with the best-fit scale radius. For the Osipkov–Merritt model, we use the best-fit anisotropy radius. It is shown in Figure 4.2 and also suggested by the chi-square test for the models considered that the analytic VDFs do not describe the simulated VDF well.

Our VDF model, Equation 4.1, consists of two terms: the exponential term and the cut-off term. The origin of the the exponential term can be explained by the anisotropy in velocity space. Figure 4.3 shows the distributions, the dispersion, and the kurtosis of the velocity vectors along the three axes of the spherical coordinate. Kurtosis is a measure of the peakedness of a distribution, defined as $(\sum_i v_i^4)/(\sum_i v_i^2)^2 - 3$, where v_i is the velocity of

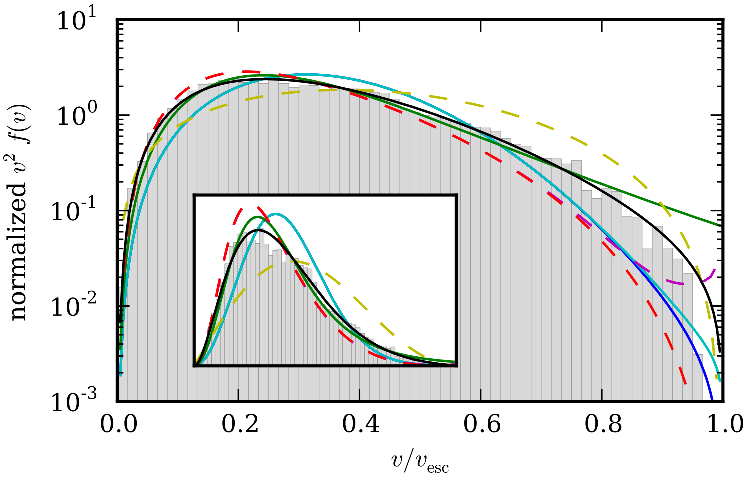

Figure 4.2: The VDF for one representative dark matter halo in Rhapsody (histogram), along with the best fits using Equation 4.1 with $(v_0/v_{\rm esc}, p) = (0.13, 0.78)$ (black, $\chi^2 = 0.59$), SHM (blue, 9.67), the double power-law model (cyan, 9.47), the Tsallis model (green, 1.99), and the analytic VDFs from Eddington's formula with isotropic assumption (red dash, 8.48), Osipkov–Merritt (magenta dash, 6.41), and constant $\beta = 1/2$ (yellow dash, 11.8). The y-axis is in log scale in the main figure and linear in the inset.

the i-th particle along one axis, and this value is zero for the normal distribution. The ratios of dispersion between the three axes are close to one at small radii, and the ratios increase with radius. The kurtosis, on the other hand, is in general non-zero and decreases with radius. An important consequence of the non-zero kurtosis is that even if the dispersion along the three axes are similar (anisotropy parameter $\beta \sim 0$), the velocity vectors do *not* follow an isotropic multivariate normal distribution in any coordinate system (even after a local coordinate transformations). In other words, as long as there exists either anisotropy or non-zero kurtosis in a certain coordinate, the norms of the velocity vectors will not follow the Maxwell–Boltzmann distribution. Indeed, Figure 4.3 shows that in the simulations, one always has non-zero kurtosis and/or anisotropy. Other simulations also indicate that the velocity vectors of dark matter particles have anisotropy (Abel et al., 2012; Sparre & Hansen, 2012) and non-zero kurtosis (Vogelsberger et al., 2009). We further found that if the ratios of dispersion between the three axes of a multivariate normal distribution are around 0.2 to 0.6, the norms of those random vectors will follow a distribution which resembles our model without the cut-off term, $v^2 \exp(-v/v_0)$ (for a formal discussion on this topic, see e.g., Bjornson et al., 2009). This suggests that if one can find a coordinate system where the distributions of the velocity components are all distributed normally (with zero kurtosis), there will be a larger difference between the dispersion along the three axes in this new coordinate system than in the spherical coordinate.

The $(v_{\rm esc}^2 - v^2)^p$ term in our VDF model introduces a cut-off at the escape velocity. It further suppresses the VDF tail more than the exponential term alone does. Despite that this cut-off term has the form of a power-law in (binding) energy, the best-fit values of the parameter p does not necessarily reflect the "asymptotic" power-law index k, defined as $k = \lim_{\mathcal{E}\to 0}(d\ln f/d\ln \mathcal{E})$, where $f(\mathcal{E})$ is the (binding) energy distribution function. The relation between k and the outer density slope has been studied in the literature (Evans & An, 2006; Lisanti et al., 2011). However, because $d\ln f/d\ln \mathcal{E}$ deviates from its asymptotic value k rapidly as $\mathcal{E}$ deviates from zero, the asymptotic power-law index k could be very different from the best-fit power-law index for the VDF tail (e.g. $v > 0.9 v_{\rm esc}$). Furthermore, the shape of the VDF power-law tail could be set by recently-accreted subhalos that have not been fully phase-mixed (Kuhlen et al., 2012), and hence has no simple relation with the density profile. In high-resolution simulated dark matter halos, particles stripped off of a still-surviving subhalo are seen to significantly impact the tail of the VDF. A larger sample of simulations at higher resolution than we consider in the current analysis will be needed to further test this hypothesis.

4.4 Halo-to-halo Scatter in Velocity Distributions

We demonstrated above that there exists a similarity in VDFs for a wide range of simulated dark matter halos; Equation 4.1 provides a good description of this similarity. We now quantify explicitly how the VDF depends on r/r_s and the associated halo-to-halo scatter. Figure 4.4 shows a scatter plot of the velocity distributions for different halos, characterized by the two parameters of Equation 4.1, for different r/r_s. The regions of (v_0, p) parameter space for different r/r_s are distinct, which implies that r/r_s is the most relevant quantity in

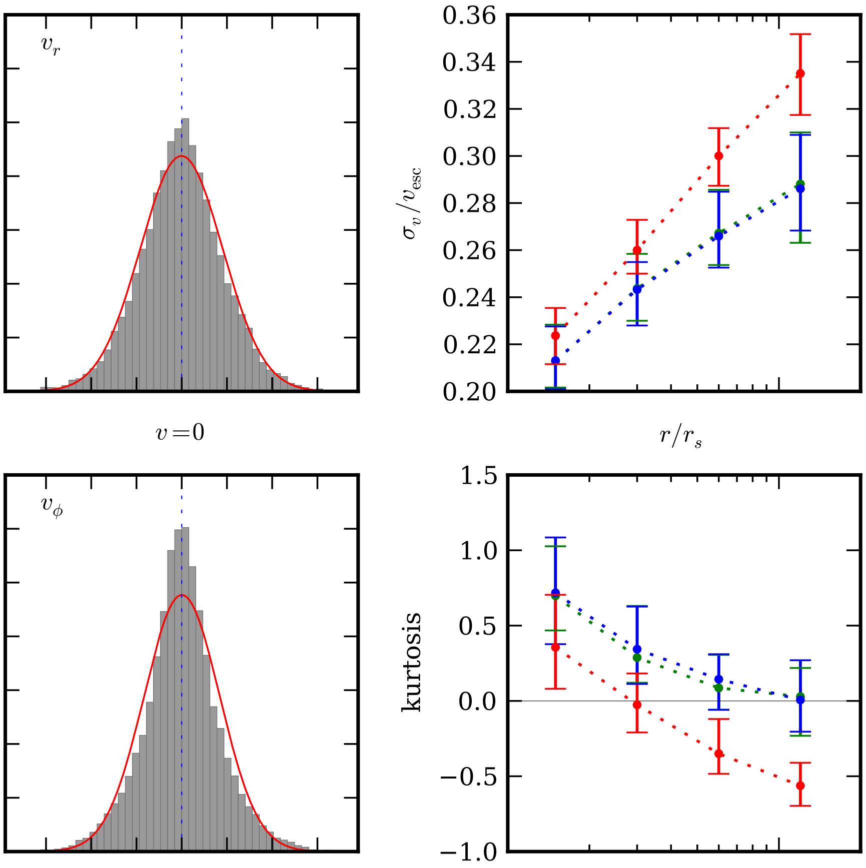

Figure 4.3: *Left*: The histograms of v_r and v_ϕ of the same halo shown in Figure 4.2, with the best-fit normal distributions (red lines). *Right*: The velocity dispersion $\sigma_v/v_{\rm esc}$ and the kurtosis, along the three axes: v_r (red), v_θ (green), and v_ϕ (blue). Both the dispersion and the kurtosis are measured in spherical shells at different r/r_s and averaged over all halos in Rhapsody, with the error bars showing the 68% halo-to-halo scatter. The dashed lines are only to guide the eyes.

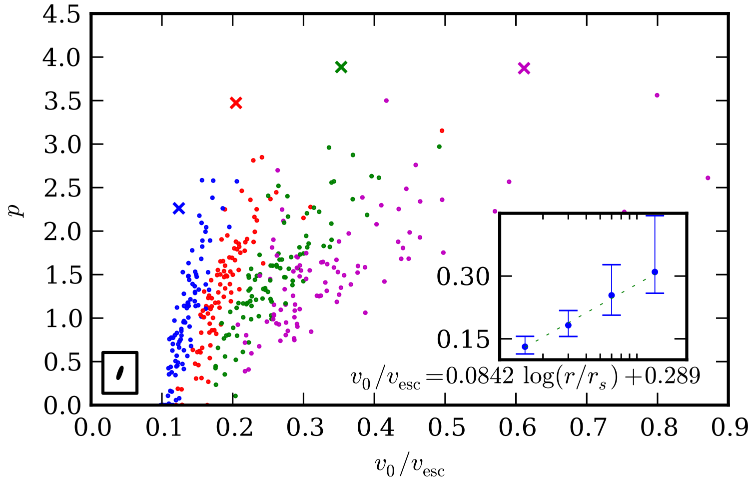

Figure 4.4: Distribution of the best-fit parameters, v_0 and p of Equation 4.1, which describes the simulated VDFs. Each dot represents one halo from the Rhapsody simulation at a certain r/r_s: (from left to right) 0.15 (blue), 0.3 (red), 0.6 (green), 1.2 (magenta). The cross symbols show the best-fit parameters to isotropic analytic VDFs obtained from Eddington's formula at corresponding radii. The typical uncertainty of the fit is shown in the lower left corner. The lower right inset shows the linear relation between $v_0/v_{\rm esc}$ and $\log(r/r_s)$.

determining the shape of the velocity distribution. We also found that the parameter $v_0/v_{\rm esc}$ has a linear relationship in $\log(r/r_s)$, as shown in the inset of Figure 4.4.

We note that there is significant degeneracy between the two parameters (v_0, p). This degeneracy comes from the fact that a larger value of p is needed to steepen the tail of the VDFs which have larger values of v_0. In our fitting process we left both parameters free because there is no simple relation between v_0 and p for all radii. Because of this degeneracy, there also exists a linear relation between p and $\log(r/r_s)$. However, since the best-fit p is not well-constrained due to the low number of particles in the tail of the VDF, the relation between p and $\log(r/r_s)$ is not well determined either.

In Figure 4.4 we see there exists halo-to-halo scatter even for a fixed r/r_s. This intrinsic scatter could arise from the statistics of the samples or some other physical quantities. Figure 4.5 shows the best-fit $v_0/v_{\rm esc}$ at different radii as a function of concentration, halo shape (c/a), formation time ($z_{1/2}$), and local density slope ($-d\ln\rho/d\ln r$) respectively, as defined in Wu et al. (2013b). We found that at a given r/r_s (a fixed color), $v_0/v_{\rm esc}$ does not

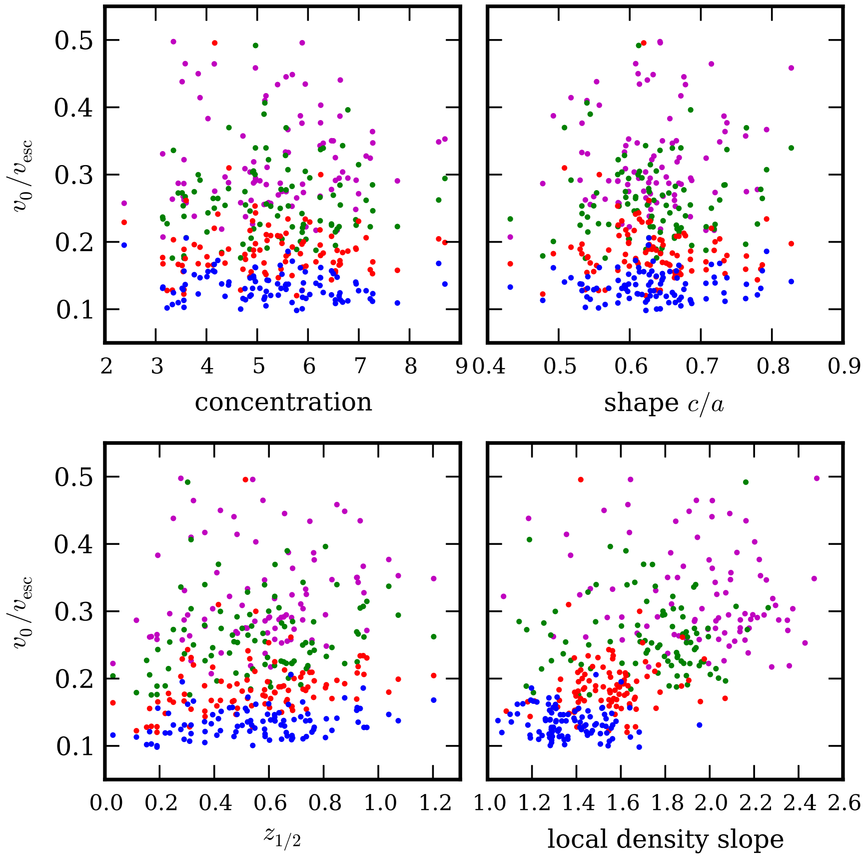

Figure 4.5: Scatter plots of the best-fit parameter $v_0/v_{\rm esc}$ with concentration, halo shape (c/a), formation time ($z_{1/2}$), and local density slope on the x-axes respectively. Each dot represents one halo from the Rhapsody simulation at a certain r/r_s: (from bottom to top in each panel) 0.15 (blue), 0.3 (red), 0.6 (green), 1.2 (magenta). For any fixed r/r_s, there is no significant correlation between $v_0/v_{\rm esc}$ and the aforementioned quantities on the x-axes. See text for details.

have a significant correlation with the physical quantities on the x-axis (except for $z_{1/2}$ in the two smallest radial bins). This reinforces the main result of this study: the VDF is mostly determined by r/r_s (i.e. the gravitational potential). We note that the lower left panel of Figure 4.5 shows a weak correlation between $z_{1/2}$ and $v_0/v_{\rm esc}$; however if the halos with $z_{1/2} < 0.25$ are removed, this correlation is no longer statistically significant. Halos with recent accretion tend to have larger deviations from the NFW profile, and this results in a slight overestimate of the best-fit scale radius (fit to an NFW profile). We do not expect the Milky Way has had a recent major merger with $z_{1/2} < 0.25$. This indicates that for possible Milky Way host halos, one can exclude these systems with recent major mergers, and there will be no remaining correlation between formation time and v_0.

For Milky Way size halos, it has been suggested that the VDF has a universal shape depending only on the velocity dispersion and the local density slope (Hansen et al., 2006). This is related to our finding in a way that the magnitude of the velocity dispersion is roughly proportional to $v_{\rm esc}$ and the local density slope for an NFW profile is given by a monotonic function of r/r_s,

$$\frac{d\ln\rho}{d\ln r} = -\frac{1+3(r/r_s)}{1+(r/r_s)}. \tag{4.3}$$

However, our study suggests that r/r_s is a more fundamental quantity than the local density slope in determining the shape of the VDF. Figure 4.5 illustrates that $v_0/v_{\rm esc}$ does not grow with the local density slope when one only looks at a fixed r/r_s (points with the same color), but it does grow with r/r_s when the local density slope is fixed.

4.5 The Distribution of the VDF Parameters

So far we identify the best-fit VDF parameters $v_0/v_{\rm esc}$ and p of individual halos from simulations, and indicate an apparent correlation between these two parameters for a fixed r/r_s. This degeneracy between $v_0/v_{\rm esc}$ and p impedes a simple description of the parameter domain of interest. To break this degeneracy, we instead find it useful to parameterize the VDF of Equation 4.1 by $v_{\rm rms}/v_{\rm esc}$ and p, where $v_{\rm rms}$ is the root-mean-square velocity,

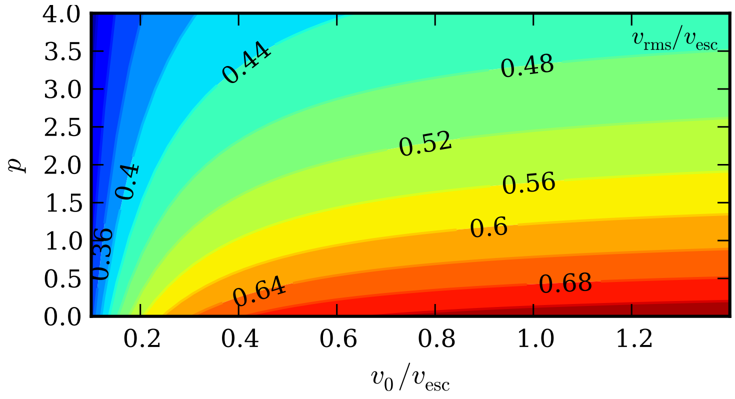

Figure 4.6: Contours show the value of $v_{\rm rms}/v_{\rm esc}$ as a function of $(v_0/v_{\rm esc}, p)$, from the VDF model of Equation 4.1.

defined as $\left[4\pi\int_0^{v_{\rm esc}} dv v^4 f(v)\right]^{1/2}$. For simplicity, hereafter we use $v_{\rm rms}$ and v_0 to refer to their respective normalized values, $v_{\rm rms}/v_{\rm esc}$ and $v_0/v_{\rm esc}$.

In Figure 4.6 we show the value of $v_{\rm rms}$ as a function of (v_0, p). There is an one-to-one correspondence between $(v_{\rm rms}, p)$ and (v_0, p), so the VDF of Equation 4.1 can be completely specified by $(v_{\rm rms}, p)$. Furthermore, lines of constant $v_{\rm rms}$ follow the relation between v_0 and p for a fixed r/r_s, where r_s is the scale radius of the density profile; $v_{\rm rms}$ is largely determined by r/r_s, while the halo-to-halo scatter is primarily determined by the parameter p. This is physically explained by noting that $v_{\rm rms}$ is the ratio of the average energy to the escape energy, which is directly related to the relative position in the gravitational potential.

Figure 4.7 shows the 90% scatter on the VDF parameters for three different samples of simulated halos. One sample is from the Rhapsody simulation (Wu et al., 2013b), in which there are 96 halos with virial mass of $\sim 10^{14.8} M_\odot h^{-1}$. The other two samples are halos with virial mass of $\sim 10^{14} M_\odot h^{-1}$ and of $\sim 10^{13} M_\odot h^{-1}$ respectively, in the the Bolshoi simulation (Klypin et al., 2011). We use samples of halos with different masses in order to determine if there are mass trends of the VDF parameters. As shown in Figure 4.1 and more explicitly in Figure 4.7, there is no mass trend indicated over three orders-of-magnitude in mass, implying that it is reasonable to apply the following analysis to MW-mass halos.

We set the domain of interest on $v_{\rm rms}$ based on the current observational constraint on

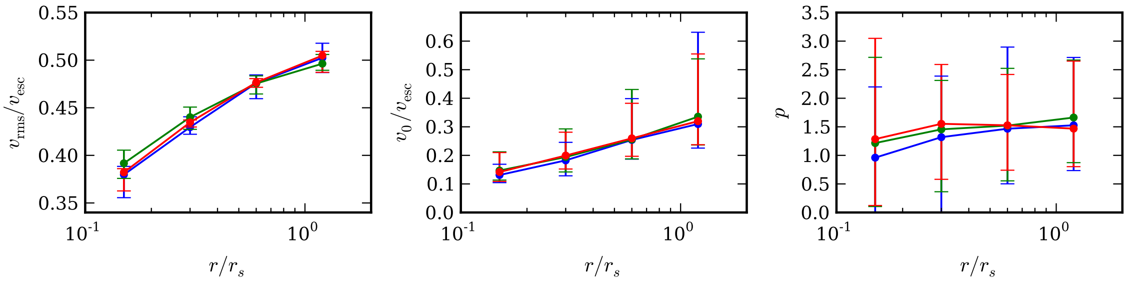

Figure 4.7: From left to right, plots show $v_{\rm rms}/v_{\rm esc}$ (from fitted profiles), fitted v_0, and fitted p respectively, as functions of r/r_s, for simulated DM halos of three samples. The red, green, and blue samples consist of halos of $\sim 10^{13}$,10^{14}, and $10^{14.8} M_\odot h^{-1}$, respectively. See text for the simulation detail. Error bars show the 90% halo-to-halo scatter of each sample.

r/r_s, which is, conservatively, [0.15, 1.2] (we will further discuss this range in Section 4.8; see also e.g., Kafle et al. 2012). This then sets the domain of interest on $v_{\rm rms}$ to be $[0.35, 0.52]$. Since the parameter p is not affected by r/r_s, guided by the 90% halo-to-halo scatter from Figure 4.7 we set the domain of interest on p to be $[0, 3]$. Note that the magnitude of the halo-to-halo scatter is comparable to the directional scatter at a fixed radius within an individual halo, so the above domain will not shrink even if one could remove the halo-to-halo scatter completely, given our lack of knowledge about the Earth's angular position. The simulations used here do not include baryons, so in principle this domain may be larger than what is discussed here.

4.6 Implications for Direct Detection Rates

Weakly Interacting Massive Particles (WIMPs) are well-motivated candidates for dark matter (DM), and many theoretical WIMP candidates have been proposed (Jungman et al., 1996; Bertone et al., 2005; Bertone, 2010; Feng, 2010). Though WIMPs have not been detected, a variety of direct, indirect, and collider experiments are rapidly progressing in searching for them (Strigari, 2013).

Despite rapidly improving sensitivities and analysis methods, direct detection experiments are presenting a conflicting picture. The DAMA (Bernabei et al., 2010), CoGENT (Aalseth et al., 2011), and CRESST (Angloher et al., 2012) collaborations have reported hints for low-mass DM in the mass range $\sim 5-10$ GeV. Most recently, the CDMS-II collaboration has reported three events in their silicon detectors that are not explained by known backgrounds. When interpreted as a WIMP signal this yields a most likely mass of 8.6 GeV (Agnese et al., 2013). However, these candidate events ls are inconsistent with the null result reported by the XENON100 collaboration (Aprile et al., 2012) and the LUX collaboration (Akerib et al., 2014). Ideas to alleviate the conflict include improved characterization of experimental backgrounds (Collar & Fields, 2012; Sorensen, 2012), particle physics explanations such as tuning the ratio of the coupling constants of WIMP scattering on neutrons and protons (Feng et al., 2011), or more detailed examination of the velocity distribution function (VDF) (Lisanti et al., 2011; Bhattacharjee et al., 2013; Frandsen et al., 2012).

The Standard Halo Model (SHM) is commonly adopted by direct detection experiments. As a consequence, uncertainties in the local DM density (see e.g., Bovy & Tremaine, 2012; Garbari et al., 2012) and in the VDF are not a standard component of analysis of experimental data. While the local DM density affects the overall detection rates for all experiments, the VDF affects different experiments differently. For heavy WIMPs, greater than ~ 20 GeV, it is relatively safe to neglect uncertainties in the VDF because the majority of modern experiments are not sensitive to variation of the VDF in this high-mass regime. However, for lighter WIMPs uncertainties the VDF may significantly affect experimental results.

Cosmological simulations have suggested that DM halos in a Lambda Cold Dark Matter (LCDM) universe do not have isothermal profiles (Navarro et al., 1997; Lu et al., 2006), so one does not expect the VDF in DM halos should necessarily follow the isotropic Maxwell–Boltzmann distribution. Recent studies also confirmed this inconsistency by directly comparing the VDFs in simulated halos with the Maxwell–Boltzmann distribution (Vogelsberger et al., 2009; Kuhlen et al., 2010). VDFs which are consistent with certain anisotropy profiles have been calculated (Łokas & Mamon, 2001; Evans & An, 2006), and parametric VDF models that directly fit to the VDF of simulated halos have also been proposed (Lisanti et al., 2011).

In addition to the deviation from the Maxwell–Boltzmann distribution due to anisotropy, large substructures or other dark components such as dark discs (Read et al., 2008; Bruch et al., 2009) and streams Vogelsberger & White (2011) can result in a non-smooth VDF that cannot be characterized by the SHM either. Methods to present and compare results from different experiments without assuming a specific VDF model have been developed (Fox et al., 2011; Frandsen et al., 2012; Gondolo & Gelmini, 2012; Frandsen et al., 2013), though a VDF model is still required to translate results from experiments into constraints or limits on physical parameters of the DM particle (Strigari & Trotta, 2009; Peter, 2010; Pato et al., 2011, 2013; Kavanagh & Green, 2013; Friedland & Shoemaker, 2013).

It has not yet become standard in the direct detection community to include uncertainties of the VDF or to use a VDF-independent presentation in published results, possibly because the traditional vanilla WIMP candidate has mass of $\sim$ 100 GeV and in this regime experiments are less subject to impact of the VDF. As intriguing signals continue to mount, and new theoretical models of low-mass DM are constructed (Feng et al., 2008; Kaplan et al., 2009; Feng et al., 2011; Essig et al., 2012), it is important to systematically address the issue of the VDF in the context of direct detection experiments.

Due to our lack of knowledge about the exact form of the VDF, it is not straightforward to include the possible uncertainties in VDF in experimental analyses. As an initial step, a flexible and parameterized smooth VDF model that is consistent with our understanding of CDM halos is essential at the current stage. With DM-only cosmological simulations, we have empirically determined that the VDF in DM halos may be described by Equation 4.1 with two parameters (v_0, p).

This particular functional form is flexible enough to incorporate a wide range of peak velocities and the power-law fall-off near $v_{\rm esc}$. Although it was motivated by DM-only simulations, a recent study shows that this functional form provides an excellent fit to baryonic simulation as well (Pillepich et al., 2014). While the baryonic physics impacts the best-fit parameters specifying the VDF, it does not appear to change the general functional form. We use a suite of cosmological simulations and zoom-in simulations to identify a domain of the VDF parameter space that is allowed. We further demonstrate that, within this parameter domain, there exists the intriguing possibility that the tension between these experiments can be resolved by uncertainties in the Milky Way (MW) halo model, and motivates the development of a stronger connection between cosmological simulations and predicted direct detection event rates. We conclude by discussing how this VDF model provides a framework for studying the uncertainties in VDF and suggesting how to mitigate these uncertainties in experimental analyses.

Given the known dependence on r/r_s, we can now examine the impact on direct dark matter detection experiments. The differential event rate per unit detector mass of dark matter interactions in direct detection experiments is

$$\left.\frac{dR}{dQ}\right|_Q = \frac{\rho_0 \sigma_0}{2\mu^2 m_{\rm dm}} A^2 \, |F(Q)|^2 \int_{v_{\rm min}(Q)} d^3v \, \frac{f(\mathbf{v}+\mathbf{v_e})}{v}, \tag{4.4}$$

where Q is the recoil energy, ρ_0 is the local dark matter density, σ_0 is the WIMP-nucleus cross section at zero momentum transfer, $m_{\rm dm}$ is the WIMP mass, μ is the WIMP-nucleus reduced mass, A is the atomic number of the nucleus, $|F(Q)|^2$ is the nuclear form factor, $v_{\rm min} = (Q m_N / 2\mu^2)^{1/2}$ for an elastic collision, f is the VDF in the Galactic rest frame, and $\mathbf{v_e}$ is the velocity of Earth in the Galactic rest frame (Lewin & Smith, 1996).

With Equation 4.4 one can calculate the event rate given VDF and $v_{\rm min}$. We calculated this rate for each halo using the best-fit exponential model of the VDF, for different $v_{\rm min}$ and different r/r_s. The results are shown in Figure 4.8, where we divided the rate by the rate calculated from the SHM with conventional parameters $v_0 = 220$ km/s and $v_{\rm esc} = 544$ km/s for comparison.

The rate as a function of $v_{\rm min}$ behaves very differently for different r/r_s as shown in Figure 4.8. For low values of r/r_s, the change in detection rates between experiments can be much larger than the predictions of the SHM, e.g., the ratio between the rates of CoGeNT (Aalseth et al., 2011) to DAMA-I (Bernabei et al., 2008) is three times larger in our model than in the SHM. This clearly motivates efforts to better constrain the scale

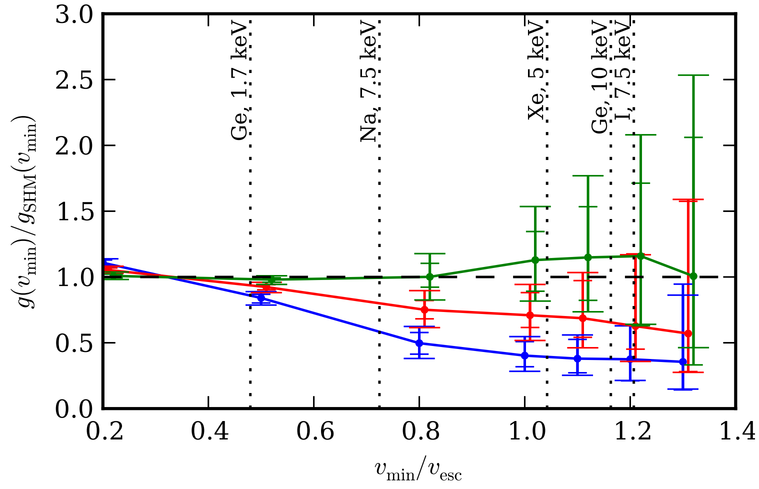

Figure 4.8: Ratio of detection rate predicted by Equation 4.1 with parameters obtained from Rhapsody, for different r/r_s: (from bottom to top) 0.15 (blue), 0.3 (red), 0.6 (green), to that of the SHM with conventional parameters. Vertical dotted lines show v_{min} for different detectors: (from left to right) CoGeNT, DAMA-Na, XENON, CDMS, DAMA-I, expressed in (nucleus, threshold energy) (Aalseth et al., 2011; Bernabei et al., 2008; Aprile et al., 2011; CDMS II Collaboration et al., 2010), assuming a WIMP mass of 10 GeV. The error bars show the 68% halo-to-halo scatter, and those with wider caps include the scatter in different directions. The x-axis is slightly offset for clarity. The lines which connect the data points are only to guide the eyes.

radius of the Milky Way: comparing the scatter coming from measurements of VDF with the intrinsic physical differences among halos, the uncertainty on r/r_s appears to be the dominant contribution to the uncertainty in event rates, especially for smaller $v_{\rm min}$.

4.7 A Demonstration with Mock Experiments

We further demonstrate the impact of uncertainties in the VDF on direct detection experiments by considering two mock experiments, which we call Exp. X and Exp. S, and investigate how the different parameters of the VDF in Equation 4.1 impact the interpretation of the results. In this demonstration, we assume a WIMP model which has a mass $m_{\rm dm} = 8.6$ GeV and a WIMP-nucleon cross section at zero momentum transfer $\sigma_0 = 1.9 \times 10^{-41}$ cm^2, as inspired by the recent results from the CDMS-II experiment (Agnese et al., 2013). Note that this mass and cross section are also consistent with the recent CoGENT analysis (Kelso et al., 2012).

In Exp. X, the target nucleus is xenon, the nuclear recoil energy threshold is 6 keV (i.e. minimal $v_{\rm min} \sim 715$ km/s), and the effective exposure is 6000 kg-days. In Exp. S, the target nucleus is silicon, the threshold is 7 keV (i.e. minimal $v_{\rm min} \sim 443$ km/s), and the exposure is 7.1 kg-day, chosen to obtain a mean event count of 3 in the case of the SHM. In both experiments, to highlight the theoretical impact of the VDF we assume a sharp energy cutoff at the threshold energy, and both perfect energy response efficiency and resolution. We fix the local DM density to be $\rho_0 = 0.3$ GeV/cm^3, and assume equal WIMP coupling to the neutron and proton. We set the Galactic escape velocity to be 544 km/s, and take the averaged speed of the Earth in the Galactic frame to be 232 km/s. Note that we have neglected the uncertainties in ρ_0 (0.3 ± 0.1 GeV/cm^3 (Bovy & Tremaine, 2012)) and $v_{\rm esc}$ (498 – 608 km/s at 90 per cent confidence (Smith et al., 2007)). In a complete analysis these uncertainties should also be marginalized over.

Given the parameters stated above, we can then calculate the predicted event rate R, which is the integral of the differential event rate per unit detector mass over the recoil energy Q,

$$\left.\frac{dR}{dQ}\right|_Q = \frac{\rho_0\sigma_0}{2\mu^2 m_{\mathrm{dm}}} A^2 \left|F(Q)\right|^2 \int_{v_{\mathrm{min}}(Q)} d^3v \, \frac{f(\mathbf{v}+\mathbf{v_e})}{v}. \tag{4.5}$$

Here μ is the WIMP-nucleon reduced mass, A is the atomic number of the nucleus, $|F(Q)|^2$ is the nuclear form factor (Lewin & Smith, 1996), $v_{\mathrm{min}} = (Qm_N/2\mu^2)^{1/2}$ for an elastic collision, f is the VDF in the Galactic rest frame, and $\mathbf{v_e}$ is the velocity of Earth in the Galactic rest frame.

The question we address in this demonstration is how the probability of a certain experiment observing N collision events (assuming all the events are real WIMP-nucleus collisions) varies with different models for the VDF. We define P_X to be the probability that Exp. X observes *no* events, and P_S the probability that Exp. S observes three events. We calculate the probabilities assuming that WIMP-nucleon collision events follow a Poisson process, $P(N;\lambda) = \left(\lambda^N/N!\right) e^{-\lambda}$, where N is the number of events, which equals 0 for P_X and 3 for P_S, and λ is a dimensionless parameter that equals the predicted rate times the exposure of the experiment. Note that λ changes with the WIMP model, the experimental setup, and the VDF. In the demonstration we always fix the WIMP model and the settings of the two experiments, and only change the VDF to see its effect.

Assuming the SHM, we obtain $P_X = 4.65 \times 10^{-7}$ and $P_S = 0.224$. With these assumptions (including the sharp energy cutoff), given the low P_X, Exp. X rejects the WIMP model at a high confidence level. So if Exp. S does indeed observe WIMP events, it implies a strong tension between these two experiments. Note that when the SHM is assumed, this conflict remains for any escape velocity larger than 515 km/s. However, the results change dramatically if a different VDF model is assumed. Assuming the VDF in Equation 4.1 with a range of parameters motivated from cosmological simulations, we calculate P_X and P_S and show the results in Figure 4.9.

The uncertainties in the VDF can have distinct effects on different experiments. Figure 4.9 shows that P_X is a strong function of p, while P_S only mildly depends on v_{rms} and is insensitive to p. Because different experiments have different responses to changes in the VDF, a given VDF can reconcile two experiments that are inconsistent with one another

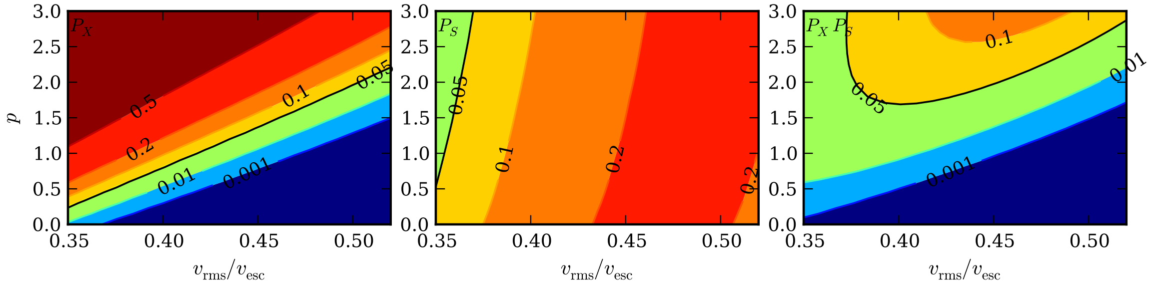

Figure 4.9: Contours show the probabilities P_X (left), P_S (middle), and $P_X \times P_S$ (right), as functions of the VDF parameters $v_{\rm rms}/v_{\rm esc}$ and p in the region of interest. The color scale on each panel is the same. P_X is the probability that Exp. X observes *no* event, and P_S is the probability that Exp. S observes 3 events. Values below 0.05 are excluded with 95% confidence. High values of p can significantly reduce the tension between the two experiments, when compared to the SHM.

when using the SHM.

The left-most panel of Figure 4.9 shows that Exp. X, which is strongly ruled out with the SMH, can only reject less than half of the parameter domain at a 95% confidence level when the VDF is allowed to vary. On the other hand, Exp. S could still observe three events, given that $P_S > 0.05$ for almost all $v_{\rm rms}$ and p within the ranges shown on Figure 4.9. The right-most panel shows the joint probability $P_X \times P_S$. In roughly one-third of the parameter domain, the possibility of Exp. S observing three events and Exp. X observing none cannot be excluded. To exclude this WIMP model for all possible VDFs considered within this domain at 95% confidence level, Exp. X must lower its energy threshold to at least 5.25 keV, if all other conditions and assumptions unchanged.

The above analysis does not include the effect of background noise, the energy cutoff, the energy response efficiency, and the energy resolution of the mock experiments, and hence caution should be invoked when drawing strong conclusions regarding the relation between XENON100 and CDMS-II experiments. Since the original submission of this manuscript, new results were presented by LUX, and for all values in the VDF parameter space we proposed, the results from LUX and CDMS-II experiments appear to be inconsistent. However, it clearly motivates a full self-consistent statistical analysis with a VDF of the form Equation 4.1, because if the DM is in fact a light WIMP, a more realistic model for the VDF will be required to translate measurements into physical parameters of the DM particle.

4.8 Sources of Uncertainties

When deducing the direct detection event rate from cosmological simulations, the primary sources of uncertainty arise from: (i) finite particle sampling of the VDF, (ii) intrinsic scatter from physical processes that affect the VDF during the halo formation process (i.e. the halo-to-halo scatter), (iii) the quality of the fit and the validity of a smooth model, (iv) the observational constraint on r/r_s for the Milky Way, (v) the variation of the VDFs in various directions at a fixed radius, and (vi) the impact of baryons.

An important outcome of our analysis is that at present the scatter from (iv) is significantly larger than the corresponding scatter due to each of (i), (ii), and (iii), combined, by more than two orders of magnitude. This is particularly important given that the observational constraint on the scale radius suggests the concentration $c = r_{\rm vir}/r_s$ is $10-20$ (Klypin et al., 2002; Deason et al., 2012), which corresponds to $r_\odot/r_s \sim 0.15-0.6$ (Xue et al., 2008; Gnedin et al., 2010; Brown et al., 2010; Busha et al., 2011a). Thus, although the distance from the Earth to the Galactic center is well known (Ghez et al., 2008; Gillessen et al., 2009), we find that the largest current theoretical uncertainty on the VDF is the uncertainty in r/r_s.

Our determination of the VDF represents an average over a spherical shell. In reality, spherical asymmetry and substructures will affect the VDF and result in additional scatter along different directions. In the Rhapsody simulations, if we divide the spherical shell into several regions while maintaining enough particles (of the order 1000) in each analysis region, we find that this directional scatter is comparable to the halo-to-halo scatter, and that the combined scatter will be $10-40\%$ larger than only the halo-to-halo scatter, as illustrated in Figure 4.8. Similar scatter is also seen in the Aquarius Milky Way simulations (Vogelsberger et al., 2009). This directional scatter will grow at larger radii because it is a consequence of substructures, tidal effects, and streams (Helmi et al., 2003; Vogelsberger &

White, 2011; Maciejewski et al., 2011; Purcell et al., 2012). At present, we have no robust way to relate this scatter to direct observables, and in practice this directional scatter may be the most important uncertainty in determining the direct detection rates once other sources have been minimized.

We can also distinguish these sources according to their contribution to the uncertainties in v_{rms} or in p. We find here that v_{rms} is largely determined by r/r_s; the uncertainty in this parameter is thus driven by observational uncertainty in r/r_s for the position of the solar system with respect to the density profile of the Milky Way. Conservative estimates of the concentration parameter of the Milky Way imply the region of v_{rms} used in Figure 4.9; with more optimistic assumptions one can constrain $r/r_s \in [0.32, 0.50]$ (Kafle et al., 2012). This will narrow the parameter range shown in Figure 4.9 but would not change our conclusions. It is likely that future data on the motions of Milky Way halo stars and satellites will be able to further constrain the density profile of our Galaxy's halo to minimize this uncertainty.

The uncertainty in p, on the other hand, at present appears to be irreducible. The halo-to-halo scatter in p could originate from the different intrinsic properties between halos, but we have not yet found any significant correlations between p and physical properties of the halo (even if found, the quantity may not be well-constrained observationally). In principle, one could ignore the halo-to-halo scatter if we had a simulation that resembles the Milky Way halo in every way; however, there would still be intra-halo scatter due to variation of VDF in various angular positions at a fixed radius. We found that the intra-halo directional scatter is not smaller than the halo-to-halo scatter. Nevertheless, future measurements of stellar streams and the motions of satellites in the halo of the Milky Way, combined with modeling of large numbers of halos with realistic baryonic physics, could possibly constrain this parameter even in specific regions. Last but not least, baryons could also possibly impact the shape of the VDF as characterized by p.

We have not yet investigated the impact of baryons; we expect that adiabatic contraction of dark matter halos would raise the velocity but preserve the shape of the VDF, so that our model will serve as a useful tool for these studies in the future. Baryonic effects in isolated halos have been studied in the context of dark matter detection (Bruch et al., 2009; Ling et al., 2010). More recently, more high-resolution baryonic simulations have been carried out, and it has been shown that the VDF model we proposed still fit the baryonic simulations very well (Pillepich et al., 2014; Bozorgnia et al., 2016). However, these baryonic simulations seem to suggest a higher value of p (> 2.5), especially when compared with the same halo with only DM. They also show a higher value than the median value we obtained from DM-only simulations. Those this finding is very suggestive, it is still limited to a small sample of halos (~ 10) as simulating a statistical sample of halos with both sufficient resolution and realistic baryonic physics is not yet tractable.

At present it is hence important to include different VDF models or to marginalize over some VDF parameter space, when making statistical statements about signals or exclusions, because different VDF parameters/models that are well within the uncertainties of our current understanding can have very different contribution to the detection rate for different experiments. Figure 4.10 demonstrates this by showing the relative scatter (defined as the difference between the maximum and the minimum divided by the mean value) in $g(v_{\rm min})$ due to the two parameters defined in Equation 4.1 for different values of $v_{\rm min}$, where $g(v_{\rm min})$ is defined as

$$\begin{aligned} g(v_{\rm min}) &\equiv \int_{v_{\rm min}} d^3v\, \frac{f(|\mathbf{v}+\mathbf{v_e}|)}{v} && (4.6)\\ &= \frac{2\pi}{v_e}\int_{\max(v_{\rm min}-v_e,0)}^{v_{\rm esc}} dy\, yL(y)f(y), && (4.7)\end{aligned}$$

where $L(y) = \min(y + v_e - v_{\rm min}, 2y, 2v_e)$ and other variables are defined in the same way as in Equation 4.5. We note that the deduction of Equation 4.7 is valid for any generic, smooth or not, VDF model which only depends on the DM speed in the Galactic frame.

We note that Equation 4.1 does not account for all possible astrophysical uncertainties. Non-smooth components such as dark disks and streams could results in some features in the VDF that cannot be characterized by this model. So far, simulations including hydrodynamics indicate that Equation 4.1 also fits to the VDF very well in the presence of baryons, but since we have not yet fully understood all the baryonic physics involved, it is

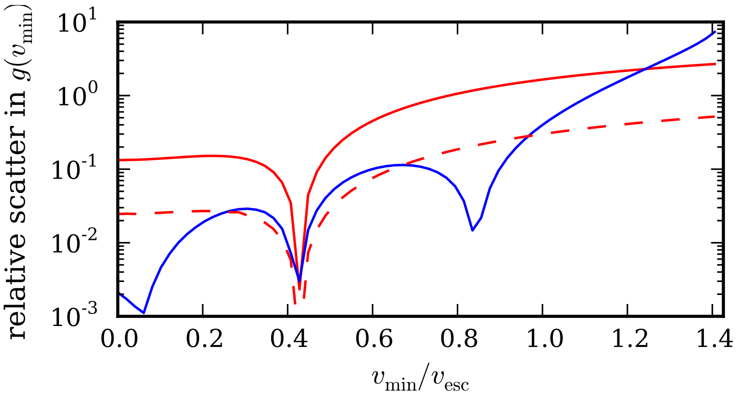

Figure 4.10: Relative scatter in $g(v_{\rm min})$, as defined in text, as a function of $v_{\rm min}$. The red solid line shows the effect of $v_{\rm rms} \in [0.35, 0.52]$ (with $p = 1.5$), the red dashed line shows the effect of a reduced parameter space $v_{\rm rms} \in [0.43, 0.46]$ (with $p = 1.5$), and the blue solid line shows the effect of $p \in [0, 3]$ (with $v_{\rm rms} = 0.45$). The features (dips) are due to the non-zero speed of the Earth in the Galactic frame, and only appear in the scatter of $g(v_{\rm min})$ but not in the energy spectra of the detection experiments.

possible that these processes can contribute to the VDF in a non-trivial way that has not yet been identified. Caution should thus be taken when using Equation 4.1 to represent the full astrophysical uncertainties. Nevertheless, for low-mass WIMPs or for heavy-nucleon detectors (i.e. high $v_{\rm min}$, the dominant contribution to the uncertainty of VDF is the power-law fall-off near $v_{\rm esc}$ (and hence also the value of $v_{\rm esc}$). Equation 4.1 provides a simple yet flexible functional form for this power-law tail, so in the high $v_{\rm min}$ regime, the uncertainty in p will change the results most dramatically.

4.9 Summary

The results presented here highlight the need to significantly improve the determination of the Milky Way scale radius. Although the concentration is now only weakly constrained with present data (Busha et al., 2011a; Deason et al., 2012), improvements will be forthcoming with spectroscopy and astrometry from large scale surveys (An et al., 2012). Analysis along these lines will usher in a new era of complementarity between astronomical surveys and particle dark matter constraints deduced from terrestrial experiments.

In conclusion, we demonstrate that even when restricting to the cosmologically motivated VDFs discussed herein, a wide range of interpretations remain possible for current experimental results. We should emphasize again that assuming the same halo model does not imply that different experiments are comparable, and our demonstration clearly shows this point. Consequently, to present experimental results, especially to make statistical statements about signals or exclusions, we recommend the following strategies:

- In the low-mass regime, use a VDF-independent method (Fox et al., 2011; Frandsen et al., 2012, 2013) for several WIMP masses.
- Show at least two different VDF models to highlight the possible uncertainties. Ideally one should choose two very different ones (e.g. SHM and the VDF function in Equation 4.1 with high p).
- Choose a family of VDF model and marginalize over its parameters (v_0 and p for Equation 4.1) and the relevant astrophysical quantities (ρ_0 and $v_{\rm esc}$). In the case of Equation 4.1, here we provide the priors on its VDF parameters deduced from DM-only cosmological simulations. Future baryonic simulations may change these priors.

Chapter 5

The Abundance of Dark Substructures

This chapter is originally published as

- Y.-Y. Mao, M. Williamson, R. H. Wechsler, "The Dependence of Subhalo Abundance on Halo Concentration", *Astrophysical Journal*, 810, 21 (2015). © The American Astronomical Society ("AAS")

Minor modifications have been made to the text. Permission for including this article in this dissertation is granted per the copyright agreement.

Abstract Hierarchical structure formation implies that the number of subhalos within a dark matter halo depends not only on halo mass, but also on the formation history of the halo. This dependence on the formation history, which is highly correlated with halo concentration, can account for the super-Poissonian scatter in subhalo occupation at a fixed halo mass that has been previously measured in simulations. Here we propose a model to predict the subhalo abundance function for individual host halos, that incorporates both halo mass and concentration. We combine results of cosmological simulations with a new suite of zoom-in simulations of Milky Way-mass halos to calibrate our model. We show the model can successfully reproduce the mean and the scatter of subhalo occupation in these simulations. The implications of this correlation between subhalo abundance and halo concentration are further investigated. We also discuss cases in which inferences about

halo properties can be affected if this correlation between subhalo abundance and halo concentration is ignored; in these cases our model would give a more accurate inference. We propose that with future deep surveys, satellite occupation in the low-mass regime can be used to verify the existence of halo assembly bias.

5.1 Introduction

Bridging our understanding of the processes of galaxy formation and of the evolution of dark matter halos remains one of the primary challenges in modern cosmology. While N-body simulations provide detail about the formation and evolution of dark matter halos, it is still observationally challenging to directly probe their properties. Nevertheless, extensive work over the past decade has used observations of galaxy's spatial distributions to constrain models of the galaxy–halo connection, which reveals how galaxies form in halos (e.g., Berlind & Weinberg, 2002; Zehavi et al., 2011; Reddick et al., 2013). As new observations become more precise, it is crucial to understand possible systematic uncertainty and bias in those models.

The two main characteristics of a dark matter halo are its mass, usually calculated by setting a spherical over-density region, and its formation history. The latter is also highly correlated with the density profile of the halo, and hence with the concentration and with the maximal circular velocity $v_{\max}$ of the halo (Wechsler et al., 2002). Halos of the same mass but different formation history can have very different characteristics or reside in different environments (e.g., Bullock et al., 2001; Allgood et al., 2006; Macciò et al., 2007).

The abundance of subhalos within a dark matter halo most strongly correlates with the mass of the halo (e.g., Kravtsov et al., 2004). Nevertheless, at a fixed halo mass, the subhalo abundance also correlates with the formation history of the halo (Zentner et al., 2005; Zhu et al., 2006; Ishiyama et al., 2009). This correlation, despite its significance in modeling satellite occupation, is often neglected, mostly because it does not manifest itself when the Poisson scatter is comparable to the number of subhalos in consideration. Satellite occupation, or richness, is often used as a proxy of host halo mass, especially for optical observations of clusters (Rozo et al., 2009, 2010). The scatter in the mass distribution inferred from richness can be underestimated if this correlation with concentration is neglected.

In this work, we investigate again the correlation between subhalo abundance and halo concentration, and propose a simple model that describes this correlation. This model can also be used to extend the subhalo abundance function for a given host halo beyond the resolution limit, and enables us to evaluate how this correlation may manifest in a range of observable statistics.

The simplest approach to extend the subhalo abundance function beyond the resolution limit is to extrapolate a parametrized subhalo abundance function. The subhalo abundance function is most commonly modeled by a power law, and the parameters of the model can be calibrated against simulations. Studies have shown this method describes the subhalo abundance functions in N-body simulations very well (Gao et al., 2004; Kravtsov et al., 2004; Giocoli et al., 2008; Springel et al., 2008; Angulo et al., 2009; Boylan-Kolchin et al., 2010; Ishiyama et al., 2013; Cautun et al., 2014b), at least for host halos in a narrow mass range.

In order to calibrate this kind of model over a wide range of mass, usually a suite of cosmological simulations and zoom-in simulations is needed. Zoom-in simulations, such as the Aquarius and Phoenix simulations (Springel et al., 2008; Gao et al., 2012), are particularly powerful for measuring subhalo abundance function at high resolution but still with reasonable costs. However, if one wants to study the halo-to-halo scatter in the subhalo abundance function, a fairly large sample size is required. More recently, two re-simulation suites have been completed with tens to hundreds of simulations in specific small mass ranges: the Rhapsody (cluster-mass halos, Wu et al., 2013a) and ELVIS simulations (Milky Way-mass halos, Garrison-Kimmel et al., 2014).

While these fitting models can usually describe simulations fairly well, they often capture the minimal relevant physics for the particular questions that are being addressed. A more elaborate approach is to consider the assembly histories of dark matter halos and the evolution of halo mass function (Yang et al., 2011). One can further consider more relevant subhalo dynamics when modeling subhalo abundance beyond the resolution limit by tracking the orbits of subhalos and adding subhalos that do not appear or are disrupted in simulations (Zentner et al., 2005; Jiang & van den Bosch, 2014; van den Bosch & Jiang, 2014). Instead of fitting the abundance function, this kind of approach considers most physical details, but at the same time can be more difficult to constrain.

In this work, we focus on an empirical model which directly uses mass and $v_{\rm max}$ of the host halo to predict the subhalo abundance function, and calibrate the model against cosmological and zoom-in simulations. This model is essentially the simplest possible model of subhalo abundance function that takes halo formation history into account. In principle, a more sophisticated model (i.e., models that track subhalo evolution) could produce similar results. However, our simple model provides a straightforward way to evaluate this correlation between subhalo abundance and halo formation history, and to evaluate its implications for various observables.

This chapter is organized as follows. In Section 5.2 we describe the simulations used in this study. In Section 5.3 we first discuss the correlation between subhalo abundance and halo formation history, and then we describe and calibrate the model which predicts the subhalo abundance. In Section 5.4, we further discuss the implications of this correlation between subhalo abundance and halo concentration. We summarize this chapter in Section 5.5.

5.2 Simulations

In this study we use a cosmological simulation `c125-2048` and also present a new set of zoom-in simulations of Milky Way-mass halos.

The `c125-2048` box[1] is a dark matter-only cosmological simulation run with L-GADGET (based on GADGET-2, Springel et al., 2001; Springel, 2005). The box has 2048^3 particles and a side length of 125 Mpc h^{-1}, resulting in a particle mass of $1.8 \times 10^7 M_\odot h^{-1}$. The softening length used is 0.5 kpc h^{-1}, constant in comoving length. The cosmological parameters are $\Omega_m = 0.286$, $\Omega_\Lambda = 0.714$, $h = 0.7$, $\sigma_8 = 0.82$, and $n_s = 0.96$. The initial conditions are

---

[1] Provided by M. R. Becker

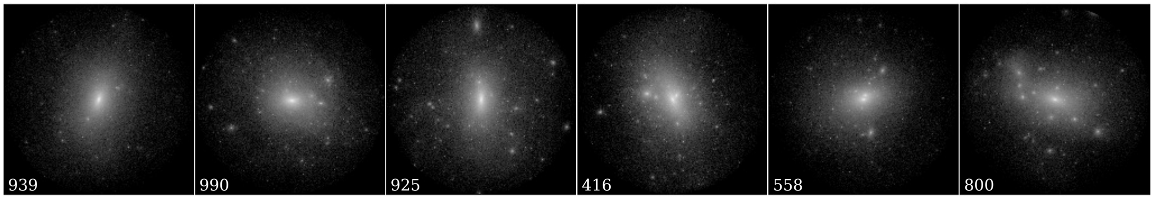

Figure 5.1: Images of the zoom-in simulations of six Milky Way-mass halos, from our suite of 46 halos. The concentration of these selected halos decreases from left to right.

generated by 2LPTic[2] (Crocce et al., 2006) at $z = 199$, with the power spectrum generated by Camb.[3]

The new suite of zoom-in simulations consists of 46 Milky Way-mass halos, selected from the `c125-1024` box (see footnote 1), which is a low-resolution version of the `c125-2048` box. The parameters and initial conditions of these two boxes are identical, but `c125-1024` contains only 1024^3 particles and starts at $z = 99$. All the selected halos fall in the mass range $M_{\rm vir} = 10^{12.1\pm0.03} M_\odot$ in the `c125-1024` box. The initial conditions of these zoom-in simulations are generated with the publicly available Music code[4] (Hahn & Abel, 2011), and are matched to the cosmological box up to the 1024^3 scale. The Lagrangian volume where the highest-resolution particles are placed is set by the rectangular volume which the particles within $10 R_{\rm vir}$ of the present-day halo occupied at $z = 99$. The mass of the highest-resolution particles in the zoom-in simulations is $3.0 \times 10^5 M_\odot h^{-1}$. The softening length in the highest-resolution region is 170 pc h^{-1} comoving. Figure 5.1 shows the images of 6 of these zoom-in simulations. Figure 5.2 compares the concentration distribution of this sample of Milky Way-like halos with the full sample in the mass range in the `c125-2048` box. The concentration distribution of the selected sample is slightly wider than that of all the host halos in the mass range.

In the analysis, we use Rockstar[5] for halo finding and Consistent Trees[6] for tree building (Behroozi et al., 2013a,b). The halos are defined with $\Delta_{\rm vir} \simeq 99.2$ for this

---

[2] http://cosmo.nyu.edu/roman/2LPT/
[3] http://camb.info/
[4] https://bitbucket.org/ohahn/music
[5] https://bitbucket.org/gfcstanford/rockstar
[6] https://bitbucket.org/pbehroozi/consistent-trees

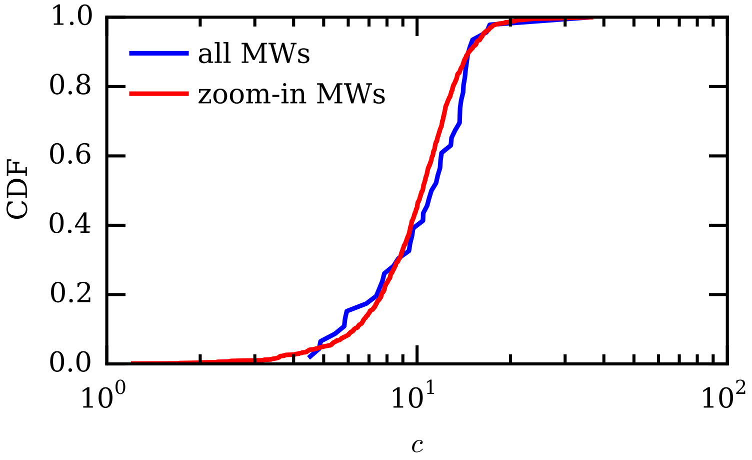

Figure 5.2: The cumulative distribution of concentration (in log scale) for the zoom-in Milky Way halos (red) and all the halos in the same mass range in the`c125-1024` box (blue).

cosmology. Subhalos are defined as halos that are within R_{vir} of any other larger halo. Halos that are not a subhalo are called *host halos* throughout this paper.

The particle mass of a simulation cannot be directly translated into the maximal circular velocity, v_{max}, to which the simulation converges. By inspecting the velocity function, we estimate that a conservative lower limit for the convergence of the `c125-2048` box is $40\,\mathrm{km\,s^{-1}}$, and that of the zoom-in Milky Way simulations is $9\,\mathrm{km\,s^{-1}}$.

5.3 Modeling Subhalo Abundance

In this section, we present a framework to model the subhalo abundance of individual host halos. We first discuss the correlation between subhalo abundance and host halo concentration, and observe qualitatively how host halo concentration affects subhalo abundance function. We further argue that for a given host halo, the number of subhalos is consistent with a Poisson distribution. Then we describe both the framework and the specific parameterization of our model, and calibrate the model against the aforementioned simulations. Finally we briefly discuss the universality of the subhalo abundance function.

5.3.1 Dependence of Subhalo Abundance on Halo Concentration

N-body simulations have shown that the subhalo abundance function averaged over a sample of host halos of a similar mass approximately follows a power law, and its form is nearly universal for different host halo masses when scaled properly (e.g., Gao et al., 2004; Kravtsov et al., 2004; Boylan-Kolchin et al., 2010). Hence, the simplest model of subhalo abundance is to describe the mean number of subhalos, $\langle N_{\rm sub}\rangle$, as a function of host halo mass only. Although this simple kind of model can predict the mean number of subhalos at a given host halo mass in simulations fairly well, it cannot explain the dependence of subhalo abundance on host halo concentration, as shown in Zentner et al. (2005).

To see how host halo concentration affects the number of subhalos, in Figure 5.3 we plot the mean number of halos (including hosts and subhalos) whose $v_{\rm max}$ (or $v_{\rm peak}$) is larger than $60\,{\rm km\,s^{-1}}$ (or $75\,{\rm km\,s^{-1}}$) as a function of host halo mass. We plot this relation for all the host halos and for only halos with the highest and the lowest 25% of concentration in each mass bin. We can clearly see that halos of high concentration tend to have fewer subhalos, and also see that this is not a small effect, especially when the halo halo mass is about $10^{12} M_\odot h^{-1}$. We note that at higher host halo mass, this difference becomes smaller because high-mass halos have a smaller spread in concentrations than low-mass halos.

We now take a closer look at how concentration affects the subhalo abundance on a halo-by-halo basis for host halos of the same mass. In Figure 5.4, we plot the subhalo $v_{\rm max}$ function for all the zoom-in simulated Milky Way-mass halos. The subhalo $v_{\rm max}$ functions in Figure 5.4 are colored according to the concentration of their respective host halos. We observe two prominent features:

1. All these halos fall in a very narrow mass bin (smaller than 0.08 dex), yet there is a significant halo-to-halo scatter in their subhalo $v_{\rm max}$ functions. The halo-to-halo scatter seems to affect mostly the normalization of the subhalo $v_{\rm max}$ function, and the trend roughly follows the concentration trend, which is indicated in colors — darker lines sit lower.

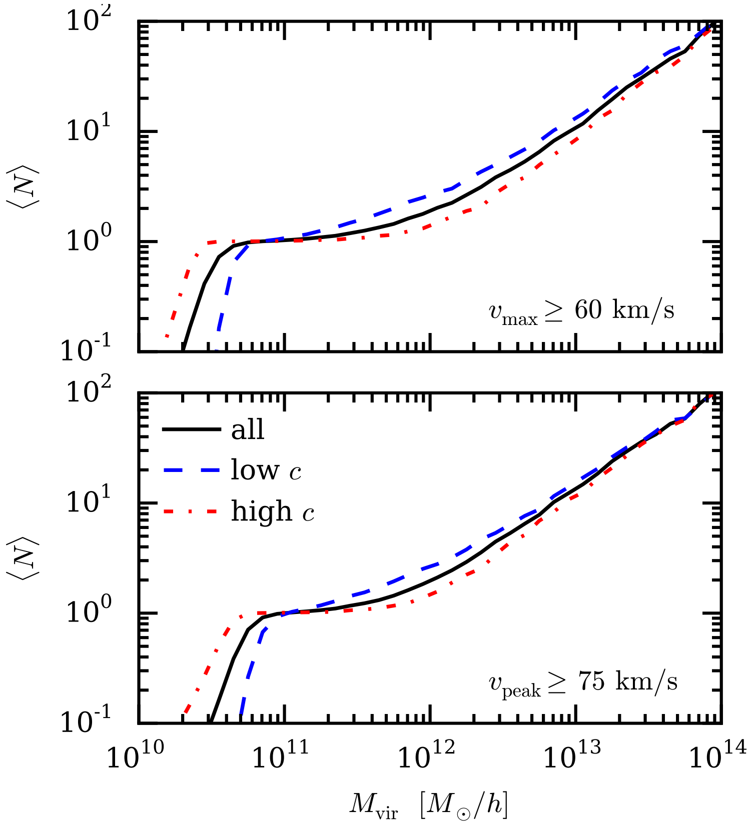

Figure 5.3: Number of *galaxies*, i.e., halos (including both hosts and subhalos) with a cut in $v_{\max}$ (upper) or in $v_{\rm peak}$ (lower), as a function of host halo mass. The black solid line shows all host halos, while the blue dashed line and the red dash–dot line show the host halos with the lowest and the highest 25% of concentration, respectively.

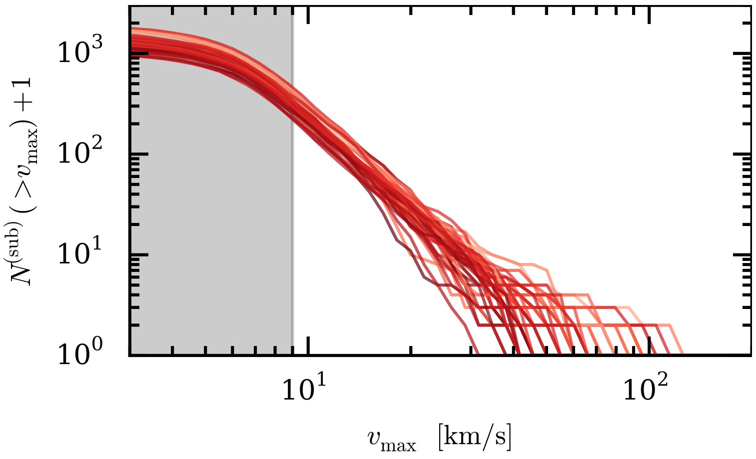

Figure 5.4: The subhalo v_{max} function for the 46 zoom-in simulations of the Milky Way halos. Each line represents one host halo and is colored according to the ratio $V_{\mathrm{max}}/V_{\mathrm{vir}}$ of the host halo. Darker color reprensents halos of higher concentration (larger $V_{\mathrm{max}}/V_{\mathrm{vir}}$). The gray band on the left shows the regime affected by resolution, where the abundance function bends due to unresolved subhalos.

2. On the log–log plot, subhalo v_{max} functions are mostly parallel to one another, especially in the regime where $N_{\mathrm{sub}} > 10$. This suggests the power-law index is roughly a constant from halo to halo. Also, for each individual halo, the deviation of the abundance function from a simple power law is much smaller than the halo-to-halo scatter when N_{sub} is large.

In Wu et al. (2013a), the authors also find that the numbers of subhalos in different v_{max} bins are correlated, especially when N_{sub} is large. This agrees with our findings here.

This correlation between the subhalo number and host halo concentration has been found and discussed in, for example, Zentner et al. (2005), Watson et al. (2011). This correlation can be understood by the hierarchical formation of halos: conditioned on a fixed halo mass, halos with higher concentration form early, and subhalos in these halos are stripped longer to a lower mass and v_{max}, and some could already be completely disrupted and merged with the host. Both effects would result in a smaller number of subhalos at a fixed velocity cut.

5.3.2 Small-scale Poisson Scatter

It is also known and shown explicitly by Boylan-Kolchin et al. (2010) that the scatter in the number of subhalos is super-Poissonian when the mean number is much larger than 1, The authors argue this super-Poissonian scatter is a sum of a Poisson scatter and an *intrinsic* scatter (see also related discussion in Busha et al., 2011b).

Here we further claim that the Poisson scatter should exist on a single-halo basis. That is, given a host halo and its environment, the small-scale variation would result in a Poisson scatter in its subhalo abundance. On the other hand, the *intrinsic* scatter (or more precisely called the *halo-to-halo* scatter) is then in principle all possible scatter among host halos.

To verify that the subhalo abundance function is always subject to this small-scale Poisson scatter when we consider a single host halo, i.e.,

$$(N_{\mathrm{sub}} \,|\, \mathrm{host}) \sim \mathrm{Pois}(\langle N_{\mathrm{sub}} \,|\, \mathrm{host}\rangle), \tag{5.1}$$

we run 13 zoom-in simulations of a single halo, with different random seeds for the small-scale modes. All these 13 realizations have the same simulation setup as described above, and also the same large-scale initial conditions down to the scale of $k \sim 16.4\,h\,\mathrm{Mpc}^{-1}$, which is equivalent to 2048^3 particles in the box. This scale roughly corresponds to a host halo mass of $2.5 \times 10^{10} M_\odot h^{-1}$, or host $V_{\mathrm{max}} \sim 50\,\mathrm{km\,s^{-1}}$.

Figure 5.5 shows $\sigma/\sigma_{\mathrm{Pois}}$, where σ is standard deviation and $\sigma_{\mathrm{Pois}} = \sqrt{\langle N\rangle}$, i.e., the square-rooted ratio of the variance to the mean of the number of subhalos, in bins of v_{max} of the subhalos. The variance and the mean are calculated over the 13 halos of the same large-scale initial conditions. If the number of subhalos in a given v_{max} bin follows a Poisson distribution, this ratio would be 1. In Figure 5.5, one can see that at higher values of v_{max}, this ratio is less than 1, which is expected due to the constrained large-scale modes. At smaller v_{max}, this ratio approaches 1. Although the sample size is small, the typical number of subhalos above $v_{\mathrm{max}} = 10\,\mathrm{km\,s^{-1}}$ is already more than 200. Hence, if the super-Poissonian scatter truly exists at the scales within a single host halo, one would expect the ratio to be larger than 1 at small v_{max}, scaling similar to the green dashed line,

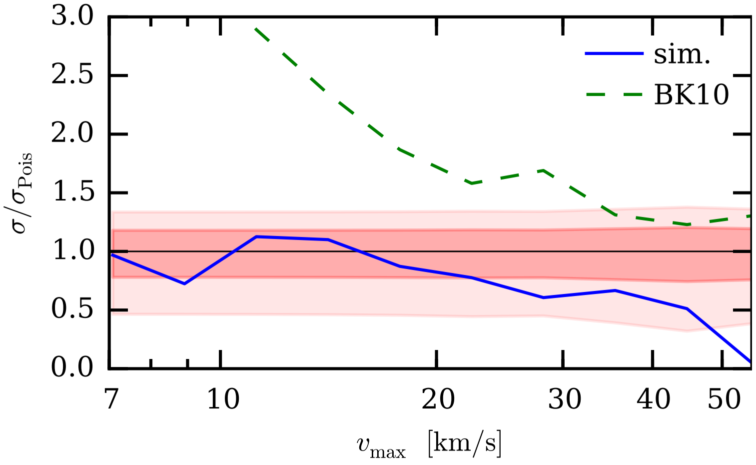

Figure 5.5: The blue line shows $\sigma/\sigma_{\rm Pois}$ in bins of $v_{\rm max}$, calculated over the 13 halos of the same large-scale initial conditions. The red bands show the 1-σ (dark) and 2-σ (light) confidence interval if N follows a Poisson distribution and given that there are 13 samples. The green dashed line shows the super-Poissonion scatter (Boylan-Kolchin et al., 2010, Figure 8) for comparison.

which includes the super-Poissonian scatter. This test suggests that, for a *given* host halo (and its environment), the scatter of its subhalo abundance is consistent with Poisson scatter. The super-Poissonian scatter in a fixed host halo mass cannot solely come from small-scale modes, and should be a result of the scatter in the host halo properties at that fixed mass, combined with dependence of the subhalo abundance on these properties.

5.3.3 Framework of the Model

Now we present the framework of our subhalo abundance model. We first outline our model that describes the number of subhalo for a given host halo, and the parameters of the model. Then we further present how to relate these model parameters to the properties of the host halos. In this fashion, we can clearly separate the Poisson scatter in each individual host halo from the halo-to-halo scatter.

Mathematically, we can model the subhalo abundance function as a counting process. Here the counting process we consider is counting over the proxy variable (i.e., $v_{\rm max}$ or $M_{\rm vir}$), not over the physical time. Although the mathematical term we used is *process*, we are not considering the physical evolution of the subhalo merging process, but only the number of subhalos at a given time.

Let $N(v)$ denote the number of subhalos whose $v_{\rm max}$ (or other proxy, which for simplicity we call v) is greater than or equal to v. Note that $N(v)$ is always an integer and has the following properties:

$$N(v_1) \geq N(v_2), \text{ if } v_1 \leq v_2, \tag{5.2a}$$

$$N(v) = 0, \text{ if } v \geq V_{\rm cut}, \tag{5.2b}$$

where $V_{\rm cut}$ is a scale above which there are no subhalos. The value of $V_{\rm cut}$ depends on the host halo.

We further argue that this counting process is an inhomogeneous Poisson process. That is, the number of subhalos in the interval $[v_1, v_2)$ follows a Poisson distribution and is independent of the counts in any other disjoint intervals. We can write

$$[N(v_1) - N(v_2)] \sim \mathrm{Pois}(\lambda(v_1, v_2)), \tag{5.3}$$

and

$$\lambda(v_1, v_2) = \left(\frac{v_1}{V_0}\right)^n - \left(\frac{\min(v_2, V_{\rm cut})}{V_0}\right)^n, \tag{5.4}$$

where V_0 is a positive parameter and n is a negative parameter, and both could depend on the host halo. Note that the parameters V_0 and $V_{\rm cut}$ should have the unit of the proxy. For example is the proxy is $v_{\rm max}$, they should have the unit of velocity. If one uses $M_{\rm vir}$ instead as the proxy, they should have the unit of mass.

The expected number of subhalos whose $v_{\rm max} \geq v$ is then simply

$$\langle N(v) \rangle = \left(\frac{v}{V_0}\right)^n - \left(\frac{V_{\rm cut}}{V_0}\right)^n. \tag{5.5}$$

We note that by introducing the $V_{\rm cut}$ scale, we do not need an additional exponential cutoff in the model. The average subhalo abundance function naturally drops off at the high end, and resembles a exponential cutoff. There are two strengths of this approach. First, the parameter $V_{\rm cut}$ has a clear physical meaning; no subhalo can have $v_{\rm max}$ (or any proxy in use) that is larger than $V_{\rm cut}$. Second, when implementing this model, one does not need to worry about the chance of having a subhalo with a very large $v_{\rm max}$. The chance of having such an outlier is remote but still finite when using an exponential cutoff, while in our model the probability of a subhalo with $v_{\rm max} \geq V_{\rm cut}$ is zero by construction.

With our framework, there is a straightforward algorithm to create a set of values which represents the set of the subhalo $v_{\rm max}$ values of a particular host halo, given a known threshold $v_{\rm thres}$. This algorithm helps to generate a mock catalog of subhalos beyond the resolution limit. To generate this set, one first draws one random number k from a Poisson distribution of mean $N(v_{\rm thres})$ according to Equation 5.5, with $v_{\rm thres}$ being the minimal possible $v_{\rm max}$ value in the desired set. Then one draws k random numbers $X_1, \ldots, X_k$ from a uniform distribution $\mathcal{U}(0, 1)$. The desired set would then be $\{f(X_1), \ldots, f(X_k)\}$, where

$$f(x) := V_0 \left[N(v_{\rm thres}) \cdot x + \left(\frac{V_{\rm cut}}{V_0} \right)^n \right]^{1/n} \tag{5.6}$$

is the inverse function of Equation 5.5.

5.3.4 Calibrating the Model

So far we have introduced three parameters that are associated with the host halo: $V_{\rm cut}$, the largest scale a subhalo could have; V_0, the overall normalization of the subhalo abundance function; and n, the power-law index (log–log slope) of the subhalo abundance function. In principle, the values of these three parameters in different host halos do not need to follow any universal relation, and can depend on *any* host halo property. Nevertheless, since the dark matter halos in dissipationless simulations do have many universal properties, it is plausible that some universal relations relating these three parameters to the host halo properties would already make a good approximation.

For conventional models that describe $\langle N \rangle$ as a function of host halo mass only, one can parameterize the variables in Equation 5.4 as follows

$$V_0 = a\, V_{\rm vir}, \tag{5.7a}$$

$$V_{\rm cut} = b\, V_{\rm vir}, \tag{5.7b}$$

$$n = n_0, \tag{5.7c}$$

where $V_{\rm vir}$ refer to the circular velocity at $R_{\rm vir}$ of the host halo, a, b, and n_0 are all constants that do *not* depend on any host halo properties.

However, we already know that the parameterization above cannot account for the dependence on halo concentration. Here we present a specific parameterization that replaces a and b in Equation 5.7 with functions of $(V_{\rm max}/V_{\rm vir})$. Particularly, we set

$$a := a_0 \left(\frac{V_{\rm max}}{V_{\rm vir}}\right)^{\alpha}, \tag{5.8a}$$

$$b := b_0 \left(\frac{V_{\rm max}}{V_{\rm vir}}\right)^{\beta}, \tag{5.8b}$$

where a_0, b_0, α, and β are constant. Here $V_{\rm vir}$ and $V_{\rm max}$ refer to the host halo, and their ratio can be viewed as a proxy of the halo concentration or formation time. When $\alpha = \beta = 0$, this falls back to the conventional model which has no concentration dependence.

With this particular parametrization which incorporates host halo concentration, we can calibrate the model against simulations. With the `c125-2048` box, we find the values listed in Table 5.1 provide decent descriptions to both the mean and the scatter of subhalo abundance across a wide range of mass. We also find the values for two different redshifts ($z = 1$ and 3) and for using $v_{\rm peak}$ as the proxy. Note that if one use $v_{\rm peak}$ as the proxy instead of $v_{\rm max}$, the dependence on concentration is slightly weaker (see the values of α in Table 5.1).

Figure 5.6 compares simulations with the prediction from this model with the parameters listed in Table 5.1. In the simulations, we bin host halos according to their mass, in a wide range of masses (10^{12}–$10^{14} M_\odot h^{-1}$), and measure the mean and variance of number of

Proxy	Redshift	a_0	α	b_0	β	n_0
$v_{\rm max}$	0	0.49	−0.9	1.4	−2.5	−2.90
$v_{\rm max}$	1	0.85	−1.0	1.4	−1.0	−2.80
$v_{\rm max}$	3	1.70	−1.0	1.4	−0.8	−2.60
$v_{\rm peak}$	0	0.67	−0.8	1.4	−2.5	−2.75

Table 5.1: Parameter Values. See Equations 5.7 and 5.8 for the definitions of these parameters. See text of Section 5.3.4 for details.

subhalos whose $v_{\rm max} > 50\,{\rm km\,s^{-1}}$ in each bin. For each host halo we also predict the number of subhalos with the model, and measure the binned mean and variance in the same way as with simulations. Then we plot the relative difference between the model prediction and the simulation as a function of host halo mass in Figure 5.6. The relative difference is defined as $\delta X := X_{\rm model}/X_{\rm sim} - 1$, where X could be the mean (upper panels) or variance (lower panels) of number of subhalos in each mass bin.

As Figure 5.6 shows, our model can reproduce the mean and variance of the number of subhalos in all mass bins very well. We also plot the model with *no* concentration dependence ($\alpha = \beta = 0$) for comparison. While this kind of model can reproduce the mean value, it fails to reproduce the variance. Especially for the predicted variance, our model successfully recovers the scatter in high-mass bins, where a model that depends only on mass or the Poisson scatter cannot. For halos of the highest and the lowest 25% concentration in each mass bin, our model also fits the simulation reasonably well.

In this work, we do not focus on refining these relations to obtain the best mock subhalo abundance function. In fact, the essence of this work is to show that with our simple model one can already reproduce most important features in the subhalo abundance function. There are two main reasons for not pursuing the *best-fit* model here.

First of all, the parameterization proposed above is not unique. For example, one can substitute the ratio $V_{\rm max}/V_{\rm vir}$ that appears in V_0 with some generic function of concentration $f(c)$, or put in a mass/velocity dependency in n. The parameters can also involve other host properties, or even be stochastic (i.e., involving random variables). Also, while the parameters provide insight on the dependence on concentration, they do not bear clear

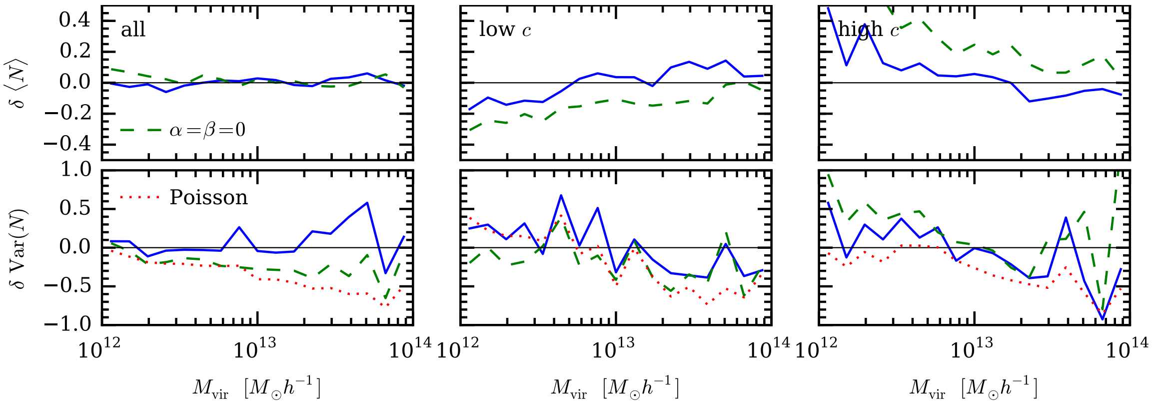

Figure 5.6: Relative difference between the model prediction and simulation of mean (upper row) and of variance (lower row) of the number of subhalos, in bins of host halo mass. The middle and the right columns show the lowest and the highest 25% of concentration, respectively. Blue solid line shows the model we present here. The green dashed line is a model that depends only on host halo mass (i.e., $\alpha = \beta = 0$). The red dotted line shows the Poisson scatter given the mean value in each bin.

physical meaning and the parameterization choice is somewhat arbitrary.

Second, although simulations do provide constraints on the model parameters, these parameters are very degenerate and the Poisson scatter of individual halos makes it very difficult to tightly constrain the *best-fit* parameters. Multiple sets of values could give equally good fits to simulations, and the choice of the objective function (statistics to minimize) would also affect the best-fit values. The reported value in Table 5.1 are obtained by fitting only the mean and scatter of subhalo abundance in the full `c128-2048` box in bins of host halo mass (i.e. to minimize the two leftmost panels in Figure 5.6), yet these values also provide decent fits to the individual abundance function as shown in Figure 5.7.

As a result, here we do not give meaningful error bars on the parameter values, but rather simply demonstrate the model's capability of reproducing the subhalo abundance functions. Until the statistics of high-resolution halos improves significantly, we recommend optimizing the fit every time for each specific use case.

5.3.5 The Power-law Index

So far we have been fixing the power-law index (log–log slope) to be a constant that does not change with halo properties when calibrating our model against the `c125-2048` box. This assumption is consistent with previous studies (e.g., Gao et al., 2012). However, due to the resolution limit, low-mass host halos in a cosmological box do not constrain the index as well as the high-mass halos because the number of resolved subhalos in low-mass host halos is smaller and subject to larger relative Poisson scatter. As a result, the value of n_0 in Table 5.1 is mostly set by those high-mass halos in the box.

To investigate whether the power-law index is indeed a constant, we check if the model would work for both the zoom-in Milky Way halos and the high-mass halos in the box. In Figure 5.7 we compare the subhalo abundance function in simulations with that predicted by the model. We discover that a constant index which can fit the subhalo abundance function very well for cluster-size halos fails to fit the abundance function for zoom-in Milky Way-size halos. The log–log slope of the abundance function is steeper for Milky Way-size halos than for cluster-size halos.

We emphasize again that this mass trend is difficult to detect in a cosmological box due to limited dynamical range. As shown in the upper right panel of Figure 5.7, at $v_{\max} = 50\,\mathrm{km\,s^{-1}}$, both the number of subhalos and the scatter are still consistent with the prediction from a constant slope.

Recall that the power-law index also changes with redshift, as shown in Table 5.1: at higher redshift, the log–log slope of the abundance function is shallower. The relation between the power-law index, host halo mass, and redshift is also discussed in Zentner et al. (2005), Watson et al. (2011). An intriguing question is then whether this redshift trend and the aforementioned mass trend in the index have the same physical origin.

Specifically, we find that we can fit the subhalo $v_{\max}$ functions of the zoom-in Milky Way halos and of the cosmological box simultaneously (see the lower panels of Figure 5.7) if we replace the constant index by this relation,

$$n = -3.05\, \nu(M, z)^{-0.1}, \tag{5.9}$$

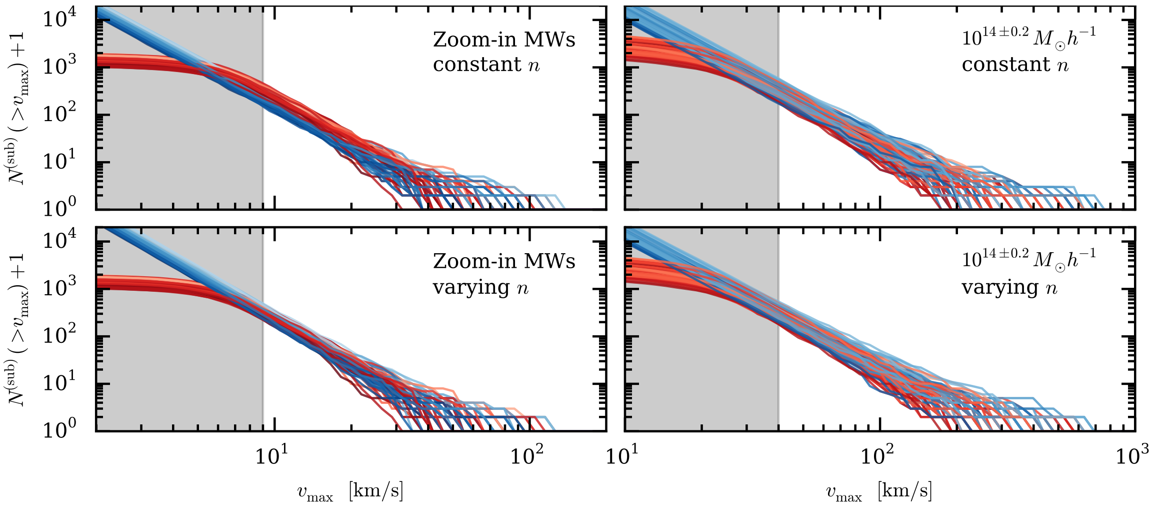

Figure 5.7: Subhalo abundance function in simulations (red) and predicted by the model (blue). The shade of colors represents the concentration ($V_{\mathrm{max}}/V_{\mathrm{vir}}$) of the halo: the darker the more concentrated. The two columns show two different host halo masses. The upper row uses the model with constant index ($n = n_0$), while the lower row uses Equation 5.9. The model with constant index cannot reproduce the subhalo abundance function for zoom-in Milky Way halos (upper left panel). The gray band on the left shows the regime affected by resolution.

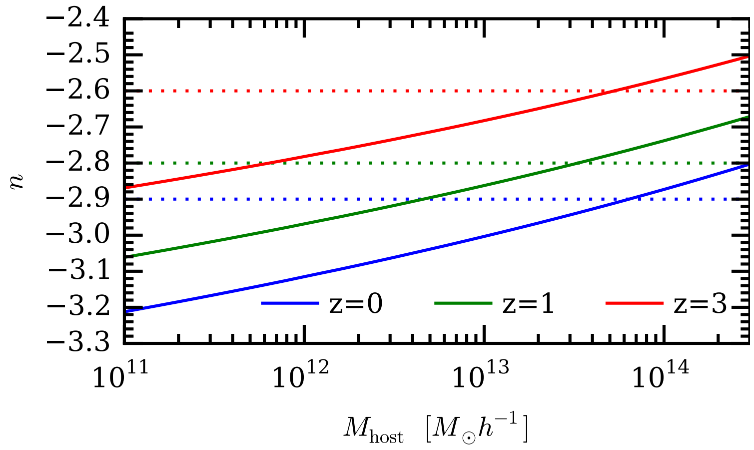

Figure 5.8: The solid lines show Equation 5.9: the log–log slope as a function of mass at three different redshifts: $z = 0$ (blue), 1 (green), and 3 (red). The dotted horizontal lines show the values of n_0 in Table 5.1 of corresponding redshifts.

where

$$\nu(M, z) = \frac{\delta_c}{\sigma(M) D(z)},$$

$\delta_c \approx 1.686$ is the critical overdensity, $D(z)$ is the linear growth rate, and $\sigma(M)$ is the squared root of the mass variance (at $z = 0$) with a top-hat filter of mass M.

Figure 5.8 shows the relation of Equation 5.9 and compares it with the constant values of n_0 in Table 5.1. Although this is *not* a proof of the validity of Equation 5.9, it indeed demonstrates the possibility that the mass and redshift trends in the power-law index have the same physical origin. To robustly verify this connection between n and $\nu(M, z)$ would require several sets of zoom-in simulations of halos of different masses, preferably also with different cosmologies. This is beyond the scope of this work, but worth exploring as simulation suites expand.

5.4 Implications and Discussion

So far we have been focusing on *subhalo* abundance function and its dependence on host halo concentration. In this section, we discuss its observational implications. While we cannot observe dark matter subhalos directly, we can certainly count the satellite galaxies that sit in those subhalos. Hence, the *subhalo* occupation can be viewed as a proxy of the *satellite* occupation, subject to the effect of baryons on the subhalo abundance function (e.g., Cui et al., 2012; Vogelsberger et al., 2014). Here we ignore baryonic effects and directly translate the subhalo occupation above a certain velocity cut to the satellite abundance at a luminosity threshold by specifying a galaxy–subhalo connection.

The simplest relation between subhalos and satellite galaxies is a one-to-one relation,

$$N_{\mathrm{sub}}(>v) = N_{\mathrm{sat}}(>L(v)), \tag{5.10}$$

where $L(v)$ specifies the correspondence between velocity cut and luminosity threshold by matching their abundance functions. This is commonly known as *abundance matching* (e.g., Kravtsov et al., 2004; Vale & Ostriker, 2004), which has been shown to work fairly well for predicting measurements such as the correlation functions (e.g., Conroy et al., 2006; Reddick et al., 2013). With this abundance matching scheme, the model we introduced in Section 5.3 directly becomes $P(N_{\mathrm{sat}}|M, c)$, and it implies that satellite occupation depends on both host halo mass and concentration.

A different, but also widely used approach is to use Halo Occupation Distribution (HOD). Instead of specifying the galaxy–subhalo connection, standard HOD directly models the probability distribution of satellite occupation at a luminosity threshold as a function of host halo mass (e.g., Peacock & Smith, 2000; Seljak, 2000; Scoccimarro et al., 2001; Berlind & Weinberg, 2002; Cooray & Sheth, 2002). That is, it specifies $P(N_{\mathrm{sat}} > L|M)$, and this distribution of satellite occupation does not depend on host halo concentration. Nevertheless, one can also generalize the HOD to include the concentration dependence and to specify $P(N_{\mathrm{sat}}|M, c)$. Yet most studies constraining HOD assume the sole dependence on mass.

Abundance matching and HOD also differ from each other in how the positions of the satellite galaxies are assigned. However, in the context of satellite occupation, the only relevant difference is whether or not the satellite occupation depends on host halo concentration (at a given host halo mass). It is clear that *subhalo* occupation does depend on host halo concentration, but the stochastic process of galaxy formation could diminish this dependence. Nevertheless, it is also possible that Equation 5.10 is only perturbed, and the concentration dependence of *subhalo* abundance still survives and results in the concentration dependence of *satellite* abundance.

In this section, we assume the simple relation of Equation 5.10, and investigate the implications of the correlation between concentration and satellite occupation. We compare the different inferences between these two models (with and without concentration dependence) when using satellite occupation as a proxy of halo mass. Then we look at the the possible signal of halo assembly bias with satellite occupation.

5.4.1 Satellite Occupation as a Proxy of Halo Mass

Satellite occupation, especially in the cluster-mass regime, has been used to probe the host halo mass (Old et al., 2014, 2015; Oguri & Lin, 2015; Rozo et al., 2015). Conventionally, this is done within the standard HOD framework, which ignores the dependence of satellite occupation on host halo concentration. Here we would like to investigate the effects of ignoring this dependence. We consider the two subhalo models, as presented in Figure 5.6: one only depends on halo mass like the standard HOD, and the other incorporates the dependence on concentration as introduced in Section 5.3. We then take the host halos from simulations and populate them with subhalos according to these two models. This procedure is repeated multiple times to obtain enough statistics and to smooth the Poisson noise.

Figure 5.9 shows the joint distribution of the host halo mass and concentration at a fixed satellite occupation, $N_{\rm sat}(v_{\rm max} > 75~{\rm km/s}) = 100$, in the context of cluster-size halos. We see significant differences between the inferences from the two subhalo models, with or without the dependence on concentration. Although the mean value of inferred mass does not differ more than 1 σ, the inferred distribution of mass is much wider in the case with the dependence on concentration, and also includes many more high-concentration high-mass

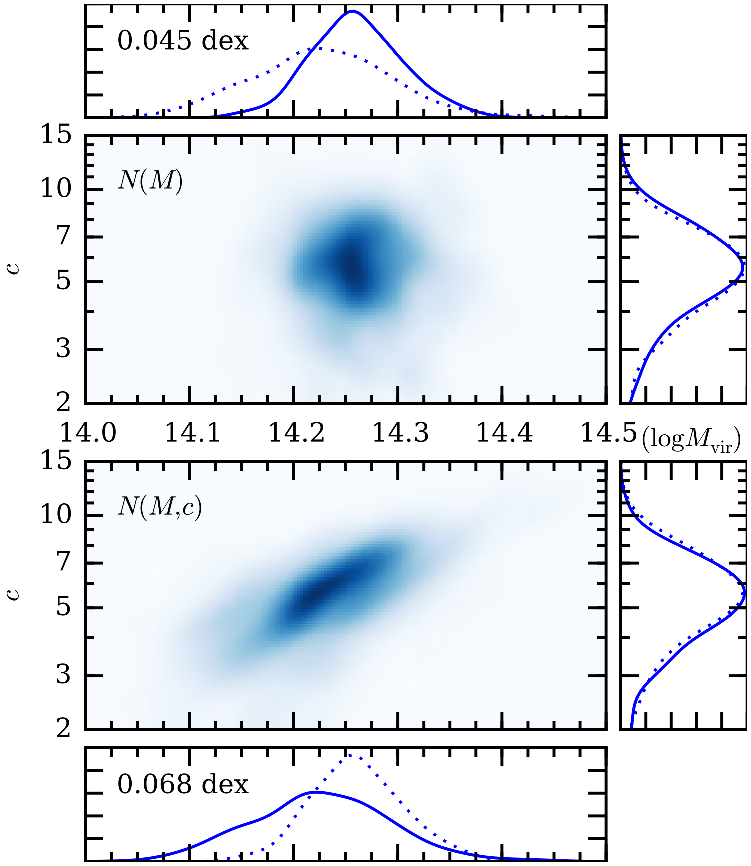

Figure 5.9: The joint and marginal distributions of logarithmic concentration (y-axis) and logarithmic mass (x-axis) of all the host halos which have exactly 100 subhalos whose $v_{\max} > 75\,\mathrm{km\,s^{-1}}$. The upper and lower parts demonstrate the inference from the two models: (1) with only mass dependence (upper) and (2) with both mass and concentration dependence (lower). Dotted lines in the side panels show the same marginal distribution for the other model just for convenient comparison by eyes. Both models are the same as used in Figure 5.6. The number in the marginal distribution of logarithmic mass shows σ value.

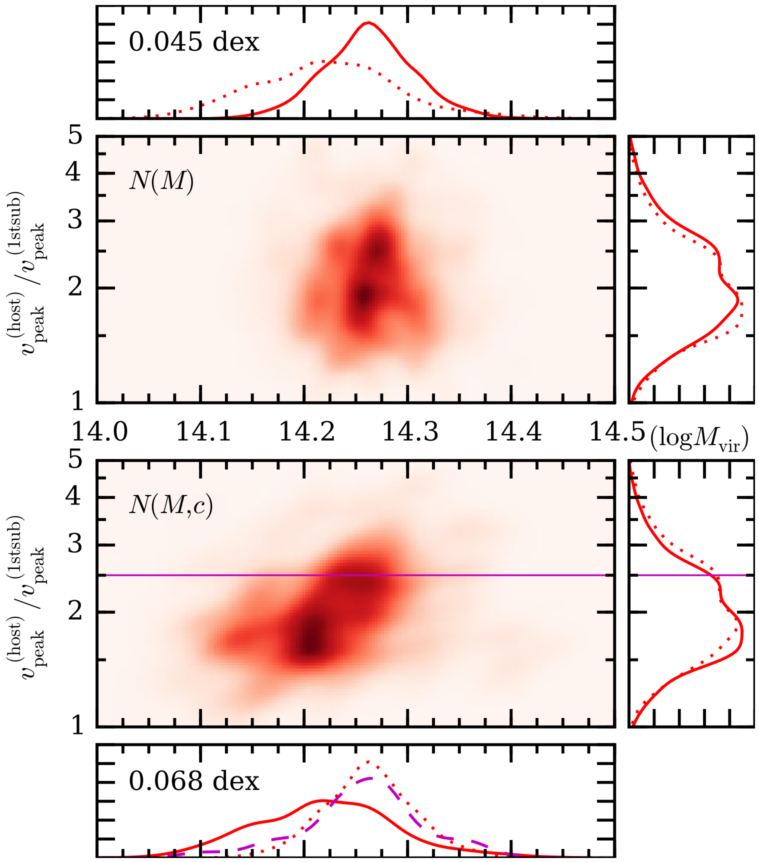

Figure 5.10: Same as Figure 5.9, but showing the distributions of log $v_{\rm peak}^{\rm host}/v_{\rm peak}^{\rm 1st\,sub}$ (y-axis) and logarithmic mass (x-axis). The magenta dashed line in the lowest panel shows the mass distribution when selecting only halos whose "gap" is larger than 2.5.

or low-concentration low-mass halos.

The difference seen in Figure 5.9 would be especially prominent when the number of subhalos in consideration is large compared to the Poisson noise, i.e., $N_{\rm sat} \gg \sqrt{N_{\rm sat}}$. Thus when estimating the mass of galaxy clusters with richness or satellite occupation, one should consider including halo concentration in the model, especially in cases when not only the mean estimator but also the resulting inference is relevant.

To refine the mass estimator for halos of a fixed occupation, we then need some independent observable to probe halo concentration. We discuss three possible choices here.

1. *The radial distribution of satellites.* If satellites trace the density profile of the

host halo, then by the radial distribution of satellites could provide independent information on host halo concentration. By comparing the number of satellites in different projected radial bins, one may be able to select those more concentrated halos in a fixed-richness sample.

2. *The luminosity of the central galaxy.* For example, the abundance matching scheme of Equation 5.10 matches luminosity with $v_{\rm max}$ or $v_{\rm peak}$ instead of $M_{\rm vir}$, and results in the dependence of luminosity on concentration. Hence a further selection on the luminosity of central galaxy may provide a tighter mass distribution (see also Reyes et al., 2008). R. M. Reddick et al. (2016, in preparation) also finds a negative correlation between the central luminosity and richness at a fixed halo mass, which agrees with trends proposed here.

3. *The magnitude gap*. In addition to the concentration dependence of luminosity, the magnitude gap between the central galaxy and the brightest satellite galaxy can further depend on the host halo concentration. For instance, as suggested by our model, the parameter $V_{\rm cut}$ itself has a concentration dependence, regardless how luminosity is matched to halo properties. It has also been shown in simulations that the gap is correlated with the formation history of the host halo, and hence with concentration (D'Onghia et al., 2005; Zentner et al., 2005; Dariush et al., 2010; Deason et al., 2013; Wu et al., 2013a).

It has been suggested that selecting on magnitude gap can refine the mass distribution of a fixed-richness sample (More, 2012; Hearin et al., 2013b; Lu et al., 2015). Here we revisit this method by considering the correlation between occupation (richness) and halo concentration. Figure 5.10 shows the distributions of magnitude gap and halo mass, for a sample of a fixed occupation (100 subhalos whose $v_{\rm max} > 75\,{\rm km\,s^{-1}}$, same as in Figure 5.9), for the two subhalo models. Here the magnitude gap is approximated by $\log v_{\rm peak}^{\rm host}/v_{\rm peak}^{\rm 1st\ sub}$, and can be translated into the actual magnitude map by abundance matching. As we already learned, the distribution of halo mass is much wider (lower panel) than that from the assumption that satellite occupation depends on host halo mass only (upper panel).

Nevertheless, if we apply a further selection on the magnitude gap, selecting only halos with larger gaps, we can obtain a sample of halos whose mass distribution is much closer to that in the upper panel.

This may provide a viable method to obtain a sample of halos in a narrower halo mass bin, especially in the high-mass regime. It has been shown that selecting on magnitude gap can indeed narrow the velocity dispersion distribution of the sample (Hearin et al., 2013b). As for halo mass, it remains to be seen how strong these effects are in specific observed samples, but we expect that the relative impact of the central galaxy luminosity and the magnitude gap could be tested in the near future using either lensing or X-ray measurements of large samples of optically selected clusters with fixed galaxy number.

5.4.2 Satellites of the Milky Way

In the context of Milky Way-mass halos, the number of subhalos in consideration is much smaller, and the Poisson noise of individual halos would dominate and diminish the difference between these two subhalo models. Nevertheless, in Figure 5.9 we observe a positive correlation between the host halo mass and concentration for this sample of a fixed satellite occupation. This positive correlation differs from the commonly known concentration–mass relation (e.g., Navarro et al., 1997), and can also been seen when the number of subhalos in consideration is small.

Figure 5.11 shows the joint distribution of the host halo mass and concentration at another fixed satellite occupation, $N_{\mathrm{sat}}(v_{\mathrm{max}} > 30\ \mathrm{km/s}) = 4$. In this case, the marginal distributions of mass or of concentration barely differ between the two subhalo models. Nevertheless, the predicted correlation between mass and concentration is fairly different in the two cases. Without the dependence on concentration, a sample of a fixed satellite occupation basically corresponds to a sample of halos in a mass bin, and the correlation between halo concentration and mass inherits the usual, negative, concentration–mass relation of host halos. On the other hand, with the dependence on concentration, the inferred correlation between concentration and mass becomes positive.

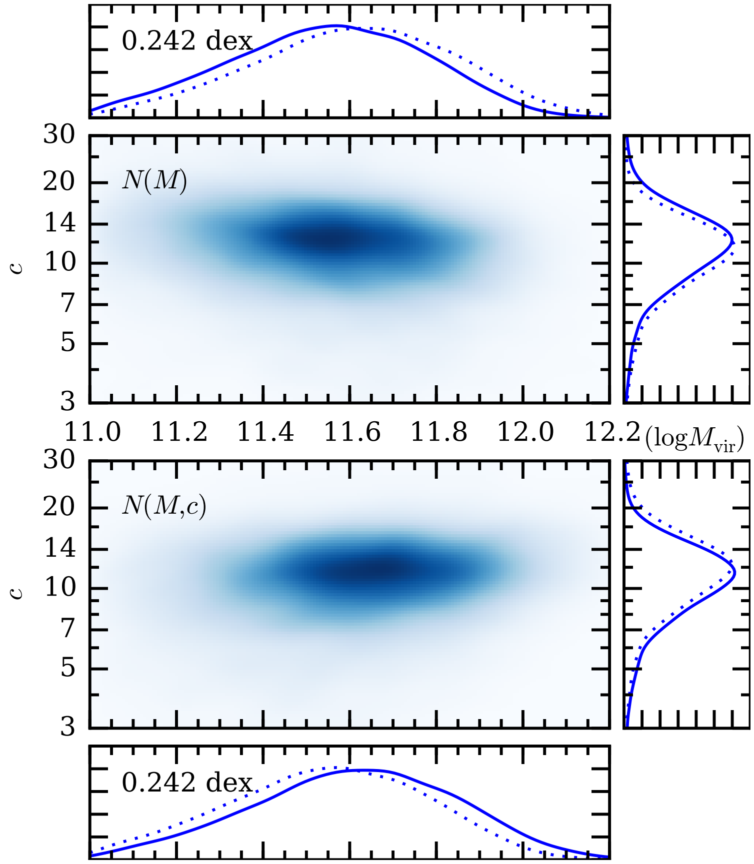

Figure 5.11: Same as Figure 5.9, but showing of all the host halos which have exactly four subhalos whose $v_{\rm max} > 30\,{\rm km\,s^{-1}}$.

This discrepancy again highlights the need to consider this dependence of satellite occupation on concentration when inferring the mass or other properties of the Milky Way halo from satellites (e.g., Busha et al., 2011a; Rodríguez-Puebla et al., 2013b,a; Cautun et al., 2014a). If the inference is not derived completely from simulations but with the help of a subhalo model which does not account for dependence on concentration, such as the conventional HOD, then one might need to consider the effect discussed above when interpreting the results, particularly the degenerate correlation between concentration and mass. We also note that recent constraint on the mass and concentration of the Milky Way from dynamical tracers have a negatively correlated degeneracy (Wang et al., 2015), while occupation-based constraints will have the opposite degeneracy if the concentration dependence is properly accounted for, as demonstrated here.

This dependence on concentration also suggests that one should take the concentration of the Milky Way halo into account when investigating the tension between the population of subhalos in N-body simulations and that of the observed Milky Way satellite galaxies (e.g., Kauffmann et al., 1993; Klypin et al., 1999b; Moore et al., 1999; Bullock, 2010; Boylan-Kolchin et al., 2011; Purcell & Zentner, 2012). While a Milky Way-like halo is conventionally defined by selecting on halo mass only, it is clear that the concentration of the Milky Way halo could potentially change the statistical significance of the aforementioned tension. In a follow-up paper, we further investigate these implications of this dependence on concentration for the Milky Way and its population of satellites (Y.-Y. Mao et al. 2016, in preparation).

5.4.3 Observing Halo Assembly Bias

Given that satellite occupation is a direct observable that is correlated with halo concentration, it may provide a way to observationally detect the halo assembly bias. Halo assembly bias has been shown to exist in simulations; particularly it is found that host halos of different formation histories or concentrations cluster differently,

$$b_{\mathrm{h}}(M, c) \neq b_{\mathrm{h}}(M), \tag{5.11}$$

where b_{h} is the halo bias function (Gao et al., 2005a; Wechsler et al., 2006; Gao & White, 2007). The question we want to address here is whether we can measure

$$b_{\mathrm{h}}(M, N_{\mathrm{sat}}) \neq b_{\mathrm{h}}(M), \tag{5.12}$$

and if so, whether it implies the existence of halo assembly bias as in Equation 5.11.

Instead of calculating the bias function directly, we use the mark correlation function (MCF) to probe the bias. The MCF is defined as

$$\mathrm{MCF}(m, r) = \sum_{(i,j)\in S_r} \frac{m_i m_j}{\bar{m}^2}, \tag{5.13}$$

where $S_r = \{(i, j) : \left|\mathbf{x}_i - \mathbf{x}_j\right| \in [r, r + dr]\}$, and $\bar{m}$ is the mean of m_i over i. The MCF of a specific mark m shows whether the averaged value of this mark for halos in pairs is higher or lower than the averaged value of the whole sample. For each radial bin S_r, we find all pairs of halos whose separation falls in that bin and measure the mark of those halos. To accommodate the possible large range of the mark values, we use the ranks of the mark instead of the actual value for m, normalized by the total number of different values. If Equation 5.12 holds, we expect either a positive or a negative excess in the MCF of N_{sat}.

In Wechsler et al. (2006), the authors found a positive excess in the MCF of N_{sat} in the regime above M_*, but were not able to find a similar signal below M_*. To interpret these results, recall that for halos below the typical collapse mass M_*, high-concentrated halos are more clustered; for halos above M_*, high-concentrated halos are less clustered. In the regime above M_*, halos in pairs are on averaged more massive but *less* concentrated, and both characters give a higher N_{sat}. As a result, the excess in the MCF of N_{sat} comes from a mixed effect of both mass and concentration, and hence it is easy to detect this excess but

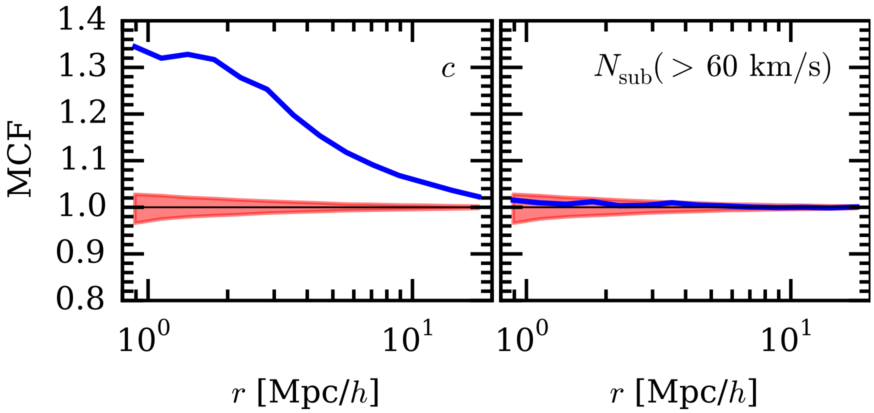

Figure 5.12: The MCFs of concentration (left) and of satellite occupation ($v_{\rm max} > 60\,{\rm km\,s^{-1}}$) (right), for host halos whose mass is within 10^{11} and $10^{11.4}$ $M_\odot h^{-1}$. The red shaded area shows the range of MCF consistent with no correlation within 2-σ.

would be difficult to distinguish whether this signal is really coming from halo assembly bias.

On the other hand, in the regime below M_*, the dependence of the clustering strength on halo concentration switches sign, but the dependence of $N_{\rm sat}$ on concentration remains the same: host halos that form earlier still have fewer subhalos at a fixed mass. As a result, in the regime below M_*, halos in pairs are on averaged more massive and *more* concentrated, and these two characters have opposite effects on $N_{\rm sat}$. If a negative excess in the MCF of $N_{\rm sat}$ is detected, this signal must come from the contribution of concentration, or halo assembly bias. However, in Wechsler et al. (2006), there were not enough subhalos resolved in the simulation for the correlation between subhalo abundance and halo concentration to manifest itself, and hence this signal was not detected.

We first calculate the MCFs of halo concentration and of satellite occupation by selecting all resolved subhalos whose $v_{\rm max} > 60\,{\rm km\,s^{-1}}$ in our cosmological box, for host halos in a mass range, 10^{11}–$10^{11.4}$ $M_\odot h^{-1}$, and plot the results in Figure 5.12. The result we found here is consistent with previous studies: significant bias in concentration, but not in satellite occupation. This result, however, does not directly answer whether or not the satellite occupation can probe assembly bias, because the variance in $N_{\rm sat}$ can be large. As we argued in Section 5.3,

$$(N_{\rm sat}|M, c) \sim {\rm Pois}(\langle N_{\rm sat}|M, c\rangle). \tag{5.14}$$

For host halos in this mass range, the number of resolved subhalos is typically less than 10, even for a high-resolution cosmological box (e.g., with a particle mass of $10^7 M_\odot h^{-1}$). Despite the correlation between subhalo abundance and host halo concentration, the scatter in subhalo abundance can wash out this correlation, especially for host halos with few subhalos, and render the bias in subhalo occupation unobservable.

To verify our conjuncture that Equation 5.12 would hold for low-mass halos if the typical value of $N_{\rm sat}$ is large (> 10), one would need a cosmological box large enough to measure clustering statistics and with a particle mass of $\sim 10^5 M_\odot h^{-1}$, but this kind of simulation is still beyond the reach of current computational capabilities. Zoom-in simulations can easily provide a much better resolution, but those do not provide large-scale statistics. With our model, we can predict the expected number of subhalos (satellites) to a lower velocity cut (higher number density), while preserving the dependence on host halo mass and concentration. We then can quantify at what velocity cut (number density) we can start to observe the bias in subhalo occupation in low-mass host halos.

Figure 5.13 shows the model-predicted MCF of subhalo occupation for four different thresholds, in the same mass range of the host halos, 10^{11}–$10^{11.4}$ $M_\odot h^{-1}$. The host halos are selected from the cosmological box, and for each host halo we re-populate its subhalos with our model. At $v_{\rm max} = 60\,{\rm km\,s^{-1}}$ the result can be directly compared with the right panel of Figure 5.12. Since our model by construction correlates subhalo abundance and halo concentration ($V_{\rm max}/V_{\rm vir}$), the lack of signal in the MCF at $v_{\rm max} = 60\,{\rm km\,s^{-1}}$ results from the Poisson scatter. Moving the threshold down to $v_{\rm max} = 40\,{\rm km\,s^{-1}}$ we start to see a clear negative excess in the MCF. As we discussed above, this negative excess must originate from the fact that paired halos are on averaged more concentrated, and hence have fewer subhalos.

This negative excess in the MCF would manifest in the projected correlation function by lowering the one-halo term if the low-threshold data is available. With upcoming deep

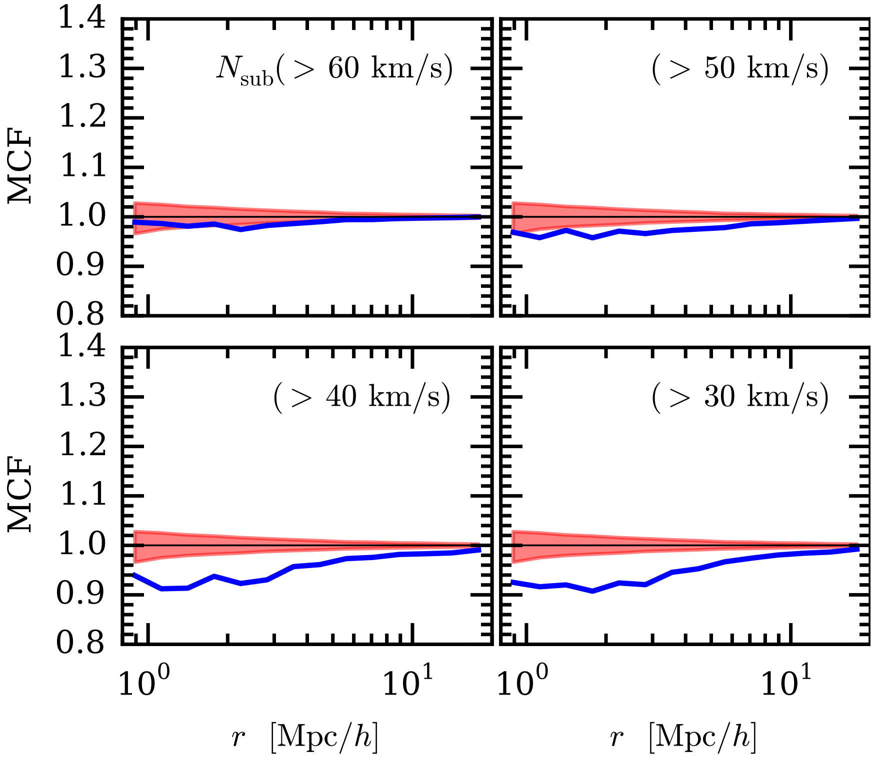

Figure 5.13: Same as Figure 5.12, but shows the MCFs of *model-predicted* satellite occupation down to 60, 50, 40, and 30 km s^{-1}. The corresponding number densities are 0.122, 0.216, 0.38, 1.03 (Mpc/h)$^{-3}$.

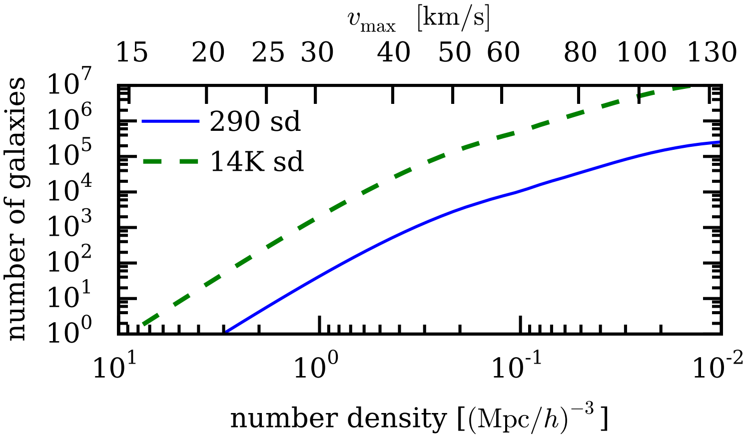

Figure 5.14: Expected number of galaxies in a volume-limited sample as a function of number density (and corresponding halo $v_{\rm max}$) for two example surveys with different sky coverage (given in square degrees).

spectroscopic surveys, such as DESI (Levi et al., 2013), data with low thresholds will be accessible in the near future. Figure 5.14 demonstrates the number of galaxies in a volume-limited sample from two exemplary surveys, assuming the luminosity function reported in Blanton et al. (2003, 2005a). Both surveys have a detection limit of $m_r = 19.5$, and their sky coverages are 290 and 14,000 square degrees, roughly representing the GAMA Survey[7] (Driver et al., 2011) and the DESI Bright Galaxy Survey,[8] respectively. With the latter survey, a volume-limited sample of a few hundred thousand galaxies with $m_r < 19.5$ down to the number density at $0.4\ (\mathrm{Mpc}/h)^{-3}$ would be accessible, and this sample would be sufficient for a precise measurement of the projected correlation function.

We note that although we assume the simple relation of Equation 5.10 in this discussion, this signal has the advantage that it is less sensitive to the details of the galaxy–halo relation because it only utilizes the number of satellites above a certain luminosity threshold, but not other properties (e.g., color) of the satellites. Even if galaxy formation introduces additional scatter in the satellite occupation, as long as this scatter is smaller than the halo-to-halo scatter due to halo concentration, this signal would survive in the projected correlation function.

5.5 Summary

In this work, we model the subhalo abundance on the basis of individual halos. The framework of our model is based on the fact that the scatter in N_{sub} for an *individual* halo is consistent with Poisson scatter, and the additional halo-to-halo scatter in N_{sub} for halos *in a mass bin* primarily affects only the overall normalization of the subhalo function. For a large sample of halos, we find that the subhalo velocity functions of a sample of halos in a mass range are nearly parallel to one another. As a result, we can model this halo-to-halo scatter by introducing additional parameters to the model that specify the normalization as a function of additional halo properties.

---

[7] `http://www.gama-survey.org/`

[8] `http://desi.lbl.gov/cdr/`

We hence present a model which predicts the subhalo abundance based on two properties: $V_{\rm vir}$ (equivalent to mass) and $V_{\rm max}/V_{\rm vir}$ (roughly equivalent to concentration) of the host halos. This model successfully reproduces the mean and scatter in the subhalo abundance in a given host halo mass bin. It can then be used to predict the number of subhalos for thresholds that are lower than the resolution limit of the simulation. It also enables one to conveniently sample a sequence of $v_{\rm max}$ values that represent the subhalos of a given host halo.

This model further provides plain insight into the dependence of subhalo abundance on halo concentration. We found that the halo concentration affects the subhalo abundance function mainly through the overall normalization (V_0 in our parameterization), but also through the "cutoff" scale ($V_{\rm cut}$). A constant power-law index (n) fits the cosmological simulations well; however, we also find that an index that depends on halo mass would fit the zoom-in Milky Way halos better. This dependence on mass may have the same physical origin as the dependence on redshift.

With this model, we then investigate the observable implications of the correlation between the subhalo abundance and halo concentration. We find that when using subhalo or satellite occupation as a proxy of halo mass, one might need to consider using a concentration-dependent model, such as the one presented here, to obtain a more accurate inference. We show that ignoring this dependence on concentration could result in a biased mass inference and an incorrect joint distribution of mass and concentration of the sample. Although these biases are small, they may become important as other sources of systematic errors decrease.

We further propose that satellite occupation can be used to probe halo assembly bias if we can detect all satellites which reside in subhalos down to $\sim 40\,{\rm km\,s^{-1}}$. Because in the low-mass regime, high-concentration halos are more clustered but have fewer subhalos, this signal can probe the halo assembly bias in concentration and is *not* degenerate with the contribution from halo mass. This method is also less sensitive to the detailed galaxy formation processes because it only depends on the total count.

Chapter 6

The Flexibility in the Galaxy–Halo Connection

An earlier version of this chapter was published as a preprint:

- B. V. Lehmann, Y.-Y. Mao, M. R. Becker, S. W. Skillman, R. H. Wechsler, "The Concentration Dependence of the Galaxy–Halo Connection," arXiv:1510.05651v1 [astro-ph.CO] (2015)

The chapter presented here has been revised to incorporate new results (e.g., Section 6.5.3) and also many improvements to the presentation of the manuscript.

Abstract Empirical methods for connecting galaxies to their dark matter halos have become essential in interpreting measurements of the spatial statistics of galaxies. In this work, we present a novel approach for parameterizing the degree of concentration dependence in the abundance matching method. This new parameterization provides a smooth interpolation between two commonly used matching proxies: the peak halo mass and the peak halo maximal circular velocity. This parameterization controls the amount of dependence of galaxy luminosity on halo concentration at a fixed halo mass. Effectively this interpolation scheme enable abundance matching models to have adjustable assembly bias in the resulting galaxy catalogs. With the new $400\,\mathrm{Mpc}\,h^{-1}$ DarkSky Simulation,

whose larger volume provides lower sample variance, we further show that low-redshift two-point clustering and satellite fraction measurements from SDSS can already provide a joint constraint on this concentration dependence and the scatter within the abundance matching framework. We also find that the choice of using peak values for abundance matching proxy is favored by the current clustering observations.

6.1 Introduction

Understanding the connection between galaxies and their dark matter halos is at the heart of modern cosmology and astrophysics. Galaxies are our primary tool to probe the spatial distribution of dark matter and its evolution, both of which are being mapped at increasingly high precision with cosmological surveys. However, because galaxies are biased tracers of this distribution, taking full advantage of these measurements requires accurate and flexible models for modeling the connection between galaxies and their dark matter halos. In addition, understanding the statistical mapping between galaxies and halos provides key insights into the physical processes responsible for galaxy formation.

The effects of assembly bias in particular remain a significant uncertainty in modeling the galaxy–halo connection (Zentner et al., 2014). In dark matter-only cosmological simulations, it has been shown that halo concentration, along with other properties of the halos and their assembly histories, can have an impact on halo clustering, generally known as halo assembly bias (e.g., Wechsler et al., 2001; Gao et al., 2005b; Wechsler et al., 2006; Croton et al., 2007). Despite a series of studies on the observational evidence for assembly bias (Yang et al., 2006; Tinker et al., 2012; Lin et al., 2016; Miyatake et al., 2015; More et al., 2016), the extent to which halo assembly bias results in observable bias in the galaxy population remains highly uncertain.

Thus it is critical to characterize the assembly bias inherited through the galaxy–halo connection. For hydrodynamic simulations and semi-analytic models (SAMs), galaxy assembly bias is an end product rather than a controlled parameter, as these two methods attempt to incorporate the microscopic physics of galaxy formation. (For the latest large-scale hydrodynamic simulations, see e.g., Vogelsberger et al. 2014; Chaves-Montero et al. 2015; for SAMs, see e.g., Bower et al. 2006; Croton et al. 2006; Somerville et al. 2008.) In principle, one can characterize directly the assembly bias for each set of parameter values used in these methods. Practically, hydrodynamic simulations are computationally expensive, even when used to produce a handful of realizations. With SAMs, while it is possible to generate many different realizations, the large number of parameters makes it challenging (though not impossible, see e.g., Lu et al., 2014; Henriques et al., 2015) to explore and statistically constrain the full parameter space. Also, neither hydrodynamic simulations nor SAMs have been shown to reproduce the detailed clustering properties of observed galaxies at the accuracy with which they have been measured, partly due to our incomplete understanding of star formation and feedback mechanisms.

On the other hand, the widely-used, conventional halo occupation distribution (HOD) models prescribe the probability that a halo of a given mass M hosts N galaxies above a given luminosity threshold, $P(N|M)$, commonly with a parameterized functional form (Peacock & Smith, 2000; Seljak, 2000; Scoccimarro et al., 2001; Berlind & Weinberg, 2002; Cooray & Sheth, 2002; Bullock et al., 2002). In this fashion, the HOD approach erases much of the halo assembly bias, as it explicitly assumes that the galaxy population in a halo depends only on its mass. Recently, some HOD models incorporate dependence on other parameters (e.g., Paranjape et al., 2015; Hearin et al., 2016). In particular, Hearin et al. (2016) (submitted shortly after this work) parameterize the assembly bias in an HOD-like model, and the approach is closely related to this work.

In this work, we characterize the assembly bias in another commonly used empirical model of the galaxy–halo connection: the abundance matching technique (or subhalo abundance matching, SHAM). Abundance matching is a fairly generic scheme for linking galaxies with dark matter halos, without a full description of baryonic physics (Kravtsov et al., 2004; Vale & Ostriker, 2004, 2006; Conroy et al., 2006). The basic assumption of abundance matching is that galaxies live in halos, and one particular galaxy property (typically luminosity or stellar mass) is approximately monotonically related to a halo property (typically virial mass, $M_{\rm vir}$, or maximum circular velocity, $v_{\rm max}$), by matching their "abundance" (i.e., matching at fixed number densities).

A major strength of abundance matching is the fact that it uses the full predictive power of the cosmological model, including the predictions for the number and properties of substructures and their relation to their host halos. Certain abundance matching models have been shown to reproduce the observed two-point correlation function with surprising accuracy, with only a very small number of parameters (Conroy et al., 2006; Trujillo-Gomez et al., 2011; Reddick et al., 2013), as well as three-point statistics, galaxy-galaxy lensing, and the Tully–Fisher relation (e.g., Marín et al., 2008; Tasitsiomi et al., 2004; Desmond & Wechsler, 2015). Similar models have also been shown to reproduce a wide range of other statistics of the galaxy distribution (Hearin et al., 2013a, 2014).

The abundance matching parameters that have typically been considered are the *scatter* in the galaxy–halo relation, usually in terms of the standard deviation of the galaxy luminosities or stellar masses at a fixed value of the halo property, and the choice of halo property. Commonly used halo properties (or *proxies*) include the halo mass ($M_{\rm vir}$ or variants), the maximum circular velocity $v_{\rm max}$, and these two properties evaluated at different epochs. For example, Reddick et al. (2013) perform a systematic search for a best-fit model to spatial clustering and the conditional luminosity function and find that using the peak value of $v_{\rm max}$ throughout all timesteps (i.e., $v_{\rm peak}$) as the proxy with a scatter of ~ 0.2 dex gives the best predictions. Other studies obtain similar results (e.g., Chaves-Montero et al., 2015; Guo et al., 2016).

Although different proxies have different physical meanings attached to them, abundance matching is only sensitive to the relative rankings of halos when they are ranked by the proxy in consideration. Hence, the seemingly distinct choices of using proxies based on $v_{\rm max}$ or $M_{\rm vir}$ are merely different ways to rank the halos. For instance, ranking halos by $v_{\rm max}$ is similar to ranking by $M_{\rm vir}$, except that more concentrated halos are given a higher rank, since at a fixed $M_{\rm vir}$, more concentrated halos have larger $v_{\rm max}$ (Klypin et al., 2011). As a result, this choice influences the dependence of galaxy luminosity or stellar mass on halo concentration at a given halo mass. Our current understanding of galaxy formation physics is not yet sophisticated enough to quantify this concentration dependence, and hence it is natural to *parametrize* this dependence on concentration by continuously interpolating the rankings that different proxies give. Furthermore, such a parametrization also provides a natural way to control how halo assembly bias propagates to galaxy assembly bias in an observed population.

This work is the first to present results on the clustering statistics using abundance matching with a continuous parameter controlling the matching proxy, and hence the amount of concentration dependence and assembly bias. This work is also the first to compare the observed two-point clustering with a cosmological box of $(400\,\mathrm{Mpc}\,h^{-1})^3$ at a mass resolution of better than $\sim 10^8\,M_\odot h^{-1}$ (from the "Dark Sky" Simulations). The large volume of this box yields much tighter constraints on abundance matching parameters, which provide further insight into the amount of galaxy assembly bias present.

Note that this work differs from the recent development on the two-parameter abundance matching technique (commonly known as conditional abundance matching, CAM), which attempts to match two halo proxies with two galaxy properties (Hearin et al., 2014; Kulier & Ostriker, 2015). The model we propose in this work, by contrast, still matches one halo proxy with one galaxy property, yet the halo proxy in consideration is a linear combination of two different halo properties. The proposed technique to combine distinct halo properties into one matching proxy can still apply to other variants of abundance matching, including CAM.

This chapter is organized as follows. In Section 6.2 we describe the simulations and the observed catalogs used in this study, and also describe the procedure for generating mock galaxy catalogs and the covariance. In Section 6.3 we present this novel model of concentration-dependent abundance matching and explore how the new parameter affects the galaxy clustering, the satellite fraction, and the assembly bias. In Section 6.4 we compare the galaxy clustering signals from this model and from observations to constrain the model parameters. We then discuss some detailed aspects of our results in Section 6.5. In particular, we test whether the choice of using peak values for matching proxy is a physical choice. We summarize this chapter in Section 6.6.

Box name	Side length [Mpc h^{-1}]	Particle number	h	Ω_M	n_s	σ_8	Particle mass [$M_\odot h^{-1}$]	Code
`c250-2048`	250	2048^3	0.7	0.286	0.96	0.82	1.44×10^8	L-GADGET
`Bolshoi`	250	2048^3	0.7	0.27	0.95	0.82	1.35×10^8	ART
`BolshoiP`	250	2048^3	0.678	0.295	0.968	0.823	1.49×10^8	ART
`MDPL`	1000	3840^3	0.678	0.307	0.96	0.823	1.51×10^9	L-GADGET
`DarkSky-250`	250	2560^3	0.688	0.295	0.968	0.834	7.63×10^7	2HOT
`DarkSky-400`	400	4096^3	0.688	0.295	0.968	0.834	7.63×10^7	2HOT
`DarkSky-Gpc`	1000	10240^3	0.688	0.295	0.968	0.834	4.88×10^9	2HOT

Table 6.1: Cosmological and simulation parameters for boxes used in this study. See Chapter 2 for more details. For `DarkSky-Gpc`, the halo catalogs and merger trees are constructed with 1/32 of the total particle number. The particle mass for `DarkSky-Gpc` in this table is the effective mass of the downsampled particles.

6.2 Simulations and Galaxy Catalogs

6.2.1 Simulations

This study uses several cosmological boxes that are described in Chapter 2. We list the boxes used in this study in Table 6.1. The `c250-2048` box comes from the “Chinchilla” suite, run with the L-GADGET code, a variant of GADGET (Springel, 2005). The “Chinchilla” suite spans a wide range of box sizes and resolutions with the same cosmology. `Bolshoi` and `BolshoiP` have the same box size and resolution as `c250-2048`, but have different cosmologies and were run with the ART N-body code (Klypin et al., 2011). `MDPL` is part of the “MultiDark” suite (Klypin et al., 2014), and was also run with GADGET. The three `DarkSky` boxes of different sizes are smaller boxes that accompany the 8 Gpc h^{-1} box from the “Dark Sky” Simulations (Skillman et al., 2014), run with the 2HOT code (Warren, 2013). Here we refer to these boxes as `DarkSky-250 (ds14_j_2560)`, `DarkSky-400 (ds14_i_4096)`, and `DarkSky-Gpc (ds14_b)`. The particles used to build the halo catalogs and merger trees for the `DarkSky-Gpc` box were down-sampled (1/32 particles) from a high-resolution box run with 10240^3 particles.

For each of these boxes, we use the halo catalog generated by the ROCKSTAR halo finder (Behroozi et al., 2013a) and the CONSISTENT TREES merger tree builder (Behroozi et al., 2013b). We use the virial overdensity (Δ_{vir}) as our halo mass definition (Bryan & Norman, 1998).

6.2.2 Mock Galaxy Catalogs

The mock galaxy catalogs used in this work are generated with the abundance matching technique. We follow the procedure of Behroozi et al. (2010) and Reddick et al. (2013) in order to implement abundance matching with scatter in luminosity at fixed halo proxy. First we deconvolve the scatter from the luminosity function. We then abundance match luminosity with the halo proxy, producing a catalog of galaxy luminosities. Finally, we replace the scatter by adding a log-normal scatter to the catalog.

We make measurements of the projected two-point correlation function, $w_p(r_p)$, from the mock catalogs as follows. We use the plane-parallel approximation in redshift-space and integrate along one of the axes (i.e., the line-of-sight), with integration depth $2z_{\rm max} = 80\,{\rm Mpc}\,h^{-1}$. Redshift-space distortions are applied along the integration axis before integration. We account for the periodic boundary conditions of the cosmological boxes when computing the projected correlation function in the directions perpendicular to the integration axis.

6.2.3 SDSS Galaxy Catalogs

In this study, we use the luminosity function (for abundance matching) and the two-point clustering measurements (for comparison) extracted by Reddick et al. (2013). These measurements were made on the volume-limited samples from the New York University Value Added Galaxy Catalog (NYU-VAGC) (Blanton et al., 2005b), based on Data Release 7 from the Sloan Digital Sky Survey (Padmanabhan et al., 2008; Abazajian et al., 2009). We note that these measurements are quite consistent with the measurements of Zehavi et al. (2011), but here a consistent sample was used to determine both the luminosity function and clustering measurements. We refer the readers to Section 2 and Appendix C of Reddick et al. (2013) for details on these measurements. In this work, we focus primarily on constraining our models with galaxies of luminosity $\sim L_*$ and brighter in order to be conservative about the resolution requirements for the complete halo and subhalo samples needed for abundance matching, but we present results from dimmer samples in Section 6.4.4.

6.2.4 Calculating the Covariance

In Section 6.4, when we compare the SDSS data to the predicted $w_p(r_p)$ obtained from the mock catalogs with a χ^2 statistic, we use a covariance matrix composed of three parts. First, we estimate the sample variance in the predictions of abundance matching due to the finite volume of the N-body simulations used in this work. We employ a jackknife procedure in order to estimate the contribution to the covariance matrix from this effect. Each N-body box is divided into smaller *square* patches with a side length of $25\ \mathrm{Mpc}\,h^{-1}$. We then omit one patch at a time in the jackknifing process (i.e., omitting everything along the line of sight in the square patches), and compute the jackknife covariance. The second contribution to the covariance comes from the scatter in abundance matching. Since we apply log-normal random scatter in luminosity directly to the catalogs, multiple catalogs generated with the same abundance matching parameters produce slightly different predictions for $w_p(r_p)$. Thus, from each set of abundance matching parameters, we generate 40 catalogs, compute $w_p(r_p)$ for each, and calculate the covariance on $w_p(r_p)$ due to this random variation. Finally, we estimate the effects of sample variance in the SDSS measurements through jackknifing the SDSS dataset. These three contributions to the covariance matrix are added together to compute the χ^2 statistic.

We note that the estimate of the covariance of the mock $w_p(r_p)$ has a direct impact on the goodness of fit, and hence on the derived constraints on the abundance matching parameters. Nevertheless, Norberg et al. (2009) find that the jackknife method does not typically underestimate the covariance.

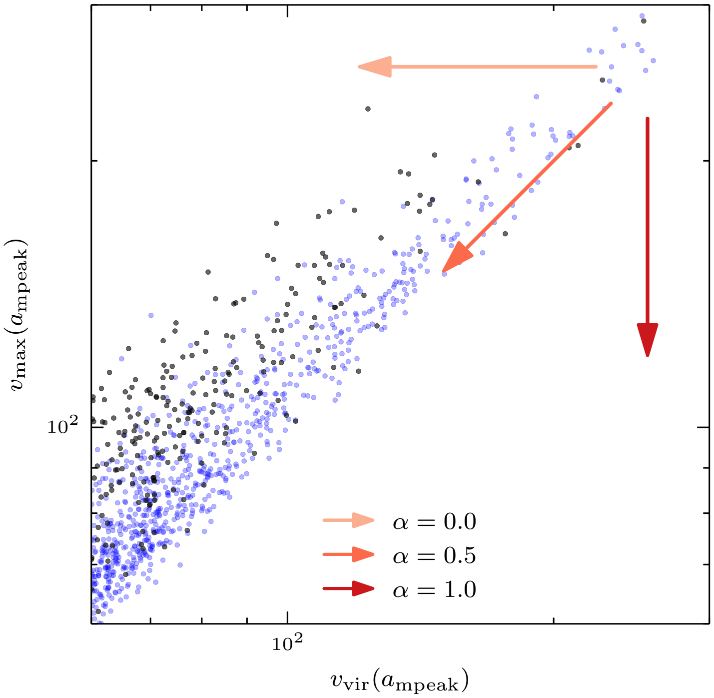

Figure 6.1: Relation between the two halo properties v_{vir} and $v_{\max}$ (both evaluated at a_{mpeak}) and abundance matching rankings. Each point represents a host halo (blue) or a subhalo (black). The total number of halos is down-sampled for illustration purposes. Each arrow shows the direction of decreasing abundance matching rank when a particular value of α is used (from light to dark: $v_{\alpha=0} = v_{\mathrm{vir}}$, $v_{\alpha=0.5}$, and $v_{\alpha=1} = v_{\max}$). The figure indicates how the choice of proxy impacts both the fraction of subhalos that are included in the sample, as well as the concentration of the included halos, which will impact their clustering properties.

6.3 Abundance Matching with Adjustable Concentration Dependence

6.3.1 Interpolating between Abundance Matching Proxies

Here we present an interpolation scheme which generalize the conventional abundance matching model to allow continuously adjustable concentration dependence. To build such a scheme, we adopt the parameterization used in Mao et al. (2015), defining a new generalized proxy to be used in abundance matching:

$$v_\alpha := v_{\rm vir}\left(\frac{v_{\rm max}}{v_{\rm vir}}\right)^\alpha, \tag{6.1}$$

where $v_{\rm max}$ is the maximal circular velocity and

$$v_{\rm vir} := \left(\frac{GM_{\rm vir}}{R_{\rm vir}}\right)^{1/2} = \left(\frac{4\pi}{3}\Delta_{\rm vir}\rho_{\rm crit}G^3\right)^{1/6} M_{\rm vir}^{1/3}, \tag{6.2}$$

with $\Delta_{\rm vir}$ being the virial overdensity and $\rho_{\rm crit}$ the critical density.

This generalized proxy captures the continuously-varying dependence on concentration through the parameter α because the ratio $v_{\rm max}/v_{\rm vir}$ can be viewed as a proxy for halo concentration. In principle, this ratio can be replaced by $f(c)$ with a general function f. Nevertheless, using this ratio facilitates comparisons with other proxies that have been used in the literature. In particular, when $\alpha = 0$, the dependence on concentration is turned off, as $v_{\alpha=0} = v_{\rm vir} \propto M_{\rm vir}^{1/3}$, and when $\alpha = 1$, this proxy reduces to the maximal circular velocity $v_{\alpha=1} = v_{\rm max}$.

Figure 6.1 illustrates how the value of α affects the ranking. In this log–log plot, an arrow represents the direction of descending rank when the halos are ranked by v_α, and the slope of the arrow is $\alpha/(1-\alpha)$. Hence, different values of α effectively rank the halos with different slopes. As a result, at a given number density, different values of α select out different halos. In particular, a larger value of α selects out more low-mass, high-concentration halos, and also more subhalos.

We note that the specific choice of the parameterization of the concentration dependence should not impact our results significantly, as the essence of our model is to vary how much we weight the concentration of halos when ranking halos by their masses in the abundance matching procedure. However, one could instead weight other halo properties, such as halo formation time, in order to study the dependence on other properties in abundance matching. In this work, we only study the dependence on concentration. Nevertheless, we expect qualitatively similar results would also apply to other proxies that are highly correlated with concentration.

6.3.2 Evaluating the Proxy at the Epoch of Peak Mass

So far we have only discussed how to model the concentration dependence in our new proxy. In abundance matching, the choice of epoch at which the ranking proxy is evaluated also significantly impacts the results (Reddick et al., 2013; Chaves-Montero et al., 2015). For example, if the proxy is evaluated at the present day, subhalos are usually ranked lower due to stripping, and the resulting mock catalog is less clustered. Conroy et al. (2006) argues that the time at which a subhalo enters the virial radius of its parent halo is a natural time at which to set proxies. Reddick et al. (2013) further uses the peak values of those proxies (e.g., $M_{\rm peak}$ and $v_{\rm peak}$) throughout history. In this work, we limit our discussion to a single choice of epoch. We evaluate the value of v_α for each halo at the epoch when $M_{\rm vir}$ reaches its peak value, and let $\hat{v}_\alpha$ denote this quantity. In follow-up work, we will explore this choice of proxy epoch in detail.

Since $\hat{v}_\alpha$ is evaluated at the time of peak mass for each halo, ranking with $\hat{v}_{\alpha=0}$ and $\hat{v}_{\alpha=1}$ is equivalent to ranking with $M_{\rm peak}$ and $v_{\rm max}$ at $M_{\rm peak}$ respectively. (However, the former is only approximately true in our case because $\Delta_{\rm vir}$ in Equation 6.2 has a weak dependence on the scale factor, and for different halos, $M_{\rm peak}$ occurs at different scale factors.) Our choice of evaluating the abundance matching proxy at the scale when $M_{\rm peak}$ rather than when $v_{\rm peak}$ occurs was motivated by the finding that halos at the largest circular velocities may be out of dynamical equilibrium (Ludlow et al., 2012); e.g. Behroozi et al. (2014) showed that $v_{\rm peak}$ is commonly set by major mergers, and hence may not represent the physical time at which the subhalo started to be stripped. Evaluating the proxy at the scale factor of $M_{\rm peak}$ then avoids this unphysical epoch probed by $v_{\rm peak}$, and is similar to using the relaxation criterion proposed by Chaves-Montero et al. (2015). Nevertheless, for the purpose of abundance matching, the difference between matching to $v_{\rm peak}$ and to $v_{\rm max}(a_{\rm mpeak})$ is minimal, as the rank orders are very similar when halos are ranked by these two proxies. As a result, the clustering signals with these two proxies are also similar.

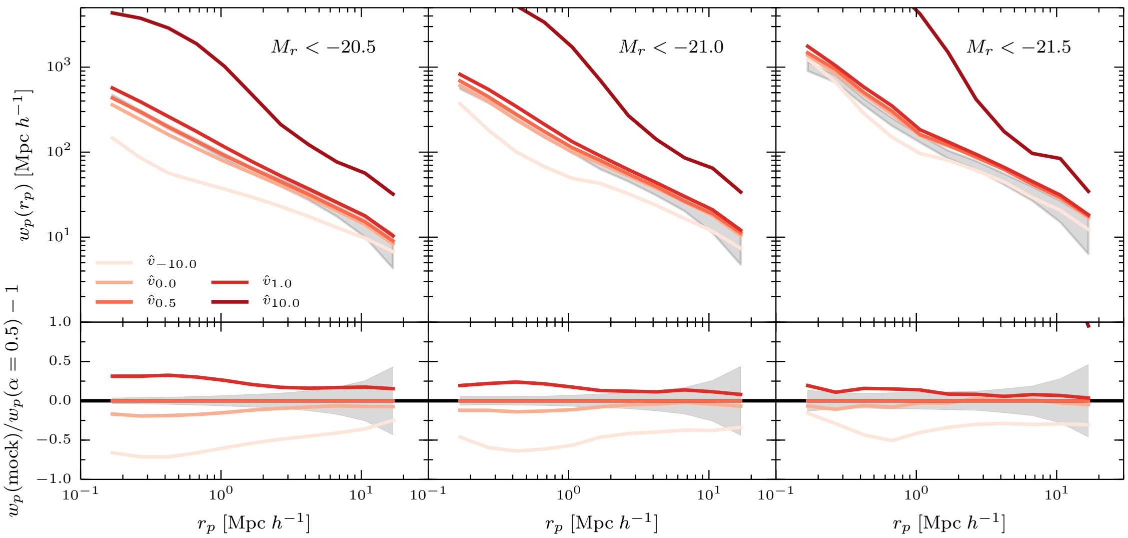

Figure 6.2: Dependence of galaxy clustering on the abundance matching proxy. Top row shows $w_p(r_p)$ for three thresholds ($M_r < -20.5$, -21, and -21.5; from left to right) in the `DarkSky-400` box. Lines of different colors shows different values of α (-10, 0, 0.5, 1, 10; from light to dark). Larger values of α correspond to stronger concentration dependence. The gray band shows the SDSS measurements and the errors combined with mock errors. Bottom row shows the relative difference in $w_p(r_p)$ with respect to $\hat{v}_{\alpha=0.5}$.

6.3.3 Impact of α on Clustering

We first demonstrate the impact of α, as defined in Section 6.3.1, on clustering. Figure 6.2 shows the wide range of clustering predictions that can be produced by varying α. We find that changing α can significantly change the clustering, and that a higher value of α produces a more clustered catalog.

There are two effects that contribute to this result. Firstly, at a given halo mass, on average, subhalos have higher concentrations than host halos. Hence, when a higher value of α is used, subhalos are more likely to make it through the threshold cut, resulting in a more clustered sample. Effectively, increasing α increases the difference between the luminosity–halo mass relation of host halos and that of subhalos. This effect impacts both the one- and two-halo terms, and also boosts the satellite fraction.

Secondly, when we use a higher value of α, high-concentration halos are ranked higher

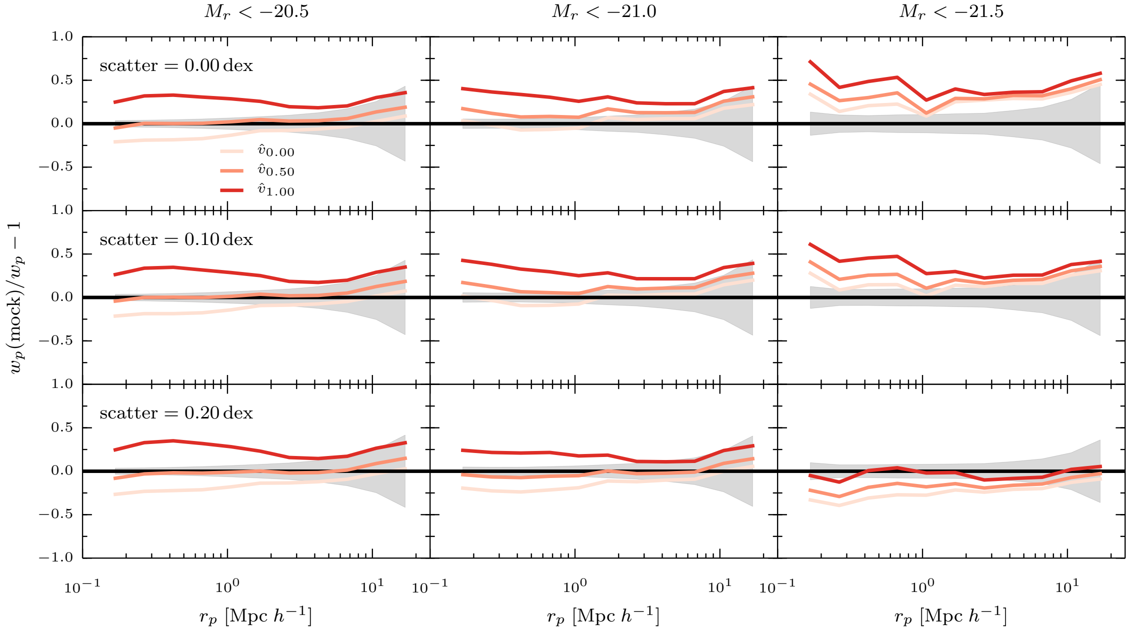

Figure 6.3: Dependence of galaxy clustering on the abundance matching scatter and proxy. Relative difference in $w_p(r_p)$ between the `DarkSky-400` galaxy catalog and the SDSS measurements, for three thresholds ($M_r < -20.5$, -21, -21.5; from left to right), three values of scatter (0, 0.15, 0.25; from top to bottom), and three values of α (0, 0.5, 1; from light to dark). Gray bands indicate combined SDSS and mock errors.

in the catalog and are more likely to make it through the threshold cut. Since in this mass regime, high-concentration halos are more clustered due to halo assembly bias (Wechsler et al., 2006), the resulting catalog is also more clustered. This effect impacts mostly the two-halo term, and is less significant in brighter samples. In the sections below, we discuss these two effects in detail.

It is known that increasing the scatter in abundance matching would decrease clustering strength because it brings in lower-mass halos (e.g., Reddick et al., 2013). Thus, there exists a degeneracy between α and the scatter. This degeneracy is demonstrated in Figure 6.3, which shows the correlation function for several values of α and scatter. The clustering strength decreases with decreasing α and also with increasing scatter. Nevertheless, the scatter has a stronger effect on the brighter samples, while α has a stronger effect on the fainter samples. This implies that samples of different thresholds are likely to give different constraints on α and scatter, and might be able to break the degeneracy between α and scatter.

6.3.4 Impact of α on Satellite Fraction

Here, we define the satellite fraction to be the fraction of satellites in bins of luminosity. In this study, we did not apply a group finder on the mock galaxies, so galaxies labeled as satellites are exactly the same as those labeled as *subhalos* in the initial halo catalog. That is, the satellite fraction we measured here is actually the fraction of galaxies assigned to *subhalos* in each luminosity bin. A *subhalo* is defined as any halo whose center falls within another larger halo. We refer to a halo that is not a subhalo as a host halo.

Figure 6.4 shows the satellite fraction as a function of luminosity for several values of α. As expected, increasing α increases the satellite fraction, since subhalos are on average more concentrated than host halos of the same mass; hence subhalos are ranked higher when α is larger. This is especially true at the faint end as the ratio $v_{\mathrm{max}}/v_{\mathrm{vir}}$ differs more between subhalos and host halos for low-mass halos.

Applying scatter to abundance matching increases the satellite fraction at the bright

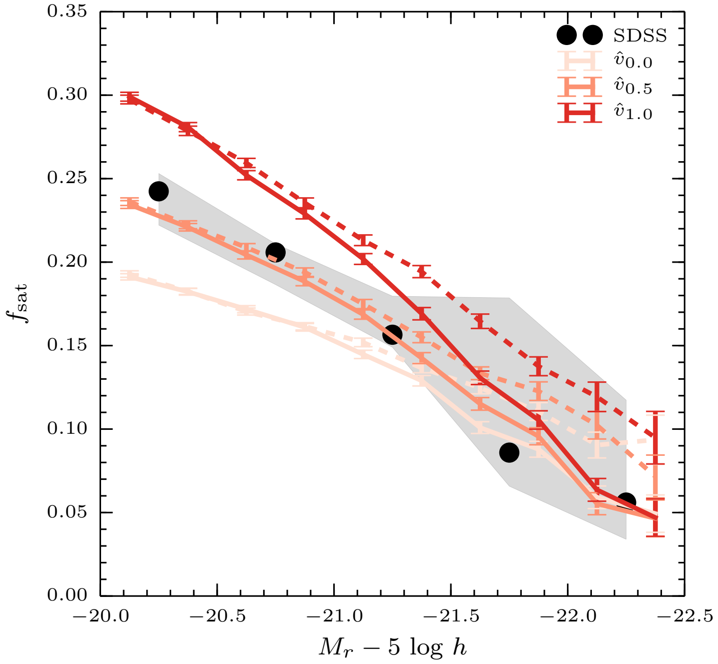

Figure 6.4: Satellite fraction as a function of luminosity, for three values of α (0, 0.5, 1.0; from light to dark), computed with zero scatter (solid) and 0.15-dex scatter (dashed), using the `DarkSky-400` box. Error bars show the jackknifing error. Circles show the satellite fraction measured from SDSS groups (Reddick et al., 2013), and the gray band indicates the sum of the error from SDSS data and the estimated systematic error introduced by the group finder (see text of Section 6.3.4 for detail).

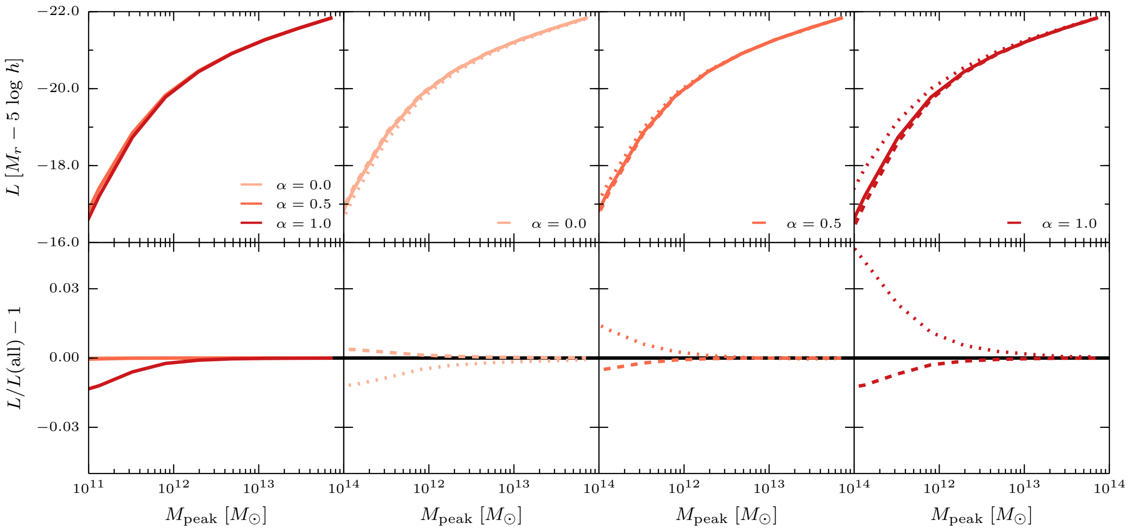

Figure 6.5: Luminosity–halo mass relation for several values of α (0, 0.5, 1.0; from light to dark). Lines with different styles show the relation for all halos (solid), host halos only (dashed), and subhalos (dotted) only. The leftmost top panel shows that the value of α has very little effect on the relation that includes all halos. The right three panels show that the difference between the relations of central halos and subhalos increases with α. The bottom row shows the relative difference with respect to the relation for all halos (and for the leftmost bottom row, with respect to the relation for $\alpha = 0$).

end because more satellites in the fainter luminosity bins are scattered up to the brighter luminosity bins. Applying scatter does not significantly change the satellite fraction for samples fainter than $M_r = -21$.

Another way to demonstrate this change in the satellite fraction is to look at the difference between the luminosity–halo mass relation of host halos (central galaxies) and that of subhalos (satellite galaxies). Previous studies have explored the case in which the stellar mass–halo mass relations of central and satellite galaxies differ from each other (e.g., Neistein et al., 2011; Rodríguez-Puebla et al., 2012, 2013a). Here, using the α parameter we can evaluate this difference quantitatively. Figure 6.5 shows the luminosity–halo mass ($L - M_h$) relations for all halos, only host halos, and only subhalos, for different values of α. We see that changing α changes the overall $L - M_h$ relations very little, but changes the difference between the halo and subhalo $L - M_h$ relation. Specifically, increasing α effectively more strongly differentiates the $L - M_h$ relations for halos and subhalos, while maintaining the overall $L - M_h$ relation.

In Figure 6.4, we also compare our results with the observed satellite fraction. The observed satellite fraction measurements are taken from Reddick et al. (2013), who used a group finder (Tinker et al., 2011) applied to the same sample used to make the clustering measurements. Since we did not apply the same group finding procedure on our mock catalogs, this comparison is subject to the systematic errors introduced by the group finder. The gray band shown in Figure 6.4 is the sum of the error from SDSS data *and* the estimated systematic error introduced by the group finder; the latter was estimated by taking the one-sided difference between the satellite fractions before and after the catalog was processed with a group finder, shown in the left panel of Figure 21 in Reddick et al. (2013). We see that these systematic errors increase significantly at the bright end, due to the fact that the group finder does not always select the right galaxy as the central. However, both scatter and group finding have much a smaller impact at luminosities dimmer than $M_r = -21$, which is also where α has a larger impact. Up to the systematic errors, the observed satellite fraction agrees well with the model prediction when $\alpha \sim 0.5$. We show in Section 6.4.2 that this is also consistent with the inference from galaxy clustering.

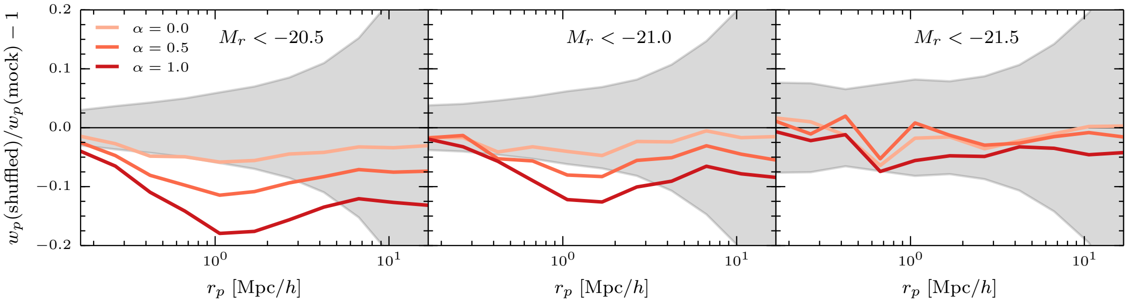

Figure 6.6: Relative difference in $w_p(r_p)$ between shuffled and unshuffled catalogs for three thresholds ($M_r < -20.5, -21, -21.5$; from left to right) and three values of α (-1, 0, 0.5, 1; from light to dark), for the `DarkSky-400` box. No scatter is applied in the abundance matching procedure. The gray band shows the combined error from the observed data and the mock catalogs. Assembly bias increases the large-scale clustering in our best-fit model by $\sim 8\%$ for the dimmest sample shown here.

6.3.5 Impact of α on Assembly Bias

In our model, α also controls how much halo assembly bias can manifest in the mock catalogs as galaxy assembly bias. To quantify this, we need to separate the effects of the satellite fraction and halo assembly bias. To that end, we shuffle our mock catalogs to remove halo assembly bias, but leaving the satellite fraction intact. Here we adopt the same shuffling procedure as described by Zentner et al. (2014). We divide the catalogs into bins of halo masses, with a bin width of 0.1 dex. For each bin, we first shuffle the central galaxies, and then independently shuffle the satellites (while retaining their relative positions to the central galaxies). This procedure preserves the halo occupation and the satellite fraction in the catalogs by construction.

Figure 6.6 shows the relative difference in $w_p(r_p)$ between the shuffled and unshuffled catalogs. Since the shuffling procedure preserves the satellite fraction, the difference seen in this figure comes from halo assembly bias alone. We see that the difference is larger for fainter samples and for larger values of α. This behavior is expected: halo assembly bias impacts the fainter samples more strongly, and catalogs with a larger value of α have stronger halo assembly bias and are more clustered. We note here that although models with more concentration dependence have stronger assembly bias, there is still some assembly bias in the models with $\alpha = 0$, because the relationship between $M_{\rm vir}$ and $M_{\rm peak}$ has some dependence on formation time and/or halo concentration.

Figure 6.6 also shows the scale dependence of assembly bias for each value of α. We find that halo assembly bias impacts both the two-halo term and the transition regime around 1–2 Mpc h^{-1}, in agreement with the findings of Sunayama et al. (2016). At the smallest scales, the original catalog and the shuffled catalog exhibit similar clustering, since the clustering at small scales is dominated by the change in satellite fraction. This implies that our $\hat{v}_\alpha$ model is distinct from merely introducing halo assembly bias to a non-biased catalog (e.g., modeling the halo occupation distribution). In particular, varying α simultaneously changes the amount of halo assembly bias and the satellite fraction.

6.4 Constraining the Concentration-dependent Model

6.4.1 Jointly Constraining α and Scatter

In the previous section we present how this α parameter, which controls the concentration dependence in abundance matching, affects the clustering signals in the mock catalog. Given this finding, here we investigate whether the current galaxy clustering measurement can already provide constraints on the this α parameter. Since the effect of the α parameter on the clustering signals and that of the scatter in abundance matching are degenerate, here we present the joint constraints on α and scatter using the SDSS galaxy catalog.

We compute the χ^2 statistic to evaluate the goodness-of-fit for a set of values in the $(\alpha, \text{scatter})$ parameter space for each threshold. We also compute the χ^2 statistic for several different cosmological boxes to determine whether the constraint on $(\alpha, \text{scatter})$ varies significantly between boxes using different cosmologies and codes.

The χ^2 statistic is computed as

$$\chi^2 = \sum_i \sum_j d(r_p^i) d(r_p^j) C^{-1}(r_p^i, r_p^j), \tag{6.3}$$

where $d(r_p) := w_p^{\mathrm{mock}}(r_p) - w_p^{\mathrm{SDSS}}(r_p)$, $C(r_p^i, r_p^j)$ is the covariance, and i, j denote the indices of the bins of r_p. Note that here C already includes the covariance from the SDSS data, as well as the covariance from jackknifing the mock catalog and from multiple realizations of abundance matching.

Figure 6.7 shows the constraints from the three `DarkSky` boxes and the `MDPL` box for four different luminosity thresholds separately. Note that the two $1\,\mathrm{Gpc}\,h^{-1}$ boxes do not have the resolution to generate a complete sample below roughly $M_r = -21$, and hence we omit the lowest luminosity panels for these boxes in Figure 6.7. We will discuss detailed resolution requirements for abundance matching in upcoming work.

We see several interesting features here. First, the degeneracy between α and scatter is most visible in the samples of $M_r < -21.5$ and -21. In both cases we see the degeneracy as expected: a larger α requires a larger scatter to balance the additional clustering since more highly concentrated halos are included.

Second, as expected, larger boxes provides stronger constraints, indicating that the constraining power of most previous studies, which have almost exclusively used boxes of $\sim 250\,\mathrm{Mpc}\,h^{-1}$ on a side, have been dominated by sample variance. This is especially true for the brighter samples, as the numbers of galaxies in those samples are small. While the sample of $M_r < -22$ from `DarkSky-250` and `-400` provide little constraint on α and scatter, the samples from the $1\,\mathrm{Gpc}\,h^{-1}$ boxes give clear constraints on scatter, and exclude zero scatter in this range of α at $p < 0.001$.

Third, on the faint end, we obtain a much stronger constraint on α. The luminosity dependence of halo bias is significantly weaker in this regime, and thus these galaxies do not provide strong constraints on scatter. However, with `DarkSky-400`, this sample excludes both $\alpha = 0$ and 1 at $p < 0.001$.

6.4.2 Combining Constraints from Different Thresholds

If we assume that α and scatter are constant with respect to luminosity, then the samples at different thresholds can be combined to produce an overall constraint on α and scatter. Here,

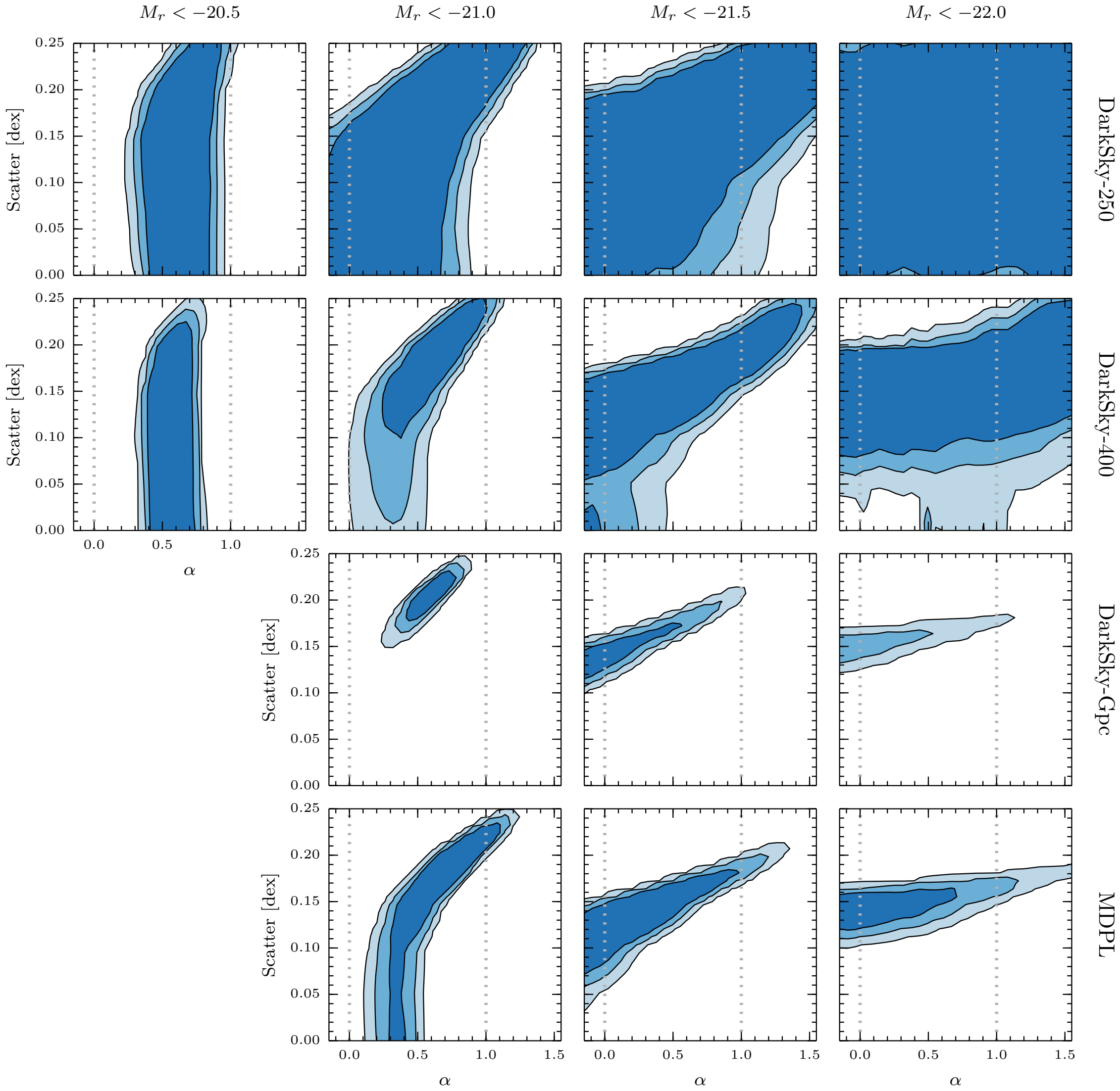

Figure 6.7: Constraints on α and scatter in each of the three `DarkSky` boxes and the `MDPL` box, for four thresholds ($M_r < -20.5$, -21, -21.5, -22; from left to right). The contours, from dark to light blue, show the one-side p-value of 0.05, 0.01, and 0.001 for the χ^2 fit.

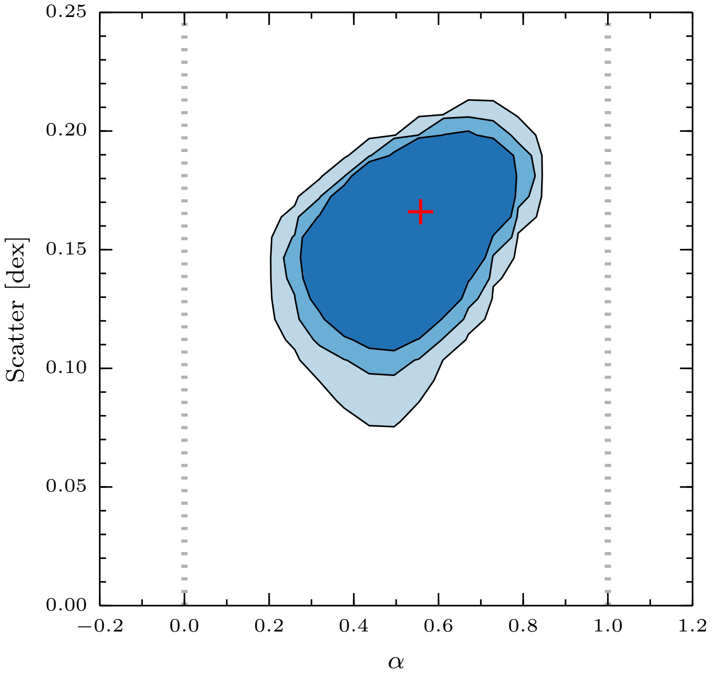

Figure 6.8: The combined joint constraint on α and scatter from four thresholds ($M_r <$ -20.5, -21, -21.5, -22.0) for `DarkSky-400`. The contours, from dark to light blue, show the one-side p-value of 0.05, 0.01, and 0.001 for the χ^2 fit. Crosshairs show best-fit point ($\alpha = 0.57^{+0.20}_{-0.27}$; scatter $= 0.17^{+0.03}_{-0.05}$ dex).

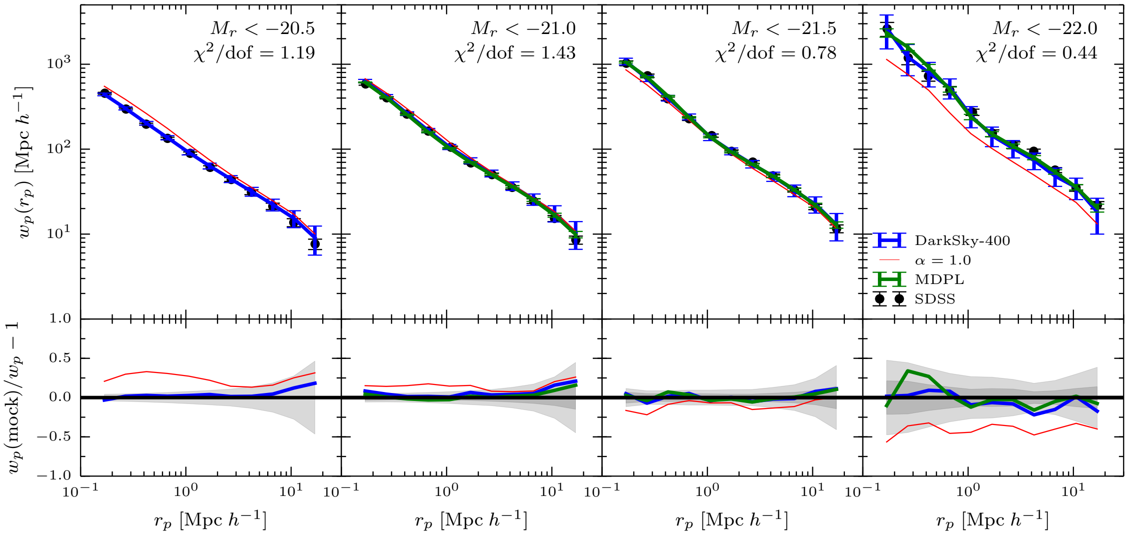

Figure 6.9: Comparison between our best-fit model and SDSS data. Top row shows the best-fit $w_p(r_p)$ for `DarkSky-400` (blue line; $\alpha = 0.57$; scatter = 0.17 dex) and `MDPL` (green line; $\alpha = 0.49$; scatter = 0.16 dex). The χ^2 values are shown for `DarkSky-400` at each threshold. Circles show SDSS $w_p(r_p)$. Four columns represent four thresholds ($M_r < -20.5$, -21, -21.5, -22; from left to right). To compare with previous work, the red line shows $\hat{v}_{1.0}$ model with best-fit scatter of 0.22 dex in `DarkSky-400` (χ^2/dof = 8.9, 2.5, 1.9, 1.8 for the four thresholds respectively). `MDPL` is omitted from the $M_r < -20.5$ column, which is not used in fit computation for that box. Bottom row shows the relative difference with respect to SDSS data. Gray bands indicate combined SDSS and mock errors: the outer region indicates combined errors for `DarkSky-400`, while the inner region indicates combined errors for `MDPL`.

we also assume that the constraints from samples at different thresholds are independent. This assumption is only approximately correct for two reasons. First, although the sample at each threshold is dominated by the fainter galaxies, it does include galaxies from higher thresholds. Second, for a given simulation, the clustering signals at different thresholds are also correlated. Here we assume the independence for simplicity, and because the effects are both small, we do not expect that they will significantly impact our conclusions.

The combined constraint from four thresholds ($M_r < -20.5, -21, -21.5, -22$) for `DarkSky-400` is shown in Figure 6.8. This combined constraint excludes both $\alpha = 0$ (resembling M_{peak}) and 1 (resembling v_{peak}) at $p < 0.001$, and also excludes zero scatter at $p < 0.001$. The best-fit values for `DarkSky-400` are $\alpha = 0.57^{+0.20}_{-0.27}$ and scatter $= 0.17^{+0.03}_{-0.05}$ dex. This value of α is consistent with the value that best matches the observed satellite fraction shown in Section 6.3.4.

The $w_p(r_p)$ corresponding to this best-fit model is shown in Figure 6.9. We find that, with this new $\hat{v}_\alpha$ proxy, we can reproduce the $w_p(r_p)$ observed in the SDSS data at all four luminosity thresholds very closely, with a fixed value of α and scatter. In the same figure, the best-fit $w_p(r_p)$ for `MDPL` is also shown. The large size of the `MDPL` box results in much smaller errors on the mock $w_p(r_p)$, yet we still obtain excellent agreement with observations. We note that the agreement is good down to the small scales measured by Zehavi et al. (2011).

6.4.3 Consistency between Different Simulations

We repeat our study on the clustering with the other simulations listed in Table 6.1 to test the robustness of our results and to investigate their cosmology dependence. We use four 250 Mpc h^{-1} boxes with approximately the same mass resolution but with different cosmologies, three different N-body codes, and different initial conditions.

Figure 6.10 shows the $p > 0.05$ regions in $(\alpha, \mathrm{scatter})$ from these four boxes, and also `DarkSky-400` for reference. Despite the difference between these boxes, the $p = 0.05$ contours agree with one another very well, and the best-fit points are all in proximity in this

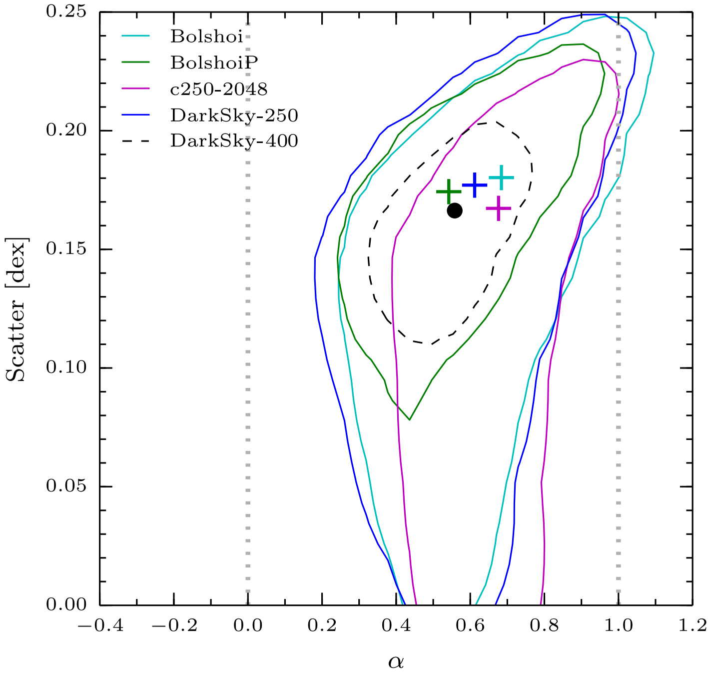

Figure 6.10: Contours of p-value = 0.05 for the combined samples ($M_r < -20.5$, -21, -21.5), for different simulations: `DarkSky-250` (blue), `c250-2048` (magenta), `Bolshoi` (cyan), `BolshoiP` (green), and `DarkSky-400` (black dashed). Crosshairs and the dot show best-fit points for the corresponding boxes.

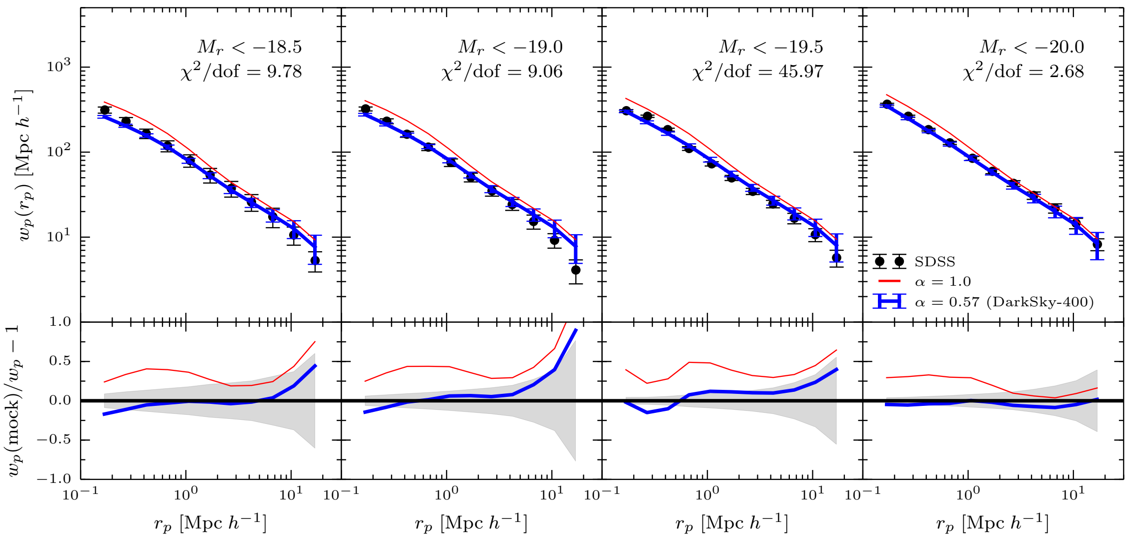

Figure 6.11: Comparison between our best-fit model and SDSS data, for dimmer thresholds than are used in the fit. Top row shows $w_p(r_p)$ for `DarkSky-400` with $\alpha = 0.57$ and scatter $= 0.17$ dex. The χ^2 values are also shown for this model at each threshold. These values are the same as those used in Figure 6.9. Circles show SDSS $w_p(r_p)$. Four columns represent four dimmer thresholds ($M_r < -18.5$, -19, -19.5, -20; from left to right). To compare with previous work, the red line shows $\hat{v}_{1.0}$ model with scatter 0.22 dex in `DarkSky-400`. Bottom row shows the relative difference with respect to SDSS data. Gray bands indicate combined SDSS and mock errors.

parameter space. This result demonstrates the robustness of our analysis. It also suggests that, within the range of cosmologies tested here (all modern ΛCDM cosmologies but with a range of values of e.g., Ω_M and σ_8), the cosmology dependence is weak enough that it cannot be distinguished in these 250 Mpc h^{-1} boxes.

6.4.4 Application to Dimmer Galaxy Samples

Since abundance matching models are based on the halo catalogs of N-body simulations, they suffer from the same limitations due to finite resolution. Particularly, for dimmer samples, abundance matching models tend to underpredict small-scale clustering (Guo et al., 2016). To avoid possible impact of the limited resolution and to obtain unbiased constraints on α and scatter, we only used galaxy samples brighter than $M_r = -20.5$ in the main results. We demonstrate that α can already be constrained even with only the bright samples.

Nevertheless, the model presented here can also provide good fits to dimmer galaxy samples given its flexibility. Even with the best-fit values of α and scatter used in Figure 6.9 (i.e., solely from the bright samples), we can obtain reasonably good matches to the clustering of dimmer samples, as shown in Figure 6.11. We note that for these four dimmer samples with $M_r > -20.5$, observed galaxies are more clustered at small scales and less so at large scales when compared to the model prediction with these particular parameter values. This hints at larger values of both α and scatter, and hence at the mass dependence of α and scatter. However, this hint could be a result of the bias due to resolution limit, and simulations of higher resolution are needed to obtain a definitive conclusion on this possible mass dependence of α and scatter.

6.5 Discussion

6.5.1 Consistency with Previous Work

We note that Reddick et al. (2013) are able to get reasonable fits to the clustering measurements by abundance matching to $v_{\rm peak}$. However, the amount of scatter required in the $v_{\rm peak}$ case is large (0.22 dex) compared to other constraints in the literature (e.g., More et al., 2009). Additionally, this $v_{\rm peak}$ model requires the exclusion of subhalos whose current mass is less than some fraction of the peak mass (using the parameter $\mu_{\rm cut} := M_{\rm vir,now}/M_{\rm peak}$), and we do not find this to be required with $\hat{v}_\alpha$. Furthermore, the $v_{\rm peak}$ model did not provide a good fit to the brightest samples when matching to luminosity (see the top left panel of Figure 26 of Reddick et al., 2013), nor did it fit the satellite fraction without excluding halos of low $M_{\rm vir,now}/M_{\rm peak}$ (i.e., with $\mu_{\rm cut} = 0$ in Reddick et al. 2013, Figure 22).

The analysis in our present paper uses a larger box with about four times the volume, and thus provides more constraining power. In Figure 6.10, one can see that given the degeneracy between scatter and α, the smaller Bolshoi box does allow for a region with

$\alpha = 1$ (corresponding to $v_{\rm peak}$) with higher scatter ($\gtrsim 0.2$). This region is consistent with the best-fit result of Reddick et al. (2013), but is ruled out here with the larger `DarkSky-400` box.

6.5.2 The Abundance Matching Framework

The core idea of abundance matching is two key assumptions: (1) all galaxies live in dark matter density peaks, and (2) galaxy properties are well correlated with halo properties. However, abundance matching should *not* be viewed as a "parameter-free" model, but instead, can be viewed as a flexible description of the galaxy–halo connection whose parameters can be constrained by observations.

By introducing this new interpolation scheme with the parameter α, we demonstrate that the abundance matching technique is more flexible than the version that was originally proposed. This interpolation scheme also provides a novel interpretation of the matching proxy. Traditionally, when we compare the performance of two abundance matching proxies, we tend to overemphasize the physical meaning of the proxy that performs better. With this α parameter, we demonstrate that, under the framework of abundance matching, there is indeed nothing special about the maximal circular velocity. It is only that observations of clustering statistics favor more concentration dependence than using simply halo mass as a proxy.

On a different note, the α parameter affects the galaxy clustering in the resulting catalog by changing the satellite fraction and the amount of assembly bias. However, we also note that, within the framework of abundance matching, these two effects (assembly bias and satellite fraction) are *linked* in the specific way when one changes the parameter α. This link is physically justified if all galaxies live in resolved halos and if galaxy and halo properties can be effectively rank matched with one of the proxies considered. On the contrary, the model in Hearin et al. (2016) do *not* assume this link, and the two effects can be adjusted separately. Nevertheless, with the clustering statistics we tested here, there is no evidence that this link, implicitly assumed when one uses abundance matching, needs to be broken.

This linked feature also enables us to constrain α with only the two-halo clustering. In fact, when we exclude small scales in our analysis, we obtain a consistent, though weaker, constraint on α. This is promising due to the more difficult nature of modeling the smallest scales, which can be impacted by fiber collisions in the data, and by resolution and baryonic effects in the simulations. At present, our best constraint on α still comes from scales in the one-halo regime, but stronger large scale constraints will be possible as data samples become larger. This result suggests that many of the key details of the galaxy–halo connection may be constrained even without the smallest scales.

It is also important to note that, in addition to the concentration dependence discussed in this work, there is still a rich set of parameters that can potentially be included in abundance matching without breaking the core assumptions mentioned above, such as using non-constant or non-Gaussian scatter, evaluating the matching proxy at different epochs, and adopting different treatments for central and satellite galaxies. With future simulations that have larger volumes and higher resolutions, we can constrain these potential abundance matching parameters, and in return obtain insights on the physical processes of galaxy formation.

6.5.3 Using Abundance Matching Proxy at its Peak Values

The discussion here made us wonder whether we also attach superfluous physical meaning to the choice of evaluating the abundance matching proxy at its peak values. This choice of peak values has been explained by that the luminosity of satellite galaxies correlates more with the subhalo properties before the stripping happens. In other words, after a subhalo infalls into a halo, the star formation would cease, but the galaxy resides in that subhalo is not immediately affected by the stripping process.

With the interpolation scheme we propose, we can also test whether the observed galaxy distribution only *prefers* peak values to present values, or it actually *favors* peak values. To test this, we introduce another parameter, β, to interpolate between peak values and present

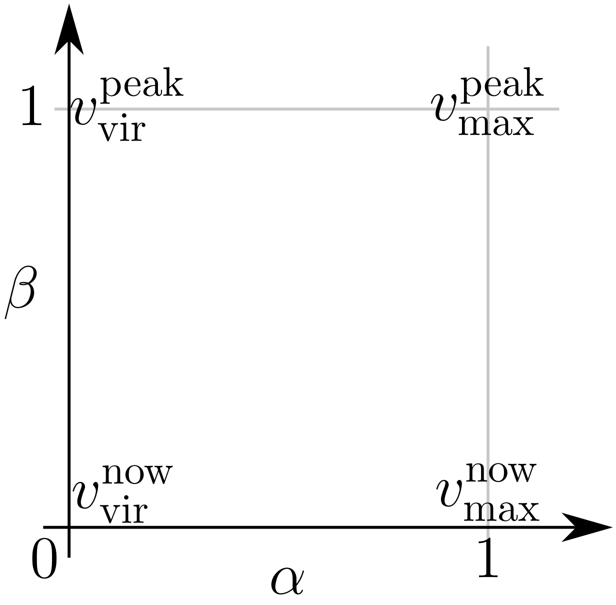

Figure 6.12: A figurative illustration of the interpolation scheme as defined in Equation 6.4.

values. We define a new proxy:

$$v_{\alpha,\beta} := \left(v_{\mathrm{vir}}^{\mathrm{now}}\right)^{(1-\alpha)(1-\beta)} \cdot \left(v_{\mathrm{vir}}^{\mathrm{peak}}\right)^{(1-\alpha)\beta} \cdot \left(v_{\mathrm{max}}^{\mathrm{now}}\right)^{\alpha(1-\beta)} \cdot \left(v_{\mathrm{max}}^{\mathrm{peak}}\right)^{\alpha\beta}, \tag{6.4}$$

such that when $\beta = 1$, $v_{\alpha,\beta=1} = v_\alpha$ evaluated at the epoch when M_{vir} peaks, as we defined in Equation 6.1, and when $\beta = 1$, $v_{\alpha,\beta=0} = v_\alpha$ evaluated at the current epoch. Figure 6.12 illustrates this interpolation scheme with a Cartesian coordinate system of α and β.

Note that in this new interpolation scheme, the β parameter interpolates the *values* at different epochs, but not the *epoch* itself. Hence, for any $\beta \neq 0$, it does *not* correspond to a single epoch for all halos. Also, we allow the β parameter to be larger than 1, in which case the matching proxy would be greater than the corresponding peak value. This setting itself might seem unphysical, but it enables us to test how physical the use of peak value actually is. If the observation data prefer a value of β that is much larger than 1, then we may infer that some unphysical assumptions have been made in the framework.

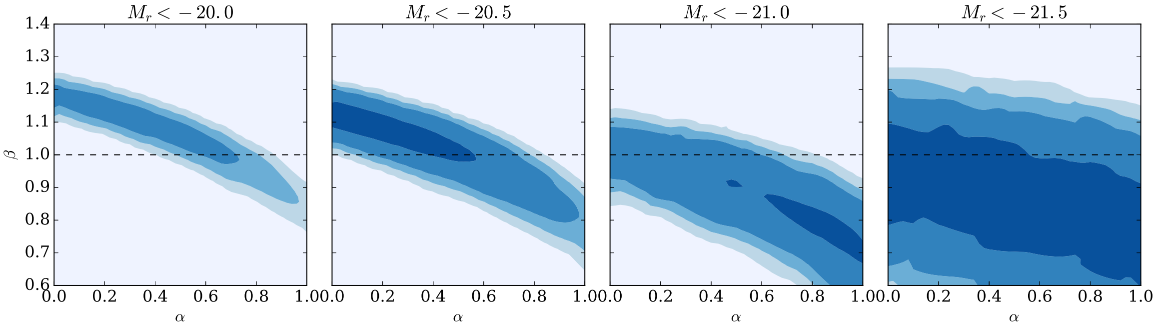

Figure 6.13: Constraints on α and β in the `DarkSky-400` box, for four thresholds ($M_r <$ −20, −20.5, −21, −21.5; from left to right). The scatter value used in abundance matching is fixed to 0.15 dex. The contours, from dark to light blue, show the one-side p-value of 0.5, 0.05, 0.01, and 0.001 for the χ^2 fit. Note that the y-axis spans from $\beta = 0.6$ to 1.4.

With this new interpolation scheme, we can simply repeat our analysis for the α parameter. The β parameter should be degenerate with the α parameter, as both parameters change the ranks of subhalos. Hence, a larger value of α and a larger value of β would both boost the one-halo term in the clustering signal. In order to better explore the degeneracy between α and β, here we fix the scatter parameter to 0.15 dex. The scatter parameter is already well constrained by the brightest threshold ($Mr < -22$), as we discussed in Section 6.4.2.

In Figure 6.13 we show the constraints on α and β for four different luminosity thresholds. The constraints are obtained with the χ^2 statistic, using the same procedure as in Section 6.4.2. The simulation used here is the `DarkSky-400` box. As expected, the constraints on parameters α and β are highly degenerate, and the preferred values of α and β are anti-correlated. We also see that the β parameter is be more sensitive to luminosity thresholds, and that fainter samples prefer a higher value of β.

Figure 6.14 shows the combined constraints on α and β, for both with and without the faintest threshold considered here ($M_r < -20$). We see that the allowed region for α is much larger when we allow β to vary. In fact, if we only include samples down to $M_r < -20.5$, we cannot rule out (at $p = 0.05$) any value of α that is between 0 and 1 when allowing β to vary. In other words, with only 2-point correlation functions, the current dataset is still not constraining enough to pin down the concentration dependence under this more

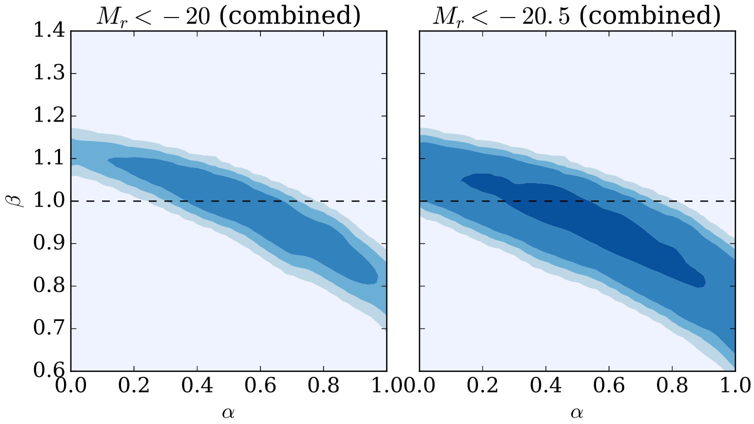

Figure 6.14: The combined joint constraint on α and β from four thresholds (left; $M_r < -20, -20.5, -21, -21.5$) and three thresholds (right; $M_r < -20.5, -21, -21.5$), for `DarkSky-400`. The scatter value used in abundance matching is fixed to 0.15 dex. The contours, from dark to light blue, show the one-side p-value of 0.5, 0.05, 0.01, and 0.001 for the χ^2 fit. Note that the y-axis spans from $\beta = 0.6$ to 1.4.

generic abundance matching framework that includes β. However, the best-fit value for α (that corresponds to the lowest χ^2 value) is still ~ 0.6, consistent with our findings in Section 6.4.

On the other hand, the range of β allowed by this dataset is much narrower than that of α. At $p = 0.05$, even with samples down to $Mr < -20.5$, we can rule out $\beta > 1.15$ and < 0.65, for any α between 0 and 1. With samples down to $Mr < -20$, we can further rule out $\beta > 1.1$ and < 0.8 for any α. This result clearly favors the choice of peak values for abundance matching proxies, even when given the freedom of adjustable concentration dependence. In other words, the adjustable concentration dependence is *not* enough to compensate the lower ranks subhalos receive when the abundance matching proxy is not evaluated at peak. This result is also consistent with the findings of Chaves-Montero et al. (2015), who used EAGLE simulations to test the correlation between the galaxy stellar mass and the matching proxy evaluated at different epochs.

The degeneracy between α and β may be broken by other statistics, as other probes can provide complementary or independent constraining power on the abundance matching parameters. For example, although in this paper we have not completed a full analysis of satellite fractions, Figure 6.4 already demonstrates that the satellite fraction as a function of luminosity can provide independent constraints on α. Similarly, other group statistics, such as the conditional luminosity function, should also provide additional constraints on α, β, and scatter.

6.5.4 Constraining Power from Other Statistics

Several other probes can provide complementary constraining power on the parameters α and β. Although in this paper we have not completed a full analysis of satellite fractions, Figure 6.4 already demonstrates that the satellite fraction as a function of luminosity can provide independent constraints on α. Similarly, other group statistics, such as the conditional luminosity function, should also provide additional constraints on α and scatter.

As an example, R. M. Reddick et al. (2016, in preparation) have studied the conditional luminosity function of galaxies in the redMaPPer cluster sample (Rykoff et al., 2014). This sample consists of a very large number of photometrically identified clusters, and hence allows for very small statistical errors on the parameters. This work finds that for models with lower scatter, data require a stronger anti-correlation between satellite occupation and central luminosity. Since satellite occupation is also anti-correlated with host halo concentration (Zentner et al., 2005; Mao et al., 2015), the result of R. M. Reddick et al. (2016, in preparation) implies an anti-correlation between scatter and α (i.e., the concentration dependence of luminosity). This result would then be complementary to the clustering results presented here, since the latter finds a positive correlation between scatter and α, provided that the correlation between scatter and α behaves the same in both luminosity-selected and redMaPPer samples.

Although we do not investigate this directly here, measurements of galaxy voids may be able to put further constraints on the amount of assembly bias (Tinker et al., 2008; Tinker & Conroy, 2009). Combining clustering results with measurements of galaxy–galaxy lensing may be able to put further limits on the scatter and on the concentration dependence (e.g., Tasitsiomi et al., 2004; Mandelbaum et al., 2006; Neistein & Khochfar, 2012). In addition, data that have more information on redshift dependence, such as the pseudo-multipole correlation function, can provide more constraints on these parameters (Reid et al., 2014; Guo et al., 2016; Saito et al., 2016).

Another way to put a physical prior on the parameters in empirical models is to compare the model predictions with hydrodynamic simulations. For example, Chaves-Montero et al. (2015) evaluated the galaxy–halo connection in the EAGLE simulation with various abundance matching models with different epochs at which the matching proxy is evaluated. In this work we establish that the galaxy luminosity has at least some dependence on halo concentration. It will be interesting to fully understand whether and to what extent such a luminosity dependence arises in modern hydrodynamic simulations, and what physical parameters it depends on.

6.6 Summary

We introduce a generalization of abundance matching which allows adjustable concentration dependence. In particular, we propose a model that abundance matches to a parameter $\hat{v}_\alpha$, which smoothly interpolates between v_vir (when $\alpha = 0$) and v_max (when $\alpha = 1$), both of which are evaluated at the peak value of the mass accretion histories.

Within the framework of abundance matching, the parameter α controls the concentration dependence of luminosity at given halo mass. Hence, α impacts both the satellite fraction and the assembly bias in the resulting mock galaxy catalog. Both effects lead to larger clustering for higher values of α, but the satellite fraction primarily increases clustering at small scales (the one-halo term), while assembly bias primarily increases clustering at larger scales (the two-halo term). This model is the first to introduce a continuously adjustable assembly bias within the abundance matching framework.

We further demonstrate that the current clustering measurements from SDSS already have constraining power on this parameter α. SDSS data prefer a range of α in the region between 0 and 1, i.e., with $\hat{v}_\alpha$ between $v_\text{vir, peak}$ and $v_\text{max, peak}$. Our best-fit value is $\alpha = 0.57^{+0.20}_{-0.27}$, with a scatter value of $0.17^{+0.03}_{-0.05}$ dex. With the high-resolution 400 Mpc h^{-1}

box, `DarkSky-400`, we show that the halo parameters $M_{\text{vir, peak}}$ and $v_{\text{max, peak}}$ which have been previously used in the literature are both ruled out at $p < 0.001$ when the various luminosity thresholds are combined.

We also extend the interpolation scheme to test if the choice of using peak values for abundance matching proxy is favored by the current clustering observations. We interpolate the proxy between its current value and its peak value using a single parameter β, and found that despite the degeneracy between the two parameters α and β, β is well constrained to be close to 1, indicating the choice of using peak values is indeed favored by observations.

In conclusion, this more general abundance matching model we present here is an important step in the quest for precise and accurate models of galaxy clustering down to small scales, which will be essential to take full advantage of the next generation of cosmological surveys.

Chapter 7

Conclusion and Outlook

In this dissertation, I use empirical models to improve the descriptions of the local velocity distribution function of dark matter (Chapter 4), the subhalo abundance function (Chapter 5), and the galaxy–halo connection under the abundance matching framework (Chapter 6). In all three cases, we find that the halo concentration (or equivalently the formation history) plays important roles in these models. Ignoring the concentration dependence will result in systematic biases when we use these models to interpret the results from various observations and experiments, such as the dark matter direct detection experiments, the abundance of dwarf galaxies, the richness–mass relations, and the large-scale spatial clustering of galaxies. The improved models provide us better precision in theoretical predictions, and also new insights into the connection among the halo formation history, the distribution of dark matter, and the galaxy–halo connection.

The importance of these improved models will likely even increase in the future. For example, thus far, we have not yet detected the collision events between dark matter and nuclei in the direct detection experiments, and hence the detailed features of the velocity distribution are not the dominate uncertainty in deriving the limits on the collision cross section. However, once we detect real collision events, a precise model for the local velocity distribution will be needed as we try to constrain the cross section, dark matter particle mass, and even Milky Way halo properties. We will also need to know the prior on the model parameters to derive those constraints. Our work on the velocity distribution has already made one step towards this upcoming future.

On a different note, our model for the subhalo abundance function extends the utility of current simulations beyond their resolution limits, and provides a more accurate description of subhalo abundance. This model is particular useful for the study of dark substructures and dwarf galaxies. In a recent study of a strong-lensed system observed by ALMA, we used this model to test the consistency between ΛCDM predictions and observed results (Hezaveh et al., 2016). Also very recently, several optical imaging surveys, including the Dark Energy Survey (DES), has discovered 17 candidate satellite galaxies in the Milky Way within the DES footprint (Bechtol et al., 2015; Koposov et al., 2015; Kim & Jerjen, 2015; Drlica-Wagner et al., 2015). It would be interesting to see if this overdensity of satellite galaxies near the Magellanic Clouds is consistent with the ΛCDM prediction.

However, the abundance of dwarf galaxies does not directly translate into the abundance of dark matter subhalos. Hence, understanding the galaxy–halo connection is a key step for interpreting the abundance of dwarf galaxies. So far, our work on the flexibility of the galaxy–halo connection has focused on bright galaxies ($M_r < -20$). An intriguing future direction is to fully model the faint end of the galaxy–halo connection.

We will soon have several rich datasets on the dwarf galaxies: in addition to the recent discovery of Milky Way satellites, the Satellite Around Galactic Analogs (SAGA) Survey, which surveys the satellite populations of Milky Way-like systems beyond the local group, will also have new results soon (Geha et al. in preparation). To fully utilize these new results, we will combine our work on the subhalo abundance and galaxy–halo relation to build a framework that can translate different aspects of the observation—luminosities, colors, velocity dispersions, and spatial distributions—into the constraints on different components of the model of the galaxy–halo connection. In the long run, this approach will provide a comprehensive picture of the galaxy–halo connection from large scales to small scales.

Bibliography

Aalseth, C. E., Barbeau, P. S., Bowden, N. S., et al. 2011, Physical Review Letters, 106, 131301

Abazajian, K. N., Adelman-McCarthy, J. K., Agüeros, M. A., et al. 2009, ApJS, 182, 543

Abel, T., Hahn, O., & Kaehler, R. 2012, MNRAS, 427, 61

Agnese, R., Ahmed, Z., Anderson, A. J., et al. 2013, Physical Review Letters, 111, 251301

Akerib, D. S., Araújo, H. M., Bai, X., et al. 2014, Physical Review Letters, 112, 091303

Allgood, B., Flores, R. A., Primack, J. R., et al. 2006, MNRAS, 367, 1781

An, J., Evans, N. W., & Deason, A. J. 2012, MNRAS, 420, 2562

An, J., & Zhao, H. 2013, MNRAS, 428, 2805

Angloher, G., Bauer, M., Bavykina, I., et al. 2012, European Physical Journal C, 72, 1971

Angulo, R. E., Lacey, C. G., Baugh, C. M., & Frenk, C. S. 2009, MNRAS, 399, 983

Aprile, E., Arisaka, K., Arneodo, F., et al. 2011, Physical Review Letters, 107, 131302

Aprile, E., Alfonsi, M., Arisaka, K., et al. 2012, Physical Review Letters, 109, 181301

Avila, S., Knebe, A., Pearce, F. R., et al. 2014, MNRAS, 441, 3488

Bechtol, K., Drlica-Wagner, A., Balbinot, E., et al. 2015, ApJ, 807, 50

Behroozi, P. S., Conroy, C., & Wechsler, R. H. 2010, ApJ, 717, 379

Behroozi, P. S., Wechsler, R. H., Lu, Y., et al. 2014, ApJ, 787, 156

Behroozi, P. S., Wechsler, R. H., & Wu, H.-Y. 2013a, ApJ, 762, 109

Behroozi, P. S., Wechsler, R. H., Wu, H.-Y., et al. 2013b, ApJ, 763, 18

Berlind, A. A., & Weinberg, D. H. 2002, ApJ, 575, 587

Bernabei, R., Belli, P., Cappella, F., et al. 2008, European Physical Journal C, 56, 333

—. 2010, European Physical Journal C, 67, 39

Bertone, G. 2010, Particle Dark Matter : Observations, Models and Searches (Cambridge University Press)

Bertone, G., Hooper, D., & Silk, J. 2005, Phys. Rep., 405, 279

Bhattacharjee, P., Chaudhury, S., Kundu, S., & Majumdar, S. 2013, Phys. Rev. D, 87, 083525

Binney, J., & Tremaine, S. 2008, Galactic Dynamics: Second Edition (Princeton University Press)

Bjornson, E., Hammarwall, D., & Ottersten, B. 2009, IEEE Transactions on Signal Processing, 57, 4027

Blanton, M. R., Lupton, R. H., Schlegel, D. J., et al. 2005a, ApJ, 631, 208

Blanton, M. R., Hogg, D. W., Bahcall, N. A., et al. 2003, ApJ, 592, 819

Blanton, M. R., Schlegel, D. J., Strauss, M. A., et al. 2005b, AJ, 129, 2562

Bovy, J., & Tremaine, S. 2012, ApJ, 756, 89

Bower, R. G., Benson, A. J., Malbon, R., et al. 2006, MNRAS, 370, 645

Boylan-Kolchin, M., Bullock, J. S., & Kaplinghat, M. 2011, MNRAS, 415, L40

Boylan-Kolchin, M., Springel, V., White, S. D. M., & Jenkins, A. 2010, MNRAS, 406, 896

Bozorgnia, N., Calore, F., Schaller, M., et al. 2016, J. Cosmology Astropart. Phys., 5, 024

Brown, W. R., Geller, M. J., Kenyon, S. J., & Diaferio, A. 2010, AJ, 139, 59

Bruch, T., Read, J., Baudis, L., & Lake, G. 2009, ApJ, 696, 920

Bryan, G. L., & Norman, M. L. 1998, ApJ, 495, 80

Bullock, J. S. 2010, ArXiv e-prints, arXiv:1009.4505 [astro-ph.CO]

Bullock, J. S., Kolatt, T. S., Sigad, Y., et al. 2001, MNRAS, 321, 559

Bullock, J. S., Wechsler, R. H., & Somerville, R. S. 2002, MNRAS, 329, 246

Busha, M. T., Marshall, P. J., Wechsler, R. H., Klypin, A., & Primack, J. 2011a, ApJ, 743, 40

Busha, M. T., Wechsler, R. H., Behroozi, P. S., et al. 2011b, ApJ, 743, 117

Cautun, M., Frenk, C. S., van de Weygaert, R., Hellwing, W. A., & Jones, B. J. T. 2014a, MNRAS, 445, 2049

Cautun, M., Hellwing, W. A., van de Weygaert, R., et al. 2014b, MNRAS, 445, 1820

CDMS II Collaboration, Ahmed, Z., Akerib, D. S., et al. 2010, Science, 327, 1619

Chaves-Montero, J., Angulo, R. E., Schaye, J., et al. 2015, ArXiv e-prints, arXiv:1507.01948

Collar, J. I., & Fields, N. E. 2012, ArXiv e-prints, arXiv:1204.3559 [astro-ph.CO]

Conroy, C., Wechsler, R. H., & Kravtsov, A. V. 2006, ApJ, 647, 201

Cooray, A., & Sheth, R. 2002, Phys. Rep., 372, 1

Crocce, M., Pueblas, S., & Scoccimarro, R. 2006, MNRAS, 373, 369

Croton, D. J., Gao, L., & White, S. D. M. 2007, MNRAS, 374, 1303

Croton, D. J., Springel, V., White, S. D. M., et al. 2006, MNRAS, 365, 11

Cui, W., Borgani, S., Dolag, K., Murante, G., & Tornatore, L. 2012, MNRAS, 423, 2279

Dariush, A. A., Raychaudhury, S., Ponman, T. J., et al. 2010, MNRAS, 405, 1873

Deason, A. J., Belokurov, V., Evans, N. W., & An, J. 2012, MNRAS, 424, L44

Deason, A. J., Conroy, C., Wetzel, A. R., & Tinker, J. L. 2013, ApJ, 777, 154

Desmond, H., & Wechsler, R. H. 2015, MNRAS, 454, 322

Diemer, B., & Kravtsov, A. V. 2015, ApJ, 799, 108

D'Onghia, E., Sommer-Larsen, J., Romeo, A. D., et al. 2005, ApJ, 630, L109

Driver, S. P., Hill, D. T., Kelvin, L. S., et al. 2011, MNRAS, 413, 971

Drlica-Wagner, A., Bechtol, K., Rykoff, E. S., et al. 2015, ApJ, 813, 109

Dutton, A. A., & Macciò, A. V. 2014, MNRAS, 441, 3359

Eddington, A. S. 1916, MNRAS, 76, 572

Essig, R., Mardon, J., & Volansky, T. 2012, Phys. Rev. D, 85, 076007

Evans, N. W., & An, J. H. 2006, Phys. Rev. D, 73, 023524

Feng, J. L. 2010, ARA&A, 48, 495

Feng, J. L., Kumar, J., Marfatia, D., & Sanford, D. 2011, Physics Letters B, 703, 124

Feng, J. L., Kumar, J., & Strigari, L. E. 2008, Physics Letters B, 670, 37

Fox, P. J., Liu, J., & Weiner, N. 2011, Phys. Rev. D, 83, 103514

Frandsen, M. T., Kahlhoefer, F., McCabe, C., Sarkar, S., & Schmidt-Hoberg, K. 2012, J. Cosmology Astropart. Phys., 1, 024

—. 2013, J. Cosmology Astropart. Phys., 7, 023

Friedland, A., & Shoemaker, I. M. 2013, Physics Letters B, 724, 183

Gao, L., Navarro, J. F., Frenk, C. S., et al. 2012, MNRAS, 425, 2169

Gao, L., Springel, V., & White, S. D. M. 2005a, MNRAS, 363, L66

Gao, L., & White, S. D. M. 2007, MNRAS, 377, L5

Gao, L., White, S. D. M., Jenkins, A., Frenk, C. S., & Springel, V. 2005b, MNRAS, 363, 379

Gao, L., White, S. D. M., Jenkins, A., Stoehr, F., & Springel, V. 2004, MNRAS, 355, 819

Garbari, S., Liu, C., Read, J. I., & Lake, G. 2012, MNRAS, 425, 1445

Garrison-Kimmel, S., Boylan-Kolchin, M., Bullock, J. S., & Lee, K. 2014, MNRAS, 438, 2578

Ghez, A. M., Salim, S., Weinberg, N. N., et al. 2008, ApJ, 689, 1044

Gillessen, S., Eisenhauer, F., Trippe, S., et al. 2009, ApJ, 692, 1075

Giocoli, C., Pieri, L., & Tormen, G. 2008, MNRAS, 387, 689

Gnedin, O. Y., Brown, W. R., Geller, M. J., & Kenyon, S. J. 2010, ApJ, 720, L108

Gondolo, P., & Gelmini, G. B. 2012, J. Cosmology Astropart. Phys., 12, 015

Green, A. M. 2012, Modern Physics Letters A, 27, 1230004

Guo, H., Zheng, Z., Behroozi, P. S., et al. 2016, MNRAS, 459, 3040

Hahn, O., & Abel, T. 2011, MNRAS, 415, 2101

Hansen, S. H., Moore, B., Zemp, M., & Stadel, J. 2006, J. Cosmology Astropart. Phys., 1, 014

Hearin, A. P., Watson, D. F., Becker, M. R., et al. 2014, MNRAS, 444, 729

Hearin, A. P., Zentner, A. R., Berlind, A. A., & Newman, J. A. 2013a, MNRAS, 433, 659

Hearin, A. P., Zentner, A. R., Newman, J. A., & Berlind, A. A. 2013b, MNRAS, 430, 1238

Hearin, A. P., Zentner, A. R., van den Bosch, F. C., Campbell, D., & Tollerud, E. 2016, MNRAS, arXiv:1512.03050

Helmi, A., White, S. D. M., & Springel, V. 2003, MNRAS, 339, 834

Henriques, B. M. B., White, S. D. M., Thomas, P. A., et al. 2015, MNRAS, 451, 2663

Hezaveh, Y. D., Dalal, N., Marrone, D. P., et al. 2016, ArXiv e-prints, arXiv:1601.01388

Ishiyama, T., Fukushige, T., & Makino, J. 2009, ApJ, 696, 2115

Ishiyama, T., Rieder, S., Makino, J., et al. 2013, ApJ, 767, 146

Jiang, F., & van den Bosch, F. C. 2014, ArXiv e-prints, arXiv:1403.6827

Jungman, G., Kamionkowski, M., & Griest, K. 1996, Phys. Rep., 267, 195

Kaehler, R., Hahn, O., & Abel, T. 2012, ArXiv e-prints, arXiv:1208.3206 [astro-ph.IM]

Kafle, P. R., Sharma, S., Lewis, G. F., & Bland-Hawthorn, J. 2012, ApJ, 761, 98

Kaplan, D. E., Luty, M. A., & Zurek, K. M. 2009, Phys. Rev. D, 79, 115016

Kauffmann, G., White, S. D. M., & Guiderdoni, B. 1993, MNRAS, 264, 201

Kavanagh, B. J., & Green, A. M. 2013, Physical Review Letters, 111, 031302

Kelso, C., Hooper, D., & Buckley, M. R. 2012, Phys. Rev. D, 85, 043515

Kim, D., & Jerjen, H. 2015, ApJ, 808, L39

Klypin, A., Gottlöber, S., Kravtsov, A. V., & Khokhlov, A. M. 1999a, ApJ, 516, 530

Klypin, A., Kravtsov, A. V., Valenzuela, O., & Prada, F. 1999b, ApJ, 522, 82

Klypin, A., Yepes, G., Gottlober, S., Prada, F., & Hess, S. 2014, ArXiv e-prints, arXiv:1411.4001

Klypin, A., Zhao, H., & Somerville, R. S. 2002, ApJ, 573, 597

Klypin, A. A., Trujillo-Gomez, S., & Primack, J. 2011, ApJ, 740, 102

Koposov, S. E., Belokurov, V., Torrealba, G., & Evans, N. W. 2015, ApJ, 805, 130

Kravtsov, A. V., Berlind, A. A., Wechsler, R. H., et al. 2004, ApJ, 609, 35

Kuhlen, M., Lisanti, M., & Spergel, D. N. 2012, Phys. Rev. D, 86, 063505

Kuhlen, M., Weiner, N., Diemand, J., et al. 2010, J. Cosmology Astropart. Phys., 2, 030

Kulier, A., & Ostriker, J. P. 2015, MNRAS, 452, 4013

Lehmann, B. V., Mao, Y.-Y., Becker, M. R., Skillman, S. W., & Wechsler, R. H. 2015, ArXiv e-prints, arXiv:1510.05651

Levi, M., Bebek, C., Beers, T., et al. 2013, ArXiv e-prints, arXiv:1308.0847 [astro-ph.CO]

Lewin, J. D., & Smith, P. F. 1996, Astroparticle Physics, 6, 87

Lin, Y.-T., Mandelbaum, R., Huang, Y.-H., et al. 2016, ApJ, 819, 119

Ling, F.-S., Nezri, E., Athanassoula, E., & Teyssier, R. 2010, J. Cosmology Astropart. Phys., 2, 012

Lisanti, M., Strigari, L. E., Wacker, J. G., & Wechsler, R. H. 2011, Phys. Rev. D, 83, 023519

Łokas, E. L., & Mamon, G. A. 2001, MNRAS, 321, 155

Lu, Y., Mo, H. J., Katz, N., & Weinberg, M. D. 2006, MNRAS, 368, 1931

Lu, Y., Yang, X., & Shen, S. 2015, ApJ, 804, 55

Lu, Y., Wechsler, R. H., Somerville, R. S., et al. 2014, ApJ, 795, 123

Ludlow, A. D., Navarro, J. F., Angulo, R. E., et al. 2014, MNRAS, 441, 378

Ludlow, A. D., Navarro, J. F., Li, M., et al. 2012, MNRAS, 427, 1322

Lynden-Bell, D. 1967, MNRAS, 136, 101

Macciò, A. V., Dutton, A. A., & van den Bosch, F. C. 2008, MNRAS, 391, 1940

Macciò, A. V., Dutton, A. A., van den Bosch, F. C., et al. 2007, MNRAS, 378, 55

Maciejewski, M., Vogelsberger, M., White, S. D. M., & Springel, V. 2011, MNRAS, 415, 2475

Mandelbaum, R., Seljak, U., Kauffmann, G., Hirata, C. M., & Brinkmann, J. 2006, MNRAS, 368, 715

Mao, Y.-Y., Strigari, L. E., & Wechsler, R. H. 2014, Phys. Rev. D, 89, 063513

Mao, Y.-Y., Strigari, L. E., Wechsler, R. H., Wu, H.-Y., & Hahn, O. 2013, ApJ, 764, 35

Mao, Y.-Y., Williamson, M., & Wechsler, R. H. 2015, ApJ, 810, 21

Marín, F. A., Wechsler, R. H., Frieman, J. A., & Nichol, R. C. 2008, ApJ, 672, 849

McCabe, C. 2010, Phys. Rev. D, 82, 023530

Merritt, D. 1985, AJ, 90, 1027

Miyatake, H., More, S., Mandelbaum, R., et al. 2015, ApJ, 806, 1

Moore, B., Ghigna, S., Governato, F., et al. 1999, ApJ, 524, L19

More, S. 2012, ApJ, 761, 127

More, S., van den Bosch, F. C., Cacciato, M., et al. 2009, MNRAS, 392, 801

More, S., Miyatake, H., Takada, M., et al. 2016, ArXiv e-prints, arXiv:1601.06063

Navarro, J. F., Frenk, C. S., & White, S. D. M. 1996, ApJ, 462, 563

—. 1997, ApJ, 490, 493

Navarro, J. F., Ludlow, A., Springel, V., et al. 2010, MNRAS, 402, 21

Neistein, E., & Khochfar, S. 2012, ArXiv e-prints, arXiv:1209.0463 [astro-ph.CO]

Neistein, E., Li, C., Khochfar, S., et al. 2011, MNRAS, 416, 1486

Norberg, P., Baugh, C. M., Gaztañaga, E., & Croton, D. J. 2009, MNRAS, 396, 19

Oguri, M., & Lin, Y.-T. 2015, ApJ, 801, 94

Old, L., Skibba, R. A., Pearce, F. R., et al. 2014, MNRAS, 441, 1513

Old, L., Wojtak, R., Mamon, G. A., et al. 2015, MNRAS, 449, 1897

Onions, J., Knebe, A., Pearce, F. R., et al. 2012, MNRAS, 423, 1200

Osipkov, L. P. 1979, Pisma v Astronomicheskii Zhurnal, 5, 77

Padmanabhan, N., Schlegel, D. J., Finkbeiner, D. P., et al. 2008, ApJ, 674, 1217

Paranjape, A., Kovač, K., Hartley, W. G., & Pahwa, I. 2015, MNRAS, 454, 3030

Pato, M., Baudis, L., Bertone, G., et al. 2011, Phys. Rev. D, 83, 083505

Pato, M., Strigari, L. E., Trotta, R., & Bertone, G. 2013, J. Cosmology Astropart. Phys., 2, 041

Peacock, J. A., & Smith, R. E. 2000, MNRAS, 318, 1144

Peter, A. H. G. 2010, Phys. Rev. D, 81, 087301

Pillepich, A., Kuhlen, M., Guedes, J., & Madau, P. 2014, ApJ, 784, 161

Planck Collaboration, Ade, P. A. R., Aghanim, N., et al. 2015, ArXiv e-prints, arXiv:1502.01589

Prada, F., Klypin, A. A., Cuesta, A. J., Betancort-Rijo, J. E., & Primack, J. 2012, MNRAS, 423, 3018

Press, W. H., & Schechter, P. 1974, ApJ, 187, 425

Purcell, C. W., & Zentner, A. R. 2012, J. Cosmology Astropart. Phys., 12, 007

Purcell, C. W., Zentner, A. R., & Wang, M.-Y. 2012, J. Cosmology Astropart. Phys., 8, 027

Read, J. I., Lake, G., Agertz, O., & Debattista, V. P. 2008, MNRAS, 389, 1041

Reddick, R. M., Wechsler, R. H., Tinker, J. L., & Behroozi, P. S. 2013, ApJ, 771, 30

Reed, D. S., Koushiappas, S. M., & Gao, L. 2011, MNRAS, 415, 3177

Reid, B. A., Seo, H.-J., Leauthaud, A., Tinker, J. L., & White, M. 2014, MNRAS, 444, 476

Reyes, R., Mandelbaum, R., Hirata, C., Bahcall, N., & Seljak, U. 2008, MNRAS, 390, 1157

Rodríguez-Puebla, A., Avila-Reese, V., & Drory, N. 2013a, ApJ, 767, 92

—. 2013b, ApJ, 773, 172

Rodríguez-Puebla, A., Drory, N., & Avila-Reese, V. 2012, ApJ, 756, 2

Rozo, E., Rykoff, E. S., Bartlett, J. G., & Melin, J.-B. 2015, MNRAS, 450, 592

Rozo, E., Rykoff, E. S., Koester, B. P., et al. 2009, ApJ, 703, 601

Rozo, E., Wechsler, R. H., Rykoff, E. S., et al. 2010, ApJ, 708, 645

Rykoff, E. S., Rozo, E., Busha, M. T., et al. 2014, ApJ, 785, 104

Saito, S., Leauthaud, A., Hearin, A. P., et al. 2016, MNRAS, arXiv:1509.00482

Scoccimarro, R., Sheth, R. K., Hui, L., & Jain, B. 2001, ApJ, 546, 20

Seljak, U. 2000, MNRAS, 318, 203

Sheth, R. K., Mo, H. J., & Tormen, G. 2001, MNRAS, 323, 1

Sheth, R. K., & Tormen, G. 1999, MNRAS, 308, 119

Skillman, S. W., Warren, M. S., Turk, M. J., et al. 2014, ArXiv e-prints, arXiv:1407.2600

Smith, M. C., Ruchti, G. R., Helmi, A., et al. 2007, MNRAS, 379, 755

Somerville, R. S., Hopkins, P. F., Cox, T. J., Robertson, B. E., & Hernquist, L. 2008, MNRAS, 391, 481

Sorensen, P. 2012, Phys. Rev. D, 86, 101301

Sparre, M., & Hansen, S. H. 2012, J. Cosmology Astropart. Phys., 10, 049

Springel, V. 2005, MNRAS, 364, 1105

Springel, V., Yoshida, N., & White, S. D. M. 2001, New A, 6, 79

Springel, V., Wang, J., Vogelsberger, M., et al. 2008, MNRAS, 391, 1685

Srisawat, C., Knebe, A., Pearce, F. R., et al. 2013, MNRAS, 436, 150

Stiff, D., & Widrow, L. M. 2003, Physical Review Letters, 90, 211301

Strigari, L. E. 2013, Phys. Rep., 531, 1

Strigari, L. E., & Trotta, R. 2009, J. Cosmology Astropart. Phys., 11, 019

Sunayama, T., Hearin, A. P., Padmanabhan, N., & Leauthaud, A. 2016, MNRAS, 458, 1510

Tasitsiomi, A., Kravtsov, A. V., Wechsler, R. H., & Primack, J. R. 2004, ApJ, 614, 533

Tinker, J., Wetzel, A., & Conroy, C. 2011, ArXiv e-prints, arXiv:1107.5046 [astro-ph.CO]

Tinker, J. L., & Conroy, C. 2009, ApJ, 691, 633

Tinker, J. L., Conroy, C., Norberg, P., et al. 2008, ApJ, 686, 53

Tinker, J. L., George, M. R., Leauthaud, A., et al. 2012, ApJ, 755, L5

Trujillo-Gomez, S., Klypin, A., Primack, J., & Romanowsky, A. J. 2011, ApJ, 742, 16

Vale, A., & Ostriker, J. P. 2004, MNRAS, 353, 189

—. 2006, MNRAS, 371, 1173

van den Bosch, F. C., & Jiang, F. 2014, ArXiv e-prints, arXiv:1403.6835

Vergados, J. D., Hansen, S. H., & Host, O. 2008, Phys. Rev. D, 77, 023509

Vogelsberger, M., & White, S. D. M. 2011, MNRAS, 413, 1419

Vogelsberger, M., Helmi, A., Springel, V., et al. 2009, MNRAS, 395, 797

Vogelsberger, M., Genel, S., Springel, V., et al. 2014, MNRAS, 444, 1518

Wang, W., Han, J., Cooper, A. P., et al. 2015, MNRAS, 453, 377

Warren, M. S. 2013, in Proceedings of the International Conference on High Performance Computing, Networking, Storage and Analysis, SC '13 (New York, NY, USA: ACM), 72:1

Watson, D. F., Berlind, A. A., & Zentner, A. R. 2011, ApJ, 738, 22

Wechsler, R. H., Bullock, J. S., Primack, J. R., Kravtsov, A. V., & Dekel, A. 2002, ApJ, 568, 52

Wechsler, R. H., Somerville, R. S., Bullock, J. S., et al. 2001, ApJ, 554, 85

Wechsler, R. H., Zentner, A. R., Bullock, J. S., Kravtsov, A. V., & Allgood, B. 2006, ApJ, 652, 71

Wu, H.-Y., Hahn, O., Wechsler, R. H., Behroozi, P. S., & Mao, Y.-Y. 2013a, ApJ, 767, 23

Wu, H.-Y., Hahn, O., Wechsler, R. H., Mao, Y.-Y., & Behroozi, P. S. 2013b, ApJ, 763, 70

Xue, X. X., Rix, H. W., Zhao, G., et al. 2008, ApJ, 684, 1143

Yang, X., Mo, H. J., & van den Bosch, F. C. 2006, ApJ, 638, L55

Yang, X., Mo, H. J., Zhang, Y., & van den Bosch, F. C. 2011, ApJ, 741, 13

Zehavi, I., Zheng, Z., Weinberg, D. H., et al. 2011, ApJ, 736, 59

Zentner, A. R., Berlind, A. A., Bullock, J. S., Kravtsov, A. V., & Wechsler, R. H. 2005, ApJ, 624, 505

Zentner, A. R., Hearin, A. P., & van den Bosch, F. C. 2014, MNRAS, 443, 3044

Zhu, G., Zheng, Z., Lin, W. P., et al. 2006, ApJ, 639, L5